Journal of Seismic Exploration

ISSN: 0963-0651

Volume 34 · Issue 4
2025

ACCSCIENCE PUBLISHING

State Key Laboratory for Fine
Exploration and Intelligent
Development of Coal Resources

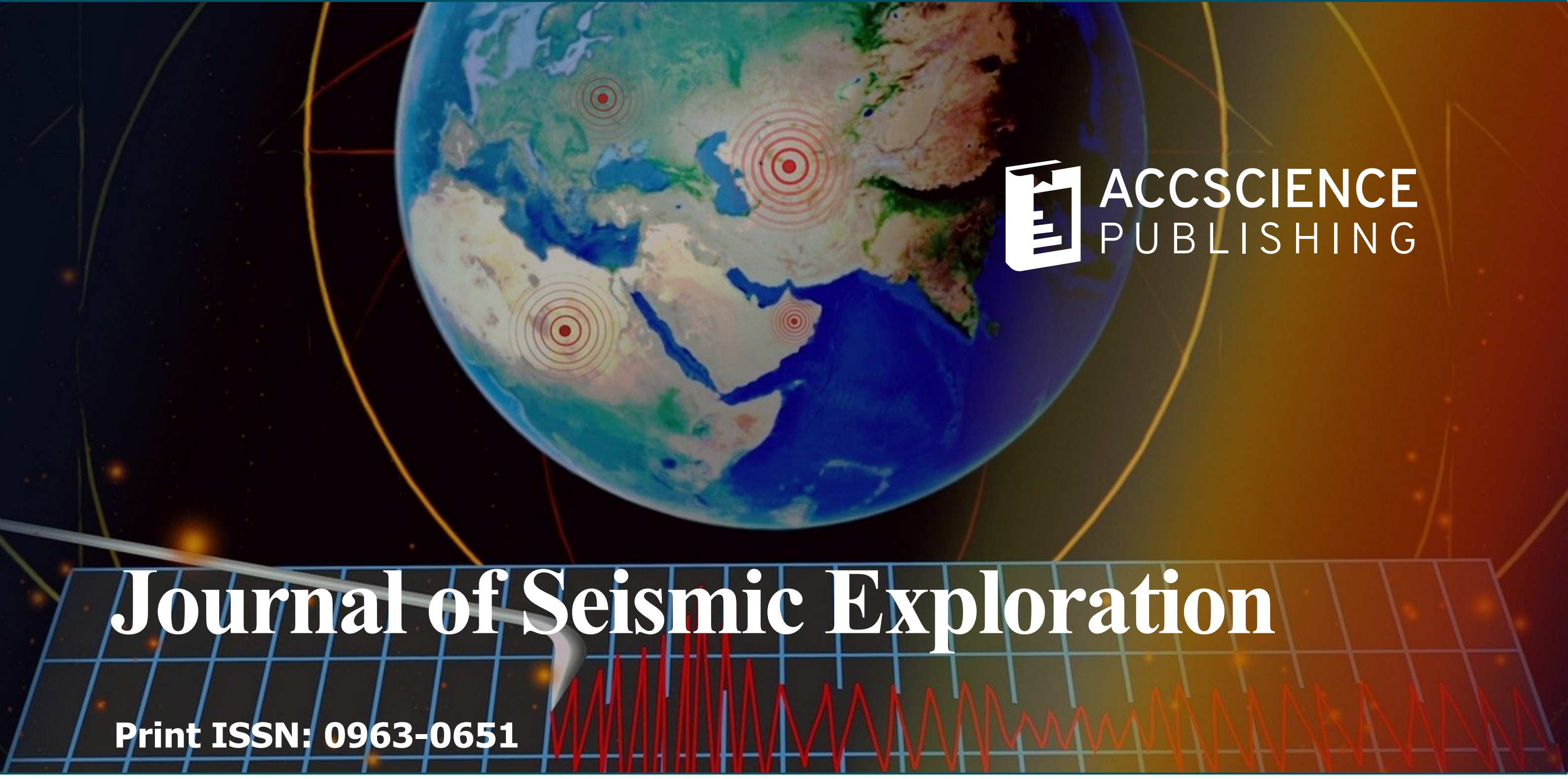

Journal of Seismic Exploration

Print ISSN: 0963-0651

The Journal of Seismic Exploration (JSE) is an international medium for the publication of research in seismic modeling, processing, inversion, interpretation, field techniques, borehole techniques, tomography, instrumentation and software. The aim and goal of JSE is to serve the interests and objectives of seismic petroleum exploration. All seismic processing methods have assumptions and prerequisites- and when they are satisfied methods are effective-and when they are violated methods become ineffective and can fail. The latter contributes to drilling dry hole exploration wells and suboptimal development wells.

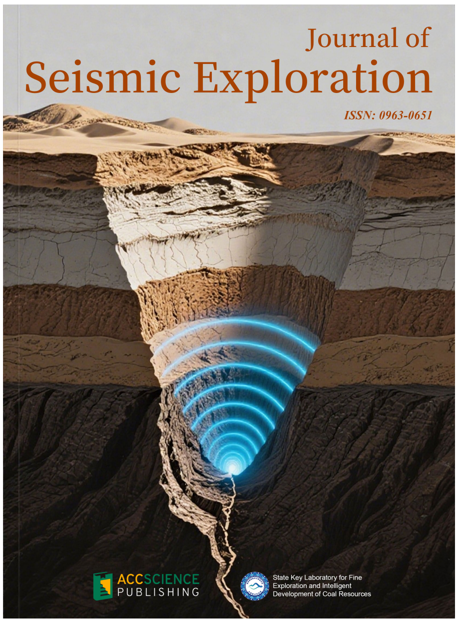

About the Publisher

AccScience Publishing is a publishing company based in Singapore. We publish a range of high-quality, open-access, peer-reviewed journals and books from a broad spectrum of disciplines.

Contact Us

Managing Editor
jse.office@accscience.sg

AccScience Publishing
9 Raffles Place, Republic Plaza 1 #06-00 Singapore 048619.

Volume 34 • Issue 4 • 2025
ISSN 0963-0651 (print)

Journal of Seismic Exploration

Editors-in-Chief

Suping Peng
State Key Laboratory for Fine Exploration and Intelligent Development of Coal Resources

Arthur B. Weglein
University of Houston

ACCSCIENCE PUBLISHING

Access Science Without Barriers

Full issue copyright © 2025 AccScience Publishing
All rights reserved. Without permission in writing from the publisher, this full issue publication in its entirety may not be reproduced or transmitted for commercial purposes in any form or by any means, electronic or mechanical, including photocopying, recording, or any information storage and retrieval system. Permissions may be sought from jse.office@accscience.sg

Article copyright © Respective Author(s)
See articles for copyright year. All articles in this full issue publication are open-access. There are no restrictions in the distribution and reproduction of individual articles, provided the original work is properly cited. However, permission to reuse copyrighted materials of an article for commercial purposes is applicable if the article is licensed under Creative Commons Attribution-NonCommercial License. Check the specific license before reusing.

JOURNAL OF SEISMIC EXPLORATION

ISSN: 0963-0651 (print)

Editorial and Production Credits

Publisher: AccScience Publishing
Managing Editor: Gary Liu
Production Editor: Lim Mingyuan
Article Layout and Typeset: Sinjore Technologies (India)

For all advertising queries, contact
jse.office@accscience.sg

Supplementary file

Supplementary files of articles can be obtained at https://accscience.com/journal/JSE/34/4.

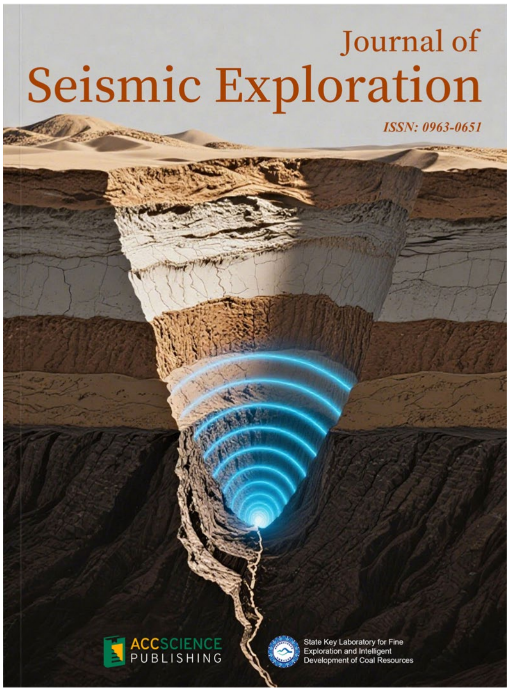

Disclaimer

AccScience Publishing is not liable to the statements, perspectives, and opinions contained in the publications. The appearance of advertisements in the journal shall not be construed as a warranty, endorsement, or approval of the products or services advertised and/or the safety thereof. AccScience Publishing disclaims responsibility for any injury to persons or property resulting from any ideas or products referred to in the publications or advertisements. AccScience Publishing remains neutral with regard to jurisdictional claims in published maps and institutional affiliations.

Journal of Seismic Exploration

Editorial Board

Volume 34 | Issue 4 | 2025 | Page 1 – 88 |

Journal of Seismic Exploration

https://accscience.com/journal/JSE

CONTENTS

REVIEW

ARTICLES

RETRACTION

ACCSCIENCE PUBLISHING

Journal of Seismic Exploration

REVIEW

Advances in theoretical and technical approaches for seismic prediction of reservoir permeability

Lele Wei, Lideng Gan*, Hao Yang, Xinyu Li, Gang Hao, and Xiaoyu Jiang

Research Institute of Petroleum Exploration and Development, PetroChina Company Limited, Beijing, China

Abstract

Reservoir permeability serves as a critical parameter for unconventional reservoir characterization and hydrocarbon recovery optimization. However, complex petrophysical mechanisms and multifactorial coupling make its seismic prediction face significant challenges. This review comprehensively synthesized advances and limitations across three dominant methodologies: (i) dispersion/attenuation-based methods, limited by petrophysical assumptions, scaling issues, and non-uniqueness; (ii) pore structure-constrained methods, enhancing prediction accuracy but hindered by oversimplification and high-dimensional inversion instability; and (iii) artificial intelligence frameworks, offering data efficiency yet challenged by error propagation, overfitting vulnerability, and geologically implausible extrapolation. Comparative analysis revealed core bottlenecks in inadequate multiscale coupling between petrophysical mechanisms and data-driven approaches. These challenges are compounded by the absence of cross-disciplinary validation frameworks. To address these challenges, this review integrated interdisciplinary perspectives from seismic exploration, petrophysics, and machine learning. It proposed a tripartite permeability prediction paradigm unifying physical mechanisms, data-driven techniques, and engineering validation. This framework encompasses: first, advancing multi-porosity fluid-solid coupling theory and pore structure-constrained rock physics models; second, constructing physics-guided multimodal learning architectures that deeply embed differentiable physical laws (e.g., Darcy-Biot theory) within cross-scale physics-informed neural networks, coupling microscopic pore network simulations with macroscopic seismic responses; third, establishing a closed-loop workflow covering digital rock core simulations, blind well testing validation, production history matching, and dynamic data-driven evolution, thereby forming a quantifiable and iteratively upgradable technological system. This paradigm provides a multiscale approach for accurately characterizing permeability in unconventional reservoirs, and it establishes foundational theoretical principles and delineates practical implementation pathways for economically viable unconventional resource development.

Keywords: Geophysical exploration; Reservoir permeability; Dispersion and attenuation; Pore structure; Artificial intelligence

***Corresponding author:**
Lideng Gan
(gld@petrochina.com.cn)

Citation: Wei L, Gan L, Yang H, Li X, Hao G, Jiang X. Advances in theoretical and technical approaches for seismic prediction of reservoir permeability. *J Seismic Explor*. 2025;34(4):1-17. doi: 10.36922/JSE025310050

Received: August 1, 2025

Revised: September 7, 2025

Accepted: September 12, 2025

1. Introduction

Reservoir permeability is a critical parameter for unconventional reservoir classification. It directly governs reservoir simulation outcomes and serves as an essential element in reservoir engineering, with significant implications for field development.[1-3] Seismic data provide a cost-effective characterization of lateral formation distribution and inter-well reservoir properties due to their extensive spatial coverage and relatively low acquisition costs. Therefore, to enhance prediction accuracy, developing effective seismic prediction methodologies for reservoir permeability holds substantial theoretical and practical value for optimizing the exploration and development of low-porosity and low-permeability reservoirs.[4]

Research on geophysical permeability prediction has primarily evolved along three trajectories over recent decades:[5] (i) numerical simulations grounded in classical rock physics models or laboratory core measurements, (ii) well-log-based permeability interpretation, and (iii) seismic inversion of permeability parameters. While core measurements deliver high accuracy, they are expensive, time-intensive, and spatially limited to discrete sample points. Well-log-based permeability offers continuous vertical profiles with moderate accuracy but remains costly and inherently localized ("single-well" perspective), lacking lateral continuity for areal development guidance. In contrast, seismic methods provide economically viable and laterally extensive formation characterization. Nevertheless, the complex and non-explicit relationship between permeability and seismic responses, compounded by multifactorial controls, renders seismic permeability prediction a persistently challenging frontier.

A pivotal 2001 United States Department of Energy workshop engaged 15 experts from industry, national labs, and academia to evaluate the detectability and invertibility of permeability within seismic data. Pride's synthesis confirmed that permeability information resides within seismic-frequency observations and outlined potential inversion frameworks, catalyzing significant research momentum.[6] Current seismic permeability prediction methodologies converge on three dominant approaches: dispersion/attenuation-based methods, pore structure-based techniques, and artificial intelligence (AI)-driven solutions.

Seismic permeability prediction currently resides in a phase of methodological exploration, challenged by the strongly nonlinear and implicitly coupled mechanisms between permeability and seismic responses. Permeability is governed by multifaceted controls, notably pore-throat architecture. These controls fundamentally impede the establishment of robust porosity and permeability mapping models based solely on core or well-log data. Consequently, effective permeability prediction in complex reservoirs remains elusive. Despite inherent obstacles, including theoretical model misfit and solution non-uniqueness, seismic permeability prediction persists as a frontier research focus. It lies at the interface of geophysics and reservoir engineering. This persistence is driven by its critical value in dynamic reservoir characterization. Recent advances in deep learning have accelerated data-driven methodologies. However, three persistent bottlenecks endure: (i) traditional rock physics models, such as the Biot-Squirt (BISQ) framework, exhibit limited generalizability in highly heterogeneous formations, failing to accurately quantify the coupling of pore-throat architecture with seismic wavefields; (ii) machine learning approaches establish nonlinear mappings, but they suffer from interpretability deficits and physical decoupling, producing predictions unconstrained by geological plausibility; and (iii) multiscale data integration across core-log-seismic domains lacks standardized protocols, with information degradation during upscaling constraining prediction accuracy.

This review systematically synthesized technological advancements in seismic permeability prediction through a structured analysis of three dominant methodologies: dispersion/attenuation-based techniques leveraging frequency-dependent velocity characteristics, pore structure-oriented approaches, and AI-driven solutions employing deep learning architectures. By evaluating the theoretical foundations, technical advantages, and limitations of these paradigms, we proposed a transformative "dual-engine" predictive framework that embedded rock physics constraints within deep learning infrastructures. This mechanism and data co-driven model integrates theoretical rigor with data-adaptive capability, particularly through physics-informed neural networks. As a result, the model overcomes applicability barriers in complex reservoirs where traditional methods falter.

The subsequent sections of this paper are organized as follows: Section 2 elaborates on the theoretical foundations and representative techniques of dispersion/attenuation-based methods. Section 3 focuses on the key technologies and applications of pore structure-based methods. Section 4 analyzes the progress and challenges of AI-driven solutions. Section 5 explores potential future research directions. Finally, Section 6 concludes the review.

2. Permeability prediction methods based on dispersion and attenuation

These approaches comprise three primary categories: (i) theoretical model-based inversion, (ii) velocity dispersion/quality factor prediction, and (iii) fluid mobility attribute prediction.

2.1. Model-based inversion

Theoretical forward modeling investigates how reservoir parameters (e.g., porosity, permeability, and fluid saturation) influence seismic wave propagation characteristics (e.g., dispersion, attenuation, and reflection coefficients), providing foundations for geophysical parameter inversion. Typically, this inversion seeks an optimal permeability value within predefined bounds, minimizing misfit between model-predicted and observed P-wave velocity dispersion or quality factor, effectively transforming permeability estimation into an optimization problem. Some typical model-based inversion methods are summarized in Table 1.

The BISQ model, incorporating both Biot flow and squirt flow mechanisms, effectively explains high dispersion/attenuation in seismic frequencies. Nie *et al.*[7] implemented BISQ-based inversion using niche genetic algorithms, while Zhang *et al.*[8] derived 3D anisotropic dispersion equations and analyzed azimuthal dispersion effects on permeability inversion. To address inherent limitations of genetic algorithms (e.g., premature convergence and poor local search), Fang and Yang[9] developed a hybrid genetic-simulated annealing algorithm demonstrating superior accuracy and convergence. In addition, a series of advancements in reservoir parameter inversion was achieved based on the BISQ model.[10,11] White[12] and White *et al.*[13] complemented the macroscopic-scale Biot theory and microscopic-scale squirt flow mechanisms and introduced a mesoscopic dissipation mechanism, finally deriving frequency-dependent attenuation and dispersion functions for partially saturated porous media parameterized using permeability, porosity, and pore-fluid properties. Johnson[14] subsequently extended White's model to accommodate arbitrarily sized fluid patches by incorporating geometric characteristic parameters S/V and T. Later, Sun[15] integrated these tri-scale (macro-meso-micro) dispersion-attenuation mechanisms to develop the Biot-patchy-squirt (BIPS) model, which characterized wave dispersion and attenuation in immiscible fluid-saturated fractured poroelastic media. In the aforementioned models, permeability characterization requires inversion through attenuation response without establishing an explicit theoretical relationship. For example, in the mesoscopic White's layered patchy saturation model, White[12] derived the expression for the complex modulus of P-waves ($E[\omega]$), which implicitly encoded permeability information. Relying on this discovery and applying plane wave theory, one can compute the phase velocity (V_p) and inverse quality factor (Q^{-1}).

$$E(\omega)=\left\{\frac{1}{K_{\mathrm{BGH}}+(4/3)N}+\frac{2(\gamma_2-\gamma_1)^2\sqrt{\dfrac{\kappa}{\eta}}}{\sqrt{i\omega}(L_1+L_2)\cdot\displaystyle\sum_{j=1}^{2}\sqrt{K_{E_j}}\coth\Big(\frac{L_j}{2}\sqrt{\frac{i\omega}{\frac{\kappa}{\eta}K_{E_j}}}\Big)}\right\}^{-1} \quad \text{(I)}$$

$$V_{\mathrm{p}}=\left(\mathrm{Re}\left(\sqrt{\frac{(1-\phi)\rho_{\mathrm{s}}+\phi(S_1\rho_{\mathrm{f}_1}+S_2\rho_{\mathrm{f}_2})}{E(\omega)}}\right)\right)^{-1} \quad \text{(II)}$$

$$Q^{-1}=\frac{\mathrm{Im}\left(\dfrac{E(\omega)}{(1-\phi)\rho_{\mathrm{s}}+\phi(S_1\rho_{\mathrm{f}_1}+S_2\rho_{\mathrm{f}_2})}\right)}{\mathrm{Re}\left(\dfrac{E(\omega)}{(1-\phi)\rho_{\mathrm{s}}+\phi(S_1\rho_{\mathrm{f}_1}+S_2\rho_{\mathrm{f}_2})}\right)} \quad \text{(III)}$$

where L denotes the thickness of the porous layer, K_{BGH} represents Hill's approximate expression of the Gassmann modulus at high frequencies, N signifies the shear modulus of the dry rock frame, γ indicates the ratio of fast P-wave fluid tension to total stress, η refers to the viscosity coefficient, κ designates the permeability, ω is the angular frequency, K_E denotes the effective modulus of

Table 1. Theoretical and application characteristics of typical model-based inversion methods

Model name	Core mechanism	Target reservoir type	Permeability representation
BISQ	Coupling of Biot flow and squirt flow	Medium-high porosity/permeability sandstones	Implicit (inverted via attenuation response)
White/Johnson	Mesoscopic fluid patch dissipation	Partially saturated porous media	Implicit (inverted via attenuation response)
BIPS	Macro-meso-micro coupling	Fracture-pore dual media	Implicit (inverted via attenuation response)
Geometric network model	Parametrization of elliptical pore/fracture geometry	Fracture-pore/fracture reservoirs	Explicit equation

Abbreviations: BIPS: Biot-patchy-squirt; BISQ: Biot-Squirt.

compressional wave, S represents the fluid saturation, and ρ_S and ρ_f are the densities of the grain mineral and pore fluid, respectively.

The following equations provide a methodology for establishing explicit permeability representation relationships. For example, Xiong *et al.*[16] and Wei *et al.*[17] established a 3D network model with elliptical cross-sections for fractures and soft pores. They incorporated permeability relationships with porosity, confining pressure, and pore aspect ratio, deriving a computational methodology for permeability estimation.

$$\kappa(\omega) = \frac{\eta L}{A} \cdot \frac{\left(\chi \cdot P_U + \delta \cdot P_D\right)}{P_U - P_D} \tag{IV}$$

$$\chi = 2\left(\frac{\alpha^3}{1+\alpha^2}\right)\frac{-\mathrm{i}\pi R^2}{\rho_f c}\left(\frac{\cos\left(\omega L/c\right)}{\sin\left(\omega L/c\right)}\right)\left(\frac{2J_1\left(KR\right)}{KRJ_0\left(KR\right)} - 1\right) \tag{V}$$

$$\delta = 2\left(\frac{\alpha^3}{1+\alpha^2}\right)\frac{\mathrm{i}\pi R^2}{\rho_f c}\left(\frac{1}{\sin\left(\omega L/c\right)}\right)\left(\frac{2J_1\left(KR\right)}{KRJ_0\left(KR\right)} - 1\right) \tag{VI}$$

where η denotes the fluid viscosity, L represents the length of the microtube, A indicates the cross-sectional area ($\alpha\pi R^2$), R is the semi-major axis radius of the elliptical cross-section, α refers to the aspect ratio of the fracture cross-section, P_U and P_D denote the pressure at both ends of the microtube, respectively, ρ_f signifies the density of the fluid within the microtube, J designates the zeroth-order Bessel function of the first kind, K represents $K = \sqrt{\frac{\mathrm{i}\omega\rho_\mathrm{f}}{\eta}}$, and C is the acoustic wave velocity in the fluid.

Tan *et al.*[18] integrated the coupled effects of solid particle detachment, fluid-solid coupling, multiphase flow, and stress sensitivity into a fluid and structure-coupled stress-sensitive permeability model grounded in material mechanics and fractal theory. They thus provided theoretical guidance for accurate prediction of flow behavior and development optimization in stress-sensitive reservoirs.

It is evident that most existing pore media and fracture-pore media models implicitly incorporate permeability information. However, they fail to establish explicit theoretical permeability relationships. Alternatively, the developed permeability models contain numerous physical parameters of the rock matrix. These parameters hinder direct permeability prediction using exploration data. Furthermore, the inversion process reveals that the effectiveness of rock physics inversion critically depends on the accuracy of elastic parameters derived from prestack seismic data and the congruence between rock physics models and actual formation properties. Key limitations of model-based permeability inversion include: (i) solution non-uniqueness and low noise tolerance, (ii) significant result divergence across different dispersion-attenuation models despite generally consistent permeability response patterns in forward modeling, and (iii) frequent mismatches between theoretical predictions and field observations.

2.2. Velocity dispersion/quality factor-based methods

In field applications, acquiring comprehensive velocity dispersion data at every sampling point remains challenging. Theoretical forward modeling generally indicates an inverse relationship between permeability and dispersion: low permeability correlates with high dispersion, while high permeability corresponds to low dispersion.

Following this principle, Liu[19] applied frequency-dependent amplitude variation with offset (AVO) theory to quantify P-wave velocity dispersion as a fluid mobility proxy for permeability prediction. Yuan *et al.*[5] established permeability and dispersion relationships through core-derived rock physics analysis and determined the first-order relative variation of Young's modulus with seismic frequency and the second-order relative variation of permeability with pressure. Then, subsequent frequency-dependent amplitude variation with incident angle (AVA) inversion of well logs yielded the reservoir's P-wave dispersion, enabling permeability prediction through the derived relationships. Wu *et al.*[20] developed a quality factor-based method, which involved correlation between averaged core permeability and well quality factors, and then they estimated permeability at unlogged locations through seismic waveform similarity analysis to reference wells.

The intrinsic limitations of dispersion attribute methods originate from fundamental physical and operational constraints:[21,22] conventional seismic bandwidth (10–100 Hz) fails to excite significant dispersion effects in high-permeability reservoirs (κ >10 mD). This failure occurs due to fluid pressure diffusion thresholds below 10 Hz, which critically attenuate permeability sensitivity. This bandwidth confinement triggers a cascading degradation: high-fidelity Q-factor inversion demands ultrabroadband data (>3 octaves), yet narrow field-acquisition bandwidths (<2 octaves) propagate

Q-estimation errors into permeability predictions. Further compounded by anisotropic scattering, fracture azimuthal variability induces phase velocity dispersion anomalies that mask permeability signatures. Collectively, these interdependencies form an error amplification chain. The chain restricts dispersion-based methods to homogeneous siliciclastic reservoirs with moderate permeability, while faltering in fractured or stress-sensitive formations. Collectively, these constraints necessitate addressing two persistent bottlenecks: (i) non-unique solutions in frequency-dependent AVO/AVA dispersion attribute inversion and (ii) significant relative errors in current Q-factor extraction techniques, compromising permeability estimation accuracy.

2.3. Fluid mobility-based methods

Fluid mobility (M), defined as the ratio of reservoir permeability (κ) to fluid viscosity (η), characterizes the coupled effects of pore structure's conductivity and pore fluid viscosity. At present, fluid mobility-based methods constitute the predominant approach for permeability prediction within dispersion-attenuation frameworks.

In 2004, Silin *et al.*[23] derived the low-frequency asymptotic reflection coefficient for fluid-saturated porous media:

$$R = \frac{Z_1 - Z_2}{Z_1 + Z_2} + R_1 \frac{1+i}{\sqrt{2}} \sqrt{\left| \mathrm{i}\left(\frac{\kappa}{\eta}\rho_f \omega\right) \right|} + \cdots \tag{VII}$$

where Z denotes impedance, ρ_f is fluid density, and ω is angular frequency. This equation establishes a positive correlation between the reflection coefficient and the square root of the product term. Goloshubin *et al.*[24] and Goloshubin *et al.*[25] subsequently proposed a novel frequency-dependent imaging attribute when analyzing dual-porosity media attenuation. Proportional to $\sqrt{M}$, this attribute was applied to reservoir permeability estimation. On this basis, Chen *et al.*[26] developed a computational expression for fluid mobility attributes and established a method to identify the dominant frequency within the low-frequency band of seismic signals. This approach enabled the direct calculation of reservoir fluid mobility using the instantaneous spectrum of the low-frequency dominant frequency. The computational expression is given as follows:

$$M \approx \frac{1}{C^2}\left[\frac{dA(\omega)}{d\omega}\right]^2 \omega \tag{VIII}$$

where C is a proportionality coefficient, ω is the dominant low frequency, and $A(\omega)$ is the amplitude spectrum of the low-frequency band derived from time-frequency analysis.

This framework facilitates subsequent methodological advances. For example, Zhao *et al.*[27] investigated the effects of fluid mobility on dispersion and attenuation using dual-porosity and dual-permeability models. Lu[28] developed a Bayesian framework for direct mobility inversion. Zhang *et al.*[29] enhanced reservoir prediction accuracy by integrating the synchro-squeezed generalized S-transform with Lucy-Richardson deconvolution into mobility computation.

The model-based inversion approach in Section 2.1 and the permeability prediction technique using dispersion/attenuation attributes in Section 2.2 were compared. The comparison revealed that the core advantage of the latter method lies in circumventing Q-factor extraction errors and directly establishing a quantitative correlation between seismic amplitude and fluid mobility. Application to actual marine seismic data from the JZ area of the Bohai Sea demonstrated that the fluid mobility attribute exhibits significant imaging advantages for hydrocarbon reservoirs. It enables precise spatial delineation of reservoir distribution while substantially reducing the non-uniqueness and uncertainty in fluid identification. A representative case study from Chen *et al.*[26] illustrated these capabilities (Figure 1). The fluid mobility measurement profile displays a high-amplitude "bright spot" anomaly at the gas reservoir location, while the fluid mobility slice extracted along the gas-bearing interval clearly delineates the spatial boundaries of high-permeability zones (outlined by black dashed contours).

Most current methods approximate mobility attributes through time-frequency decomposition for qualitative permeability assessment. However, reservoir thickness below λ/8 induces significant low-frequency amplitude distortion, which requires integrated compensation through high-frequency tuning effects, combined with subjectivity in dominant frequency selection and the petrophysical-property dependency of calibration coefficient C. Consequently, these thin-bed resolution constraints collectively result in fundamental limitations of such methods: Uncertainties artificially introduced by the subjective determination of ω, potentially misrepresenting true reservoir mobility; and the inherently limited resolution of mobility attributes derived from time-frequency decomposition methods.

2.4. Challenges of dispersion/attenuation-based methods

The model categories, theoretical bases, applicable conditions, advantages, and limitations of various dispersion/attenuation-based permeability prediction approaches are systematically compared in Table 2. This comparison reveals that despite the clear physical mechanisms underpinning this category of methods, four fundamental challenges persist: (i) controversies regarding the universality of petrophysical assumptions, such as deviations between assumed pore-scale homogeneity and actual reservoir heterogeneity, (ii) scale adaptability conflicts due to mismatched micro-mechanisms and macro-scale seismic observations, (iii) bandwidth limitations of seismic data, where the absent of low-frequency components induce significant fluid mobility estimation bias, and (iv) amplified solution non-uniqueness due to coupled controls of pore geometry, fluid viscosity, and fracture density on dispersion/attenuation responses.

3. Permeability prediction based on pore structure characteristics

Traditional seismic permeability prediction methods primarily rely on well-log or laboratory rock physics data. These methods establish optimal porosity and permeability relationships and then extrapolate these petrophysical correlations to seismic data for areal

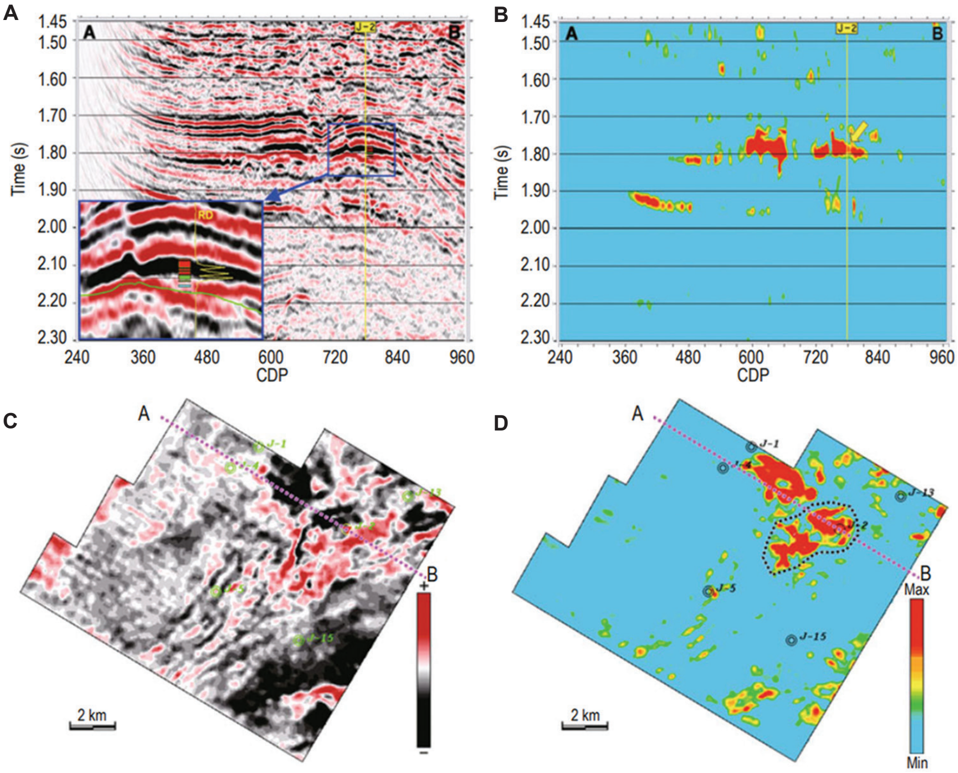

Figure 1. Fluid mobility analysis of reservoirs in the lower Ed2 formation from the JZ area. (A) Seismic section. (B) Fluid mobility reservoir section. (C) Seismic slice. (D) Fluid mobility reservoir slice. The colors red, green, and blue in the well log in the zoomed image indicate gas, oil, and brine, respectively. Reprinted with permission from Chen *et al.*[26] Copyright 2012 Editorial Office of Applied Geophysics and Springer-Verlag Berlin Heidelberg. Abbreviation: CDP: Common depth point.

Table 2. Theoretical and application characteristics of dispersion/attenuation-based methods

Model category	Theoretical basis	Applicable conditions	Advantages	Limitations
Model-based inversion	BISQ/BIPS theoretical models	Moderate-to-high porosity/permeability sandstones	Clear physical interpretation	Mismatch in strongly heterogeneous reservoirs
Velocity dispersion/quality factor-based methods	Velocity-frequency response	Broadband seismic data	High computational efficiency	Sensitive to Q-factor extraction errors
Fluid mobility-based methods	Low-frequency reflectivity theory	Fluid-saturated porous media	Direct indicator of flow capacity	Resolution constraints in time-frequency analysis

Abbreviations: BIPS: Biot-patchy-squirt; BISQ: Biot-Squirt.

permeability prediction.[30] However, due to depositional and diagenetic controls, carbonate reservoirs, particularly reef-shoal facies, exhibit significantly more complex pore architecture than clastic reservoirs. These reservoirs demonstrate substantial permeability heterogeneity even at comparable porosity levels. In lithofacies-varying formations with intricate pore systems, conventional methods yield compromised accuracy due to nonlinear porosity and permeability relationships. Consequently, pore structure integration becomes essential for reducing inversion non-uniqueness and enhancing prediction reliability.

There are currently three pore structure-based approaches: (i) Sun model-based inversion, (ii) lithofacies-constrained prediction using pore-structure parameters, and (iii) dual-porosity structure parameter integration.

3.1. Sun model-based methods

Sun[31,32] derived two pore structure parameters through fundamental rock physics analysis: the bulk compliance factor (γ), which characterizes volumetric rock deformation, and the shear compliance factor (γ_μ), which describes shape variations. Both γ and γ_μ satisfy the rock physics relationship:

$$K_d = K_m\,(1\text{-}\phi)^{\gamma} \tag{IX}$$

$$\mu_d = \mu_m (1-\phi)^{\gamma_\mu} \tag{X}$$

where K_d and μ_d denote the bulk modulus and shear modulus of dry rock, respectively; K_m and μ_m represent the bulk modulus and shear modulus of the grain mineral phase, respectively; and ϕ signifies porosity. Furthermore, γ_μ can be expressed as:

$$\gamma_\mu = \frac{\lg(V_s^2\rho) - \lg\mu_m}{\lg(1-\phi)} \tag{XI}$$

where V_s, ρ, and ϕ denote the S-wave velocity, density, and porosity, respectively.

Applied to Texas carbonate reservoirs by Dou *et al.*,[33] these parameters effectively characterized the relationship between porosity impedance and permeability. They facilitated the identification of pore types and high-permeability zones, thereby enhancing prediction accuracy. Zhang *et al.*[34] subsequently implemented these parameters in the Puguang Gas Field, with a pore structure-constrained porosity and permeability binary model developed for permeability-type classification at seismic scales. Similarly, Jin *et al.*[35] established pore-type discrimination criteria and type-specific porosity and permeability models using γ_μ. These achievements enabled refined well-log permeability interpretation. By analyzing elastic parameter-pore structure relationships across pore types, rock physics templates for the permeability prediction of complex reservoirs were constructed (Figure 2). In the case study of Puguang Gas Field (Figure 3), an intraparticle pore-dominated reservoir within the 5369–5440 m interval was developed in Well PG302-1. Although this section exhibited relatively high predicted porosity, the pore structure parameter was significantly low, indicating low permeability consistent with core analysis results. This case validates that permeability prediction based on pore structure parameters effectively discriminates reservoir flow capacity heterogeneity, thereby delineating the spatial distribution of high-permeability zones. Compared to conventional approaches, this method substantially enhances permeability prediction accuracy in complex reservoirs. Conventional methods rely on statistically derived empirical formulas for porosity and permeability, with prediction errors often exceeding one order of magnitude. Critically, these findings substantiate that pore structure exerts dominant control over permeability, whereas porosity serves merely as a contributory factor.

The Sun model demonstrates porosity-independent permeability prediction capabilities in both carbonate and clastic reservoirs. It achieves this through its characterization of rock deformation mechanisms through γ and γ_μ. However, the model suffers from fundamental flaws in its physical foundation. First, the model exclusively captures elastic deformation responses while neglecting the topological control mechanisms governing fluid pathways (e.g., pore-throat connectivity). Second, its classification regression framework contains inherent structural deficiencies: oversimplified permeability zoning based solely on γ or γ_μ results in ambiguous partition boundaries, and the enforcement of linear porosity and permeability regressions contradicts the intrinsic nonlinearity of

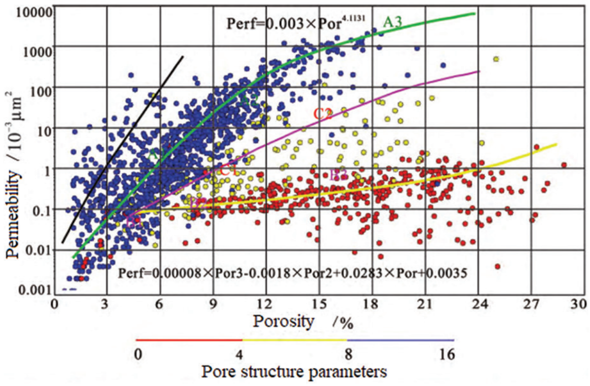

Figure 2. Permeability interpretation chart of Puguang Gas Field. Reprinted with permission from Jin *et al.*[35] Copyright 2016 Journal of Palaeogeography.

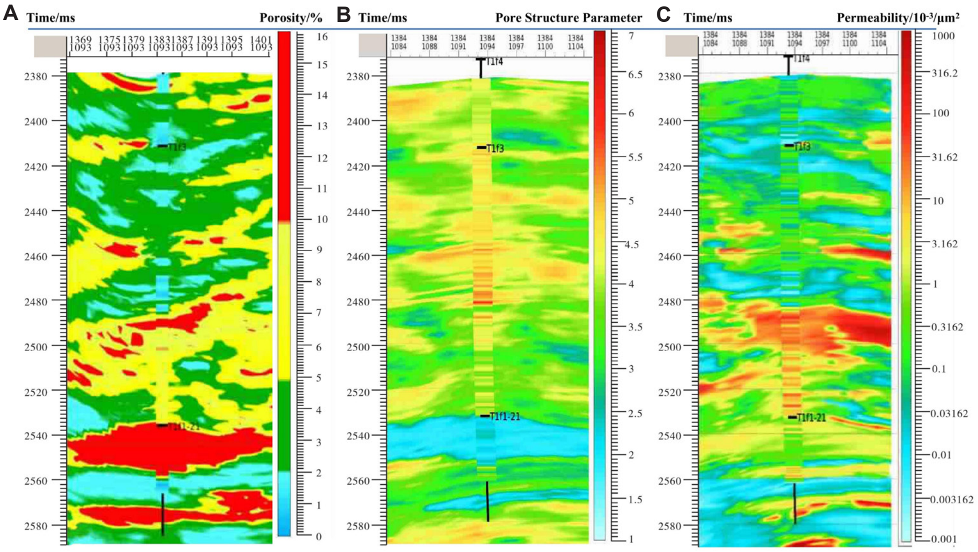

Figure 3. Inversion profiles of (A) predicted porosity, (B) pore structure parameter, and (C) permeability through Well PG302-1. Reprinted with permission from Jin *et al.*[35] Copyright 2016 Journal of Palaeogeography.

carbonate systems, particularly the exponential porosity–permeability relationships observed in vugular pore networks.

3.2. Lithofacies-controlled methods with pore structure parameters

Advancing quantitative reservoir characterization recognizes depositional microfacies as primary controls on petrophysical properties. Sedimentary attributes, including composition and grain size, fundamentally govern porosity and permeability distributions. Therefore, establishing microfacies-constrained property models is essential.

Zhao[36] derived facies-control factors from Archie's equation, integrating them with permeability through Kozeny's hydrodynamic formula to develop a facies-constrained permeability calculation method for seismic inversion. This approach demonstrably enhances lateral prediction accuracy by incorporating geological priors. Given the primary control of pore structure on permeability as introduced in Section 3.1, Gan *et al.*[37] developed a comprehensive workflow for reservoir permeability prediction integrating pore structure and lithofacies controls: First, lithofacies classification was conducted using the reservoir zone's porosity, elastic parameters, and γ_μ. Then, facies-specific multivariate regression was used for permeability prediction. Relying on this workflow, they selected the Fudong Slope area in the eastern central depression belt of the Junggar Basin as the study area for method application. The primary reservoir type in this region is lithologic-stratigraphic hydrocarbon accumulation. The study designated Well FUD7 as the training well and Well FUD6 as the prediction well. Regression relationships were separately established for different lithofacies in the training well. Subsequently, the trained lithofacies-specific regression models were applied to the prediction well to obtain permeability prediction results. Comparative analysis with non-facies-based multivariate regression in Table 3 reveals that both wells exhibited reduced prediction errors and enhanced coefficient of determination (R^2) values after facies-control implementation. The maximum error reduction and greatest R^2 improvement occurred when γ_μ was included in the regression parameters. Field applications demonstrate that this method can confine permeability prediction errors within one order of magnitude, and multivariate regression proves to be a viable solution for reservoir permeability prediction as it incorporates elastic parameters and γ_μ under lithofacies constraints.

While lithofacies-controlled methods enhance prediction accuracy through depositional microfacies constraints, precise lithofacies classification remains a prerequisite for permeability prediction, as it serves as a geological prior. Furthermore, γ_μ exhibits extreme sensitivity to velocity and density errors in seismic inversion. Acting as a key input for lithofacies classification, it forms a positive error feedback loop propagating through the workflow. Strong multicollinearity also exists among porosity, γ_μ, and impedance in multivariate regression. This multicollinearity distorts the physical significance of the regression coefficients, and these factors collectively cause abrupt lateral prediction jumps exceeding one order

Table 3. Statistics of mean square error (MSE) and coefficient of determination (R^2) for multivariate regressions

Key input parameters	Facies-based	Fud7 well		Fud6 well	
		MSE	R^2	MSE	R^2
ϕ	No	0.9599	0.4392	1.5056	0.3269
	Yes	0.9387	0.5067	1.2961	0.5250
$\phi+Vp$	No	0.9569	0.4409	1.4026	0.3508
$\phi+Vp/Vs$	No	0.9239	0.4602	1.4014	0.3921
$\phi+\gamma_\mu$	No	0.7765	0.5463	1.3564	0.4961
$\phi+Vp+Vp/Vs$	No	0.8975	0.4757	1.0756	0.4989
	Yes	0.8924	0.5408	0.9542	0.5925
$\phi+Vp+Vp/Vs+\gamma_\mu$	No	0.7421	0.5664	0.9356	0.6016
	Yes	0.6721	0.7948	0.8943	0.7924

γ_μ indicates shear compliance factor; ϕ indicates porosity; V_P indicates P-wave velocity; V_s indicates S-wave velocity.

of magnitude. In summary, the limitations of this method include: High sensitivity to seismic lithofacies and pore structure parameters that are intrinsically challenging to quantify accurately; prevalent multicollinearity in multivariate regression; and multiple pore structure factors must be incorporated, given the multivariate nature of permeability controls.

3.3. Dual-pore-structure parameters methods

Wei and Innanen[38] discovered the combined effects of pore morphology and scale on permeability, establishing a dual-parameter model:

$$\kappa = A\phi^{B}\left(\frac{\phi}{C}\right)^{0.5-\gamma_p} \quad \text{(XII)}$$

where

$$\gamma_p = W_p\gamma_s + (1-W_p)(1-\gamma_c) \quad \text{(XIII)}$$

where κ represents permeability; γ_s and γ_c denote scale and roundness parameters, respectively; W_p is a weighting coefficient determined from the core and log data; and A, B, and C are undetermined coefficients. Inspired by the Sun model in Section 3.1, and guided by the lithofacies-control rationale established in Section 3.2, Ding *et al.*[39] derived a shear-Lee factor (c_μ) from the Lee model. This factor exhibited a strong linear correlation with principal pore dimensions. By incorporating this factor, they effectively integrated both pore-scale and morphological effects. In addition, they integrated the factor with elastic parameters, porosity, and pore aspect ratios (α) as inputs for a feedforward neural network to predict lithofacies, and then subsequently predicted permeability, ultimately constraining prediction errors within half an order of magnitude. Field application (Figure 4) in the tight gas reservoirs of the Shaximiao Formation, Jinqiu Gas Field, Sichuan Basin, demonstrated that predictions incorporating dual-pore-structure parameters ($c_\mu+\alpha$) achieved superior outcomes compared to single-factor (γ_μ) approaches. These predictions quantitatively matched well-logs with higher fidelity and generated sand bodies with enhanced spatial continuity.

The dual-pore-structure parameter approach demonstrates progress in characterizing the combined effects of pore morphology and scale on permeability. However, it suffers from inherent limitations in its physical mechanisms. The model oversimplifies complex flow processes into a power law combination of morphology and scale, neglecting the fundamental control of pore topology connectivity (e.g., tortuosity of pore throats). More critically, the parameterization exhibits irresolvable ambiguity: the model fails to distinguish the opposite effects on permeability between the real-scale expansion of pore throats and the morphological distortion caused by the flattening of sheet-like pores. In industrial applications, high-dimensional inversion spaces introduce significant uncertainties: the Wei model requires simultaneous resolution of multiple interacting parameters. Its high-dimensional solution space causes pronounced oscillation in inversion results. Meanwhile, Ding's neural network framework faces triple error propagation: inherent errors in elastic parameters derived from seismic inversion directly propagate into the calculation of the shear-Lee factor. This propagation induces intermediate parameter bias. Subsequent coupling of multi-source inputs in hidden layers of the feedforward network further iteratively amplifies upstream errors through weight matrices, ultimately generating substantial errors in the output layer's permeability predictions.

3.4. Challenges of pore structure characteristics-based methods

Although existing mainstream porosity and permeability prediction models (e.g., Sun, Wei, and Ding models) demonstrate progress in specific scenarios or mathematical formulations, they still suffer from fundamental limitations, as summarized in Table 4 regarding their methodologies, advantages, and constraints. These limitations include their core physical mechanisms, such as the neglect of pore-throat connectivity control and the ill-defined physical interpretations of parameters; model architecture, such as arbitrarily imposed linearization and error-amplifying designs; and application feasibility, such as dependence

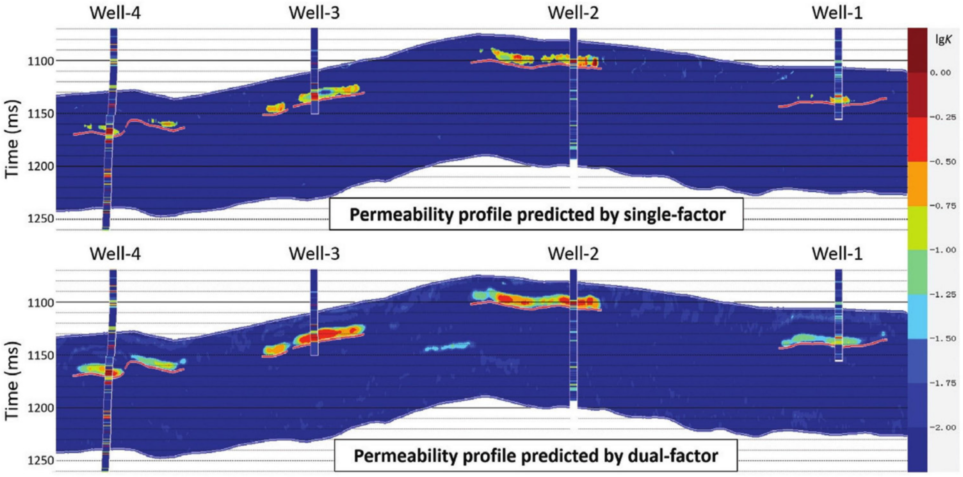

Figure 4. Predicted permeability profiles, where dual-pore-structure parameters refer to $c_\mu+\alpha$ and single-factor denotes γ_μ. Reprinted with permission from Ding *et al.*[39] Copyright 2023 Society of Exploration Geophysicists.

Table 4. Theoretical and application characteristics of pore structure characteristics-based methods

Dimension	Sun model	Lithofacies-controlled model	Dual-parameter model
Principle	Rock physics	Sedimentology	Morphology+scale
Key input parameters	Bulk compliance factor and shear compliance factor	Lithofacies type, pore structure parameters	Scale parameter, roundness parameter
Parameter acquisition	Seismic/log elastic parameter inversion	Core calibration+seismic lithofacies division	Core calibration+seismic/log elastic parameter inversion
Lithofacies dependent	No	Yes	Optional
Advantages	Porosity-independent heterogeneity characterization	Geological prior integration reduces non-uniqueness	Morphology+scale
Limitations	Oversimplified classification ignores multi-factor coupling	Subjectivity in lithofacies delineation	High-dimensional parameter instability, dependent on upstream parameter accuracy
Reservoir applicability	Carbonate/clastic reservoirs	Highly heterogeneous carbonates/clastic reservoirs	Fracture-porosity systems
Prediction accuracy	Error≤1 order of magnitude	Error≤1 order of magnitude	Error≤0.5 order of magnitude
Reference	Jin *et al.*[35]	Gan *et al.*[37]	Ding *et al.*[39]

on difficult-to-acquire/high-error parameters and high-dimensional inversion instability with non-unique solutions.

4. Permeability prediction based on AI

In recent years, AI algorithms have emerged as powerful computational tools for solving complex non-linear mapping and high-dimensional data fitting problems. They trigger transformative advances across scientific and engineering domains. Within petroleum exploration, the inherent subsurface complexity and uncertainty present significant challenges. These challenges, combined with substantial human capital demands for analyzing massive exploration datasets, have accelerated the industry-wide integration of AI technologies.[40-43]

4.1. Data-driven AI approaches

The earliest Chinese research on seismic-driven permeability prediction traces back to a groundbreaking study published in Oil Geophysical Prospecting by Chen and Guo.[30] Grounded in the elastic wave theory of dual-phase media, the authors established the theoretical basis for permeability prediction from seismic data. They demonstrated that conventional approaches relying solely on porosity and permeability functional relationships could only delineate qualitative permeability trends. To enable quantitative prediction, they pioneered the integration of mathematical approximation techniques with seismic attributes. As seismic attribute and permeability relationships defy explicit mathematical formulation, AI serves as an advanced regression tool that correlates well-log permeability with adjacent seismic traces. This calibrated relationship can then be extrapolated across 3D seismic volumes for reservoir permeability prediction.

Based on Chen's work, He *et al.*[43] implemented the rough set theory for optimal attribute selection, followed by genetic algorithm-optimized backpropagation neural networks to establish attribute and permeability mappings. Anifowose *et al.*[44] conducted a comparative analysis of multiple algorithms for permeability estimation in Middle Eastern carbonates. The study used integrated seismic attributes and wireline logs. The algorithms evaluated include artificial neural networks, fast Newman algorithm, support vector machines, and extreme learning machines. Meanwhile, Zhen *et al.*[45] integrated a convolutional block attention module into a convolutional neural network to characterize sand-body development patterns and identify concealed channels.

Riyadi *et al.*[46] proposed a permeability estimation method utilizing elastic attributes derived from simultaneous seismic inversion and evaluated the predictive performance of several ensemble-based models, including extreme gradient boosting (XGBoost), light gradient boosting (LightGBM), categorical gradient boosting, bagging regressor, random forest, and stacking. A multilayer perceptron neural network algorithm was also assessed. They focused on the X Field in the Malay Basin, characterized by complex pore systems (coexisting intergranular pores, dissolution vugs, and fractures) and pronounced heterogeneity. The statistical evaluation of permeability prediction models was based on wireline logging data using the R^2 and root mean squared log error (RMSE). The results revealed that integrating porosity with elastic properties as combined input features yielded $R^2 > 0.95$ and root mean squared log error (RMSLE) < 0.174. Among the tested algorithms, LightGBM and stacking ensemble models delivered optimal performance ($R^2 = 0.97$, RMSLE = 0.112 for both), while random forest exhibited relatively inferior results (R^2 = 0.92, RMSLE = 0.174). In contrast, predictions using elastic properties alone demonstrated significantly reduced accuracy, with R^2 ranging from 0.82 to 0.87, and RMSLE from 0.195 to 0.278. Within this feature configuration, XGBoost achieved the highest precision (R^2 = 0.87, RMSLE = 0.195), closely followed by a multilayer perceptron with 16 hidden layers (R^2 = 0.87, RMSLE = 0.207). Figure 5 compares predicted and measured permeability from the best-performing models under both input scenarios. The contrast between the bottom panels in Figure 5 visually confirms substantial prediction challenges in low-permeability intervals (<0.001 mD) when exclusively using elastic properties. Collectively, these results demonstrate that feature selection and combination exert decisive influence on predictive efficacy even with high-performance models. This limitation arises because pore-throat dimensions, morphology, and connectivity—all critical controls on flow behavior—exert more dominant control in tight formations. In contrast, elastic properties have been proven insufficient to characterize such microstructural determinants of fluid transport.

Although purely data-driven AI models (black-box models) in the aforementioned studies enhanced the prediction accuracy of reservoir permeability, their fundamental flaw lies in intrinsic decoupling from the physical mechanisms governing fluid flow.

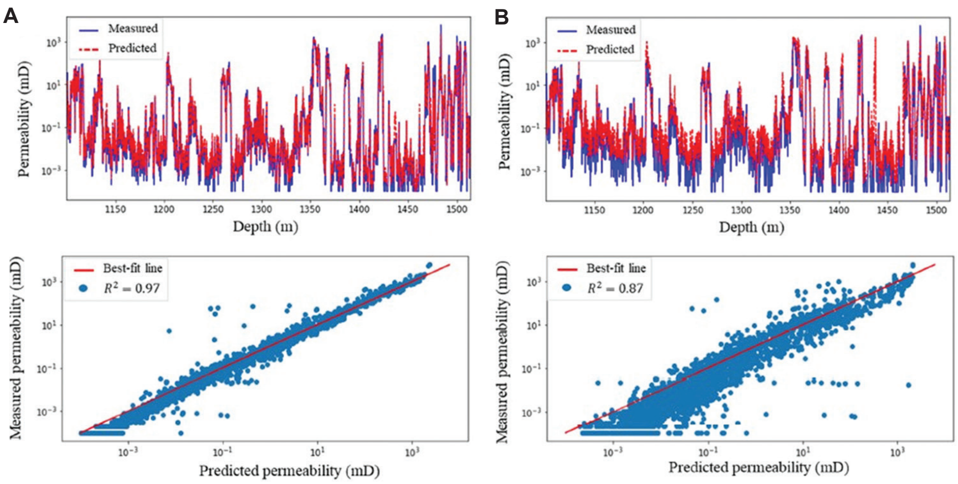

Figure 5. Measured and predicted permeability comparison. (A) Permeability prediction employing elastic properties and porosity as input features via the LightGBM modeling. (B) Elastic property-exclusive permeability prediction using the XGBoost framework. Top panels indicate depth-domain permeability profiles, while bottom panels illustrate cross-plots of predicted and core-calibrated permeability values. Reprinted from Riyadi *et al.*[46]

These methods simplify the prediction process to mathematical approximations, failing to construct genuine geologically process-driven models. The so-called "optimal feature combination" essentially represents over-adaptation to known geological conditions in training well areas. It is a feature mapping established through statistical correlations. When extrapolated to undrilled regions or complex diagenetic reservoirs, the geological plausibility of predictions becomes significantly questionable due to the absence of quantitative constraints on pore-throat network parameters. Furthermore, the inherent small-sample dilemma in reservoir parameter prediction inevitably subjects single-task learning to dual challenges of insufficient sample size and overfitting.

4.2. Data- and model-driven approaches

In 2019, Bergen *et al's*.[47] seminal review in *Science*, "Machine learning for data-driven discovery in solid earth geosciences," systematically evaluated applications of data-driven AI in solid earth sciences. The study emphasized that AI implementation must advance beyond simplistic applications to address complex geoscientific challenges. It highlighted that critical factors, such as training test set partitioning and validation methodology, significantly influence prediction outcomes. Traditional geophysical approaches typically formulate mathematical approximations between characterization parameters based on theoretical assumptions, resulting in deterministic physical models. Data-driven methods bypass theoretical presuppositions by directly extracting implicit patterns from data, making them well-suited for complex geological studies. However, they often lack physical interpretability. On the other hand, physical models offer stronger explanatory power, but they face limitations in accounting for geological complexity due to inherent assumptions and difficulties in defining inter-parameter relationships, ultimately constraining predictive accuracy. Recently, interdisciplinary collaboration has integrated data-driven methods with physical models. This integration has emerged as a promising avenue. It is deemed capable of yielding more universally applicable solutions to geophysical problems.[48-50]

The capillary bundle model provides the fundamental basis for studying fluid flow in porous media, representing the most essential physical model for permeability characterization. Its extension, the Kozeny-Carman equation, establishes the foundational relationship between porosity, pore-scale geometry, and permeability:[51]

$$\kappa = B\frac{\phi^3}{(1-\phi)^2}d^2 \qquad \text{(XIV)}$$

where κ represents permeability, ϕ represents porosity, d denotes pore scale (characteristic pore/grain size), and B is a geometric factor. On this basis, Bourbie *et al.*[52] proposed a practical formulation for application to natural materials, suggesting an empirical geometric factor n is 4 or 5, which may better represent common geological media:

$$\frac{\kappa}{d^2} \propto \phi^n \qquad \text{(XV)}$$

Shi *et al.*[53] incorporated pore-scale effects by calibrating n with well-log data, replacing Bourbie's proportionality with an explicit equality:

$$\frac{\kappa}{d_e^{\,2}} = \phi^n \qquad \text{(XVI)}$$

Where d_e represents the equivalent pore scale. To implement this permeability model, the authors first predicted porosity through sensitive parameter analysis. They used bulk modulus, shear modulus, and density with kernel Bayesian discrimination. Subsequently, they estimated the equivalent pore scale from compressional wave velocity, shear wave velocity, and the derived porosity using the same statistical method. Finally, permeability was calculated through the porosity-equivalent pore scale-permeability relationship using seismic elastic parameters. While this method introduces valuable physical constraints to data-driven prediction, there are two key limitations: on the one hand, the permeability model accounts for pore scale and porosity effects but neglects pore morphology influences. On the other hand, cumulative errors may significantly compromise prediction accuracy. These errors arise from the stepwise porosity-pore scale-permeability calculation.

Indeed, issues such as small sample sizes and overfitting are frequently encountered in the context of distributed computational cumulative errors and reservoir parameter prediction. At present, multi-task learning addresses these challenges by establishing end-to-end learning mechanisms and sharing feature information across different tasks. This approach effectively mitigates the overfitting often associated with single-task learning, thereby enhancing the generalization capability of the network model. However, since multi-task learning relies on cross-task feature transfer to enable information interaction, the correlation between tasks plays a decisive role in model performance.

A large amount of statistical data demonstrated a close correlation between porosity and permeability. Based on this, Wei *et al.*[54] proposed a seismic prediction method for reservoir permeability using multi-task learning. The method employed post-stack seismic data and P-wave impedance as network inputs, with well-log porosity and permeability serving as labeled data of the network. Through network training, an optimal network model was established by integrating near-well seismic and well-log data. Finally, reservoir porosity and permeability parameters between wells were simultaneously predicted. Application results from the tight gas reservoir in the Shaximiao Formation of Jinqiu Gas Field, Sichuan Basin, demonstrated high consistency between predicted permeability parameters of Sand Body No. 8 and actual drilling data, along with superior vertical and horizontal resolution.

4.3. Challenges of AI-based methods

While data-driven AI models demonstrate empirical efficacy in permeability prediction, their core limitation stems from divorcing mathematical approximations from underlying petrophysical mechanisms. This physics-agnostic approach manifests as an inability to construct genuine geological process-driven models, vulnerability to local overfitting through statistically derived feature mappings, and geologically implausible extrapolation in undrilled/complex diagenetic settings due to unconstrained pore-throat parameterization.

5. Discussion

This review synthesizes the fundamental limitations inherent in the three dominant methodologies within the reservoir permeability prediction domain (Table 5).

Based on these findings, the above limitations unequivocally indicate the necessary direction for next-generation models. These models must transcend empirical curve fitting through deep integration of multiscale physical mechanisms, quantitative pore structure characterization, and physics-embedded AI architectures. Ultimately, this integration will dismantle the barriers between data-driven and physical models to achieve a paradigm shift.

Future development must focus on establishing a new permeability prediction paradigm centered on the synergistic optimization of “physical mechanism, data-driven approach, and engineering validation” (Figure 6):

(i) Theoretical mechanism innovation
  a. Develop coupled models integrating pore, fluid, and fracture system interactions with dispersion/attenuation signatures, deepening the coupled flow and elasticity theory for multi-porosity media (e.g., pores, vugs, and fractures).
  b. Advance pore-throat topology-constrained rock physics models to quantify the control weights of tortuosity and connectivity on permeability.

(ii) Data-driven architecture enhancement
  a. Construct multimodal physics-guided learning networks by fusing multi-source data (e.g., seismic attributes, electrical imaging, and nuclear magnetic resonance).
  b. Employ deep generative adversarial models to synthesize geologically realistic virtual samples (e.g., generating low-frequency signals to extend bandwidth and compensate for flow capacity calculations), thereby overcoming the bottleneck of scarce training data.

(iii) Deep embedding of physical mechanisms
  a. Deeply embed differentiable forms of fundamental physical laws (e.g., Darcy’s law and Biot’s theory) within neural networks.
  b. Develop cross-scale physics-informed neural networks to couple microscopic pore network simulations with macroscopic seismic responses.

(iv) Engineering validation framework
  a. Digital rock core simulation validation: Compare seismically inverted permeability against direct flow simulation results on the pore network to utilize computerized tomography scans/process-based modeling to create digital rock cores and validate the microscale mechanistic soundness and scale-transition capability of models.
  b. Blind well testing validation: Withhold data from key geological unit representative wells (blind wells) during model training and optimization, and assess spatial generalization capability and geological scenario adaptability by analyzing prediction errors (e.g., RMSE and relative error distribution) against core analysis/well test permeability data.
  c. Dynamic production history matching validation: Embed the seismically predicted 3D permeability field into reservoir simulators, use actual production dynamics (pressure, rates, water cut, etc.) as the benchmark, and quantify improvements, such as the reduction in history matching error and the enhancement of recovery factor prediction accuracy, thereby demonstrating the practical utility for development decision support.
  d. Dynamic data-driven model evolution: Trigger incremental learning and model re-optimization on acquiring new dynamic data (e.g., new drilling/core data, production tests, and 4D seismic data) and iteratively validate the performance of the updated model on new blind wells and subsequent production periods, ensuring continuous

Table 5. Summary of three methodological categories for seismic permeability prediction

Methodology		Limitation
Dispersion and attenuation	Theoretical model inversion	(a) Non-unique solutions and inherent uncertainty (b) Significant result discrepancies across methods (c) Frequent mismatch between theoretical predictions and field data
	Velocity dispersion/ quality factor	(a) Non-uniqueness in dispersion attributes from frequency-dependent AVO/AVA inversion (b) High relative error in quality factor extraction
	Fluid mobility attributes	(a) Uncertainty in optimal frequency selection (b) Low resolution of mobility attributes derived from time-frequency decomposition
Pore structure	Sun model	(a) Oversimplified pore-permeability classification using compliance factors alone; velocity data integration required (b) Overly simplistic linear porosity and permeability regression post-classification
	Facies-constrained pore structure parameters	(a) High sensitivity to seismic facies and pore structure parameters, both of which are challenging to quantify accurately (b) Multicollinearity in multivariate linear regression (c) Necessity of multi-parameter pore structure factors for permeability classification
	Dual-pore-structure parameters	(a) Uncertainty in quantitative permeability expressions due to numerous undetermined coefficients (b) Error propagation from elastic parameters in seismic inversion
Artificial intelligence	Data-driven approach	(a) Lack of physical models and theoretical constraints (b) "Small-sample" and overfitting issues in single-task neural networks for reservoir parameter prediction
	Data- and model-driven approaches	(a) Neglect of pore morphology effects in constraining physical models (b) Significant error accumulation from stepwise calculations degrades permeability prediction accuracy

Abbreviations: AVA: Amplitude variation with incident angle; AVO: Amplitude variation with offset.

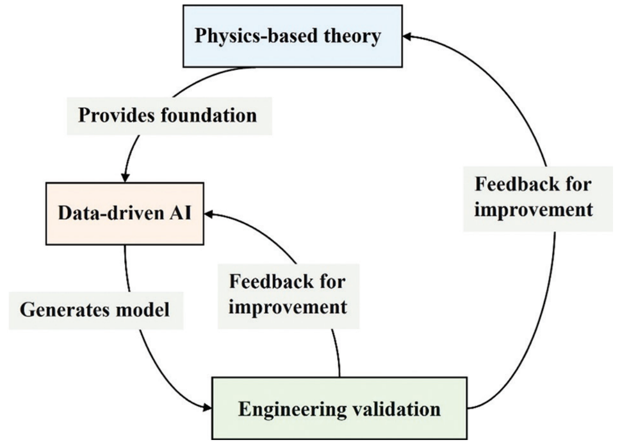

Figure 6. A proposed permeability prediction paradigm
Abbreviation: AI: Artificial intelligence.

predictive capability evolution throughout the field lifecycle.

This paradigm deeply embeds rock physics principles into neural network architectures. It achieves the unification of physical interpretability and prediction accuracy. For strongly heterogeneous reservoirs, such as fracture-vuggy carbonates and bioturbated sandstones, it enables reliable predictions at both exploration and development grades. Its closed-loop engineering validation mechanism provides quantifiable and iteratively improvable core technological support for intelligent oilfield development. This mechanism spans from digital rock core and blind well testing to history matching and dynamic evolution.

6. Conclusion

Reservoir permeability is critical for characterizing unconventional reservoirs and optimizing hydrocarbon recovery. However, its seismic prediction remains challenging due to the complex, non-explicit relationship between seismic responses and permeability, which is governed by multifaceted controlling factors. These challenges are specifically manifested in three dominant methodologies:

i. Dispersion/attenuation-based models, while grounded in explicit physical mechanisms, are constrained by the coupled interactions of pore, fluid, and fracture systems. This coupling leads to non-unique solutions, scale adaptability conflicts, and biases in fluid mobility characterization due to seismic bandwidth limitations.
ii. Pore structure methods (e.g., Sun's compliance factor) suffer from quantification uncertainties, primarily due to oversimplified morphological characterization and parameters with ambiguous physical interpretations.
iii. AI-based methods often decouple mathematical approximations from rock physics principles, resulting in a vulnerability to overfitting and geologically implausible extrapolation. Although integrating physics with AI has improved accuracy, critical deficiencies remain, including inadequate pore-throat

topology differentiation, underutilization of seismic dispersion, and limited efficacy in enforcing physical constraints.

Consequently, overcoming these fundamental limitations necessitates a new paradigm centered on the synergistic integration of multi-scale physical mechanisms, quantitative pore-structure characterization, and physics-embedded AI architectures. This integrated approach is essential to achieve a paradigm shift from empirical curve-fitting to theoretically guided forecasting in permeability prediction.

Acknowledgments

None.

Funding

This research was financially supported by the Research Project on Coalbed Methane Supporting Technologies for Gas Reservoir Evaluation (Grant No. 2025D4QP10) from PetroChina Changqing Oilfield Company, the China National Petroleum Corporation (CNPC) Tackling and Application Science & Technology Project (Grant No. 2023ZZ25-001), the PetroChina Science and Technology Project (Grant No. 2022KT1504), and the CNPC Forward-looking Fundamental Project (Grant No. 2021DJ3505).

Conflict of interest

We declare that we do not have any commercial or associative interest that represents a conflict of interest in connection with the work submitted.

Author contributions

Conceptualization: Lele Wei, Lideng Gan
Formal analysis: Lideng Gan, Hao Yang
Funding acquisition: Xinyu Li, Hao Yang
Visualization: Hao Yang
Writing–original draft: Lele Wei
Writing–review & editing: Gang Hao, Xiaoyu Jiang

Availability of data

Not applicable.

References

1. Webber KJ, Van Geuns LC. Framework for constructing clastic reservoir simulation models. *J Petrol Technol*. 1990;42(10):1248-1297.

   doi: 10.2118/19582-PA

2. Sahimi M. *Flow and Transport in Porous Media and Fractured Rock*. 2nd ed. United States: Wiley; 2011.

   doi: 10.1002/9783527636693.index

3. Suo Y, Guan W, Dong M, *et al*. Study on the heat extraction patterns of fractured hot dry rock reservoirs. *Appl Therm Eng*. 2025;262:125286.

   doi: 10.1016/j.applthermaleng.2024.125286

4. Razavirad F, Schmutz M, Binley A. Estimation of the permeability of hydrocarbon reservoir samples using induced polarization and nuclear magnetic resonance methods. *Geophysics*. 2018;84(2):1-76.

   doi: 10.1190/geo2017-0745.1

5. Yuan SY, Song CH, Tang GY, *et al*. inventors; China University of Petroleum (Beijing), assignee. *Yi Zhong Chu Ceng Shen Tou Lü Yu Ce Fang Fa, Zhuang Zhi Ji Cun Chu Jie Zhi [Reservoir Permeability Prediction Method, Device, and Storage Medium]*. CN patent CN111399044B. 2021.

6. Pride SR, Harris JM, Johnson DL, Mateeva A, Michael F. Erratum: Acquisition/processing--permeability dependence of seismic amplitudes. *Leading Edge*. 2003;22(7):698-698.

   doi: 10.1190/1.1603031

7. Nie JX, Yang DH, Yang HZ. Ji Yu Fei Bao He Duo Kong Jie Zhi BISQ Mo Xing De Chu Ceng Can Shu Fan Yan [Inversion of reservoir parameters based on the BISQ model in partially saturated porous media]. *Chin J Geophys*. 2004;47(6): 1101-1105.

   doi: 10.3321/j.issn:0001-5733.2004.06.024

8. Zhang XW, Wang DL, Wang ZJ, *et al*. Ji Yu BISQ Ji Zhi San Wei Shuang Xiang Zheng Jiao Lie Xi Ge Xiang Yi Xing Jie Zhi Shuai Jian Ji Pin San Fang Wei Te Xing Yan Jiu [The study on azimuth characteristics of attenuation and dispersion in 3D two-phase orthotropic crack medium based on BISQ mechanism]. *Chin J Geophys*. 2010;53(10):2452-2459.

   doi: 10.3969/J.Issn.0001-5733.2010.10.019

9. Fang Z, Yang D. Inversion of reservoir porosity, saturation, and permeability based on a robust hybrid genetic algorithm. *Geophysics*. 2015;80(5):R265-R280.

   doi: 10.1190/Geo2014-0502.1

10. Wu T, Li HX, Tao CH, Gu CH. Ji Yu Gai Jin Yi Chuan Suan Fa De BISQ Mo Xing Duo Can Shu Fan Yan Fang Fa Yan Jiu [The methodological study of multi-inversion of BISQ mold parameters based on modified genetic algorithm]. *Prog Geophys*. 2012;5:2128-2137.

    doi: 10.6038/J.Issn.1004-2903.2012.05.038

11. Yang L, Yang DH, Hao YJ, Nie JX. Duo Zhong Wu Li Ji Zhi Ou He Zuo Yong Xia De Chu Ceng Jie Zhi Can Shu Fan Yan Yan Jiu [A study on inversion of reservoir parameters under coupling interaction of multiple physical mechanisms]. *Chin J Geophys*. 2014;57(8):2678-2686.

    doi: 10.6038/cjg20140826

12. White JE. Computed seismic speeds and attenuation in rocks with partial saturation. *Geophysics*. 1975;40(2):

224-232.

doi: 10.1190/1.1440520

13. White JE, Mihailova N, Lyakhovitsky FM. Low-frequency seismic waves in fluid-saturated layered rocks. *J Acoust Soc Am*. 1975;57(S1):S30.

    doi: 10.1121/1.1995164

14. Johnson DL. Theory of frequency dependent acoustics in patchy-saturated porous media. *J Acoust Soc Am*. 2001;110(2):682-694.

    doi: 10.1121/1.1381021

15. Sun WT. On the theory of Biot-patchy-squirt mechanism for wave propagation in partially saturated double-porosity medium. *Phys Fluids*. 2021;33(7):076603.

    doi: 10.1063/5.0057354

16. Xiong FS, Sun WT, Ba J, Carcione JM. Effects of fluid rheology and pore connectivity on rock permeability based on a network model. *J Geophys Res Solid Earth*. 2020;125(3):e2019JB018857.

    doi: 10.1029/2019JB018857

17. Wei LL, Gan LD, Xiong FS, Sun WT, Ding Q, Yang H. Ji Yu San Wei Kong Xi Wang Luo Mo Xing De Zong Bo Pin San Shuai Jian Te Zheng Fen Xi [Attenuation and dispersion characteristics of p-waves based on the three-dimensional pore network model]. *Chin J Geophys*. 2021;64(12):4618-4628.

    doi: 10.6038/Cjg2021p0496

18. Tan XH, Zhou XJ, Xu P, Zhu Y, Zhuang DJ. A fractal geometry-based model for stress-sensitive permeability in porous media with fluid-solid coupling. *Powder Technol*. 2025;455:120774.

    doi: 10.1016/j.powtec.2025.120774

19. Liu LH, inventor; Chengdu Crystal Petroleum Technology Co., Ltd., assignee. *Yi Zhong Li Yong Die Qian Di Zhen Pin San Fen Xi Yu Ce Chu Ceng Shen Tou Lü De Fang Fa [A method for Predicting Reservoir Permeability Using Pre-Stack Seismic Dispersion Analysis]*. CN patent CN103364834B. 2016.

20. Wu ZW, Guo S, Chen H, inventors; CNPC Chuanging Drilling Engineering Company Limited, assignee. *Ji Yu Di Zhen Pou Mian Pin Zhi Yin Zi Ji Suan Chu Ceng Shen Tou Lü De Fang Fa [A method for Calculating Reservoir Permeability Based on Seismic Profile Quality Factor]*. CN patent CN107589458B. 2019.

21. Müller TM, Gurevich B, Lebedev M. Seismic wave attenuation and dispersion resulting from wave-induced flow in porous rocks-A review. *Geophysics*. 2010;75(5):75A147-75A164.

    doi: 10.1190/1.3463417

22. Chen HZ. Estimating elastic properties and attenuation factor from different frequency components of observed seismic data. *Geophys J Int*. 2019;220(2):794-805.

    doi: 10.1093/gji/ggz476

23. Silin DB, Korneev VA, Goloshubin GM, Patzek TW. A hydrologic view on Biot's theory of poroelasticity. *Office of Scientific and Technical Information Technical Reports*; 2004.

    doi: 10.2172/822181

24. Goloshubin G, Silin D, Vingalov V, Takkand G, Latfullin M. Reservoir permeability from seismic attribute analysis. *Leading Edge*. 2008;27(3):376-381.

    doi: 10.1190/1.2896629

25. Goloshubin G, Van SC, Korneev V, Silin D, Vingalov V. Reservoir imaging using low frequencies of seismic reflections. *Leading Edge*. 2006;25(5):527-531.

    doi: 10.1190/1.2202652

26. Chen XH, He ZH, Zhu SX, Wei L, Zhong WL. Seismic low-frequency-based calculation of reservoir fluid mobility and its applications. *Appl Geophys*. 2012;9(3):326-332.

    doi: 10.1007/s11770-012-0340-6

27. Zhao LX, Yuan HM, Yang JK, *et al*. Mobility effect on poroelastic seismic signatures in partially saturated rocks with applications in time-lapse monitoring of a heavy oil reservoir. *J Geophys Res Solid Earth*. 2017;11:8872-8891.

    doi: 10.1002/2017jb014303

28. Lu L. *Frequency-Dependent Seismic Inversion Method for Fluid Mobility Prediction in Hydrocarbon Reservoirs*. China: China University of Petroleum (East China); 2019.

    doi: 10.27644/d.cnki.gsydu.2019.000781

29. Zhang YJ, Wen XT, Jiang L, Liu J, Yang JX, Liu SM. Prediction of high-quality reservoirs using the reservoir fluid mobility attribute computed from seismic data. *J Petrol Sci Eng*. 2020;190:107007.

    doi: 10.1016/j.petrol.2020.107007

30. Chen ZD, Guo AH. Di zhen shu ju yu ce shen tou lv wen ti de tao lun [Discussion on permeability prediction with seismic data]. *Oil Geophys Prospect*. 1998;S2:86-90.

31. Sun YF. Core-log-seismic integration in hemipelagic marine sediments on the eastern flank of the Juan de Fuca Ridge. *Proc Ocean Drilling Program Sci Results*. 2000;168:21-35.

    doi: 10.2973/odp.proc.sr.168.009.2000

32. Sun YF. Pore structure effects on elastic wave propagation in rocks: AVO modelling. *J Geophys Eng*. 2004;1(4):268-276.

    doi: 10.1088/1742-2132/1/4/005

33. Dou QF, Sun YF, Sullivan C. Rock-physics-based carbonate pore type characterization and reservoir permeability heterogeneity evaluation, Upper San Andres reservoir, Permian Basin, west Texas. *J Appl Geophys*. 2011;74(1):8-18.

    doi: 10.1016/j.jappgeo.2011.02.010

34. Zhang HR, Sun YF, Dou QF, Zhang TT. Kong xi jie gou can shu zai pu guang qi tian de chu bu ying yong [Preliminary application of the frame flexibility factor in Puguang gas field]. *Oil Gas Geol*. 2012;33(6):877-882.

    doi: 10.11743/ogg20120608

35. Jin XJ, Hou JG, Liu HL, Zhang JX, Liu H. Pu Guang Qi Tian Jiao Tan Xiang Fu Za Kong Xi Lei Xing Chu Ji Ceng Shen Tou Lv Di Zhen Yu Ce Fang Fa [Seismic prediction method of permeability of reef bank reservoir with complex pore types in Puguang Gasfield]. *J Palaeogeogr*. 2016;18(2):275-284.

    doi: 10.7605/gdlxb.2016.02.021

36. Zhao RK. *Fine Reservoir Prediction Under Facies-Constrained Framework*. Chengdu: Chengdu University of Technology; 2014.

37. Gan LD, Wang YJ, Luo XZ, *et al.* Ji Yu Kong Xi Jie Gou Can Shu De Xiang Kong Shen Tou Lv Di Zhen Yu Ce Fang Fa [A permeability prediction method based on pore structure and lithofacies]. *Petrol Explor Dev*. 2019;46(5):935-942.

    doi: 10.1016/S1876-3804(19)60250-8

38. Wei XC, Innanen K. Prediction of reservoir parameters with seismic data. *CREWES Meeting Poster;* 2019; 31, no. 33. Available from: https://www.crewes.org/Documents/Posters/posters.php?year=2019 [Last accessed on 15 Oct 2025].

39. Ding Q, Gan LD, Wei LL, *et al*. Permeability prediction based on dual seismic pore structure factors. *Geophysics*. 2023,88(3):M173-M184.

    doi: 10.1190/geo2022-0411.1

40. Reichstein M, Camps-Valls G, Stevens B, *et al*. Deep learning and process understanding for data-driven Earth system science. *Nature*. 2019;566(7743):195-204.

    doi: 10.1038/s41586-019-0912-1

41. Xu CC, Misra S, Srinivasan P, *et al.* When Petrophysics Meets Big Data: What can Machine Do? In: *SPE Middle East Oil and Gas Show and Conference*; 2019.

    doi: 10.2118/195068-MS

42. Xu LL, Du ZY, Cai MF, *et al*. Sparse data-driven knowledge discovery for interpretable prediction of permeability in tight sandstones. *Eng Geol*. 2025;353:108151.

    doi: 10.1016/j.enggeo.2025.108151

43. He Y, Peng W, Yin J. Li Yong Di Zhen Shu Xing Yu Ce Shen Tou Lv [Permeability Prediction by Seismic Attribute Data]. *Acta Petrol Sin*. 2001;6:34-36.

    doi: 10.3321/j.issn:0253-2697.2001.06.007

44. Anifowose F, Abdulraheem A, Al-Shuhail A. A parametric study of machine learning techniques in petroleum reservoir permeability prediction by integrating seismic attributes and wireline data. *J Petrol Sci Eng*. 2019;176:762-774.

    doi: 10.1016/j.petrol.2019.01.110

45. Zhen Y, Zhang A, Zhao XM, Ge JW, Zhao Z, Yang CC. Prediction of deep low permeability sandstone seismic reservoir based on CBAM-CNN. *Geoenergy Sci Eng*. 2024;242:213241.

    doi: 10.1016/j.geoen.2024.213241

46. Riyadi ZA, Olutoki JO, Hermana M, Latif AHA, Yogi IBS, Kadir SJA. Machine learning prediction of permeability distribution in the X field Malay Basin using elastic properties. *Results Eng*. 2024;24:103421.

    doi: 10.1016/j.rineng.2024.103421

47. Bergen KJ, Johnson PA, De HMV, Beroza GC. Machine learning for data-driven discovery in solid Earth geoscience. *Science*. 2019;363(6433):eaau0323.

    doi: 10.1126/science.aau0323

48. Jia YN, Ma JW. What can machine learning do for seismic data processing? An interpolation application. *Geophysics*. 2017;82(3):V163-V177.

    doi: 10.1190/geo2016-0300.1

49. Yu SW, Ma JW. Deep learning for geophysics: Current and future trends. *Rev Geophys*. 2021;59(3):e2021RG000742.

    doi: 10.1029/2021RG000742

50. Xiao LZ. Ji Qi Xue Xi Shu Ju Qu Dong Yu Ji Li Mo Xing Rong He Ji Ke Jie Shi Xing Wen Ti [The fusion of data-driven machine learning with mechanism models and interpretability issues]. *Geophys Prospect Petrol*. 2022;2:205-212.

    doi: 10.3969/j.issn.1000-1441.2022.02.002

51. Carmen PC. Fluid flow through granular beds. *Chem Eng Res Des*. 1997;75:S32-S48.

    doi: 10.1016/s0263-8762(97)80003-2

52. Bourbie T, Coussy O, Zinszner B, Junger MC. Acoustics of porous media. *J Acoust Soc Am*. 1992;91(5):3080-3080.

    doi: 10.1121/1.402899

53. Shi L, Wang P, Liu JZ, Li JY, Wen LF, Chen XH. Zhi Mi Sha Yan Chu Ceng Wu Xing Can Shu Yu Ce Fang Fa Yan Jiu [Physical properties prediction for tight sandstone reservoirs]. *Geophys Prospect Petrol*. 2020;59(1):98-107.

54. Wei LL, Gan LD, Yang H, *et al.* Chu Ceng Shen Tou Xing Duo Ren Wu Zhi Neng Di Zhen Yu Ce Fang Fa [Multi-task learning-based intelligent seismic prediction of reservoir permeability]. *Geophys Prospect Petrol*. 2025;64(4):727-735.

    doi: 10.12431/Issn.1000-1441.2024.0285

ACCSCIENCE PUBLISHING

Journal of Seismic Exploration

ARTICLE

Application of distributed helically wound cable technology in ground seismic exploration

Jingyuan Wang*, Bin Liu, Jing Zhu, and Weiwei Duan

Research and Development Center of Science and Technology, Sinopec Geophysical Corporation, Nanjing, Jiangsu, China

Abstract

Fiber optic distributed acoustic sensing (DAS) based on phase-sensitive optical time-domain reflectometry holds significant potential for monitoring applications in seismic exploration, pipeline integrity, and border security. Conventional straight-fiber DAS systems are inherently limited to detecting single-component vibration signals along the fiber axis. To address this limitation, we propose a distributed helically wound cable (HWC). In this article, we present a theoretical analysis of the fundamental mathematical model governing HWC response and the selection criteria for an optimal spiral wrapping angle. We conducted a pioneering three-dimensional seismic field experiment in Xinghua, Jiangsu, China. An innovative underwater cable deployment scheme was implemented to ensure effective coupling between the cable and the surrounding medium. Experimental results demonstrated that HWC with a 30° wrapping angle yielded single-shot records characterized by a high signal-to-noise ratio and a broad effective frequency bandwidth, and enabled clear identification of shallow reflection events in stacked sections. This confirms the capability of HWC to acquire ground seismic reflection signals. Our findings provide an effective pathway for advancing next-generation fiber optic distributed seismic exploration technology.

Keywords: Helical wound cable; Surface seismic exploration; Wrapping angle; Fiber optic sensing; Distributed acoustic sensing

***Corresponding author:**
Jingyuan Wang
(paixing3933@163.com)

Citation: Wang J, Liu B, Zhu J, Duan W. Application of distributed helically wound cable technology in ground seismic exploration. *J Seismic Explor*. 2025;34(4):18-27. doi: 10.36922/JSE025300040

Received: July 21, 2025

1st revised: August 15, 2025

2nd revised: August 25, 2025

Accepted: August 25, 2025

1. Introduction

Distributed optical fiber distributed acoustic sensing (DAS) technology is a new optical fiber sensing technology that uses optical fibers as sensors and achieves vibration signal acquisition based on Rayleigh scattering of light. It offers advantages including low cost, high measurement accuracy, immunity to electromagnetic interference, and ease of installation.[1,2] Compared to conventional single-point and quasi-distributed sensors, DAS is more suitable for long-distance or high-resolution applications in time and space, and is widely used in oil exploration, pipeline leak monitoring, and border security monitoring.[3,4]

Driven by the promise of cost reduction and increased channel density, significant research efforts in recent years have focused on adapting DAS technology for seismic applications that are traditionally dominated by geophones and accelerometers. Researchers have explored its use for microseismic event detection and localization,[5] shallow near-surface characterization,[6] and vertical seismic profiling within boreholes,[7] and substantial progress has been made in fundamental theory, acquisition methodologies, processing algorithms, and interpretation techniques.[8,9] However, a persistent and fundamental challenge has hindered the widespread application of conventional DAS for surface seismic reflection surveys: its intrinsic directional sensitivity.

The underlying physics of phase-sensitive optical time-domain reflectometry-based DAS dictates that it is predominantly sensitive to strain components acting along the longitudinal axis of the optical fiber (axial strain), while exhibiting minimal response to strain perpendicular to this axis (radial strain).[10,11] Consequently, a straight optical fiber deployed horizontally on the surface acts as a highly directional sensor, primarily detecting seismic waves propagating along its length. This "single-component" nature is ideal for applications like vertical seismic profiling (where the fiber is near-vertical) or strain monitoring along pipelines. However, it renders standard DAS largely insensitive to the dominant energy arriving from near-vertical reflections in surface seismic exploration, where the fiber cable is typically laid horizontally, and the energetic reflected waves arrive almost perpendicularly to it. This critical mismatch in sensitivity direction has been the primary barrier preventing DAS from replacing conventional geophone arrays for land seismic acquisition.

To overcome this fundamental limitation of axial-strain-only sensitivity, Hornman *et al.*[12] pioneered the concept of the helically wound cable (HWC). The core innovation involves coiling the sensing optical fiber into a helical structure around a central strength member or mandrel within the cable jacket. This geometric transformation is pivotal; when seismic waves impinge on the cable, inducing complex strains within its structure, the helical path of the fiber ensures that its local axis has significant components in both the radial and tangential directions relative to the cable's cross-section. As a result, the fiber experiences strain components related to both compressional waves (P-waves; causing volume changes) and shear waves (S-waves; causing transverse particle motion). This multi-component sensitivity significantly enhances the DAS system's responsiveness to the diverse wave types and arrival directions encountered in surface seismic exploration, making its application in this domain theoretically feasible. Wuestefeld and Wilkd[13] advanced the understanding by employing precise ray tracing in complex velocity models to determine wave incidence angles and further elucidated the intricate relationships between subsurface medium properties, the mechanical properties of the DAS cable's wrapping materials, and the optimal helical wrapping angle for maximizing signal fidelity.[13] Furthermore, Innanen[14] developed sophisticated mathematical models for helical fibers wound along arbitrarily curved axes, specifically addressing the challenges of strain tensor estimation and the reconstruction of P-wave and S-wave signals from the measured DAS data.[14,15] These models have also been instrumental in forward modeling and inversion studies of seismic elastic waves using DAS data.[16-18] Despite these significant theoretical and simulation advances, rigorous experimental validation of HWC performance under realistic field conditions, particularly through direct comparison with established geophone arrays in three-dimensional (3D) seismic surveys, remains relatively scarce and represents a crucial research gap that needs bridging for technology maturation.

To directly address the core limitation of standard straight-fiber DAS for surface seismic—its inability to capture near-vertical reflections—this study focuses on the development, theoretical underpinning, and comprehensive field testing of a distributed HWC system designed explicitly for land seismic exploration. Based on a detailed theoretical analysis of the fundamental mathematical model governing strain transfer in helical fibers under seismic excitation, an optimal spiral wrapping angle was selected to maximize sensitivity to vertically incident waves while ensuring robust performance across a range of angles. We then conducted a pioneering 3D seismic field experiment in Xinghua, Jiangsu, China, implementing a novel underwater deployment strategy to ensure effective cable-medium coupling—a critical factor often challenging to achieve with conventional trenching or surface-laid methods, especially for kilometer-scale cables. The primary objective was to empirically evaluate the HWC's ability to acquire genuine surface seismic reflection signals, assess its data quality relative to conventional nodal systems, and validate its practical feasibility for next-generation seismic acquisition.

2. Design and theoretical analysis of a distributed HWC

In oil and gas exploration applications, distributed optical cables function as sensors to detect weak seismic waves. When a light pulse propagates along the optical fiber core, Rayleigh scattering occurs due to inhomogeneities within the fiber. The system detects the backward-scattered Rayleigh light, generating an interference pattern. When external forces such as sound pressure act on the optical cable, the optical fiber will be strained, and the interference image will change. By detecting the change, the amplitude of the seismic wave can be reconstructed. As compressional waves (P-waves) are predominantly used in seismic exploration and generate strain parallel to their propagation direction, this study focuses on P-waves as the research object. If a plane P-wave propagates along the D-axis, then the unique non-zero strain component along this axis is denoted as $e^{(w)}$. Suppose the optical cable is oriented at an angle θ with respect to the D-axis, as shown in Figure 1. The direction of e_z is parallel to the axial direction of the fiber, and the direction of $e_{||}$ is parallel to the axial direction of the optical cable. Strain $e^{(w)}$ is a second-order tensor, and its component $e_{||}^{(w)}$ along the parallel direction of the optical cable length is $e^{(w)}\cos^2\theta$. If the fiber is well coupled with the optical cable, the optical cable is well coupled with the external structural layer, and there is no loss at the contact interface, then $e_{zz}^{(f)}= e_{||}^{(c)}=e^{(w)}$, i.e., the strain of the fiber is proportional to $\cos^2\theta$, independent of the optical cable material and the external structural layer parameters.

Based on the effect of seismic P-wave on the linear optical cable, the optical fiber is wound as shown in Figure 2. The optical fiber is tightly wound on the surface of the cylindrical optical cable shaft, cut along the direction AB of the left figure, and expanded to get the right figure. The wrapping angle α of the optical fiber is the angle between the optical fiber and the radial direction of the optical cable.

Suppose $b = |AB|$ in Figure 2, the circumference of the fiber wrapping cylinder, is $\alpha = 2\pi R$, and R is the radius of the cylinder, then the diagonal L of the rectangle on the right is the length of the fiber (**Equation I**):

$$\frac{\Delta L}{L}=\frac{a}{L^2}\frac{\Delta a}{a}+\frac{b^2}{L^2}\frac{\Delta b}{b} \tag{I}$$

When the optical cable generates strain under the action of seismic waves, its cross-section will become an ellipse. Let b_1 and b_2 be the length of the long axis and short axis of the ellipse, respectively, then the ellipse equation can be obtained as follows (**Equation II**):

$$\begin{Bmatrix} x=b_1\cos\beta \\ y=b_2\cos\beta \end{Bmatrix} \tag{II}$$

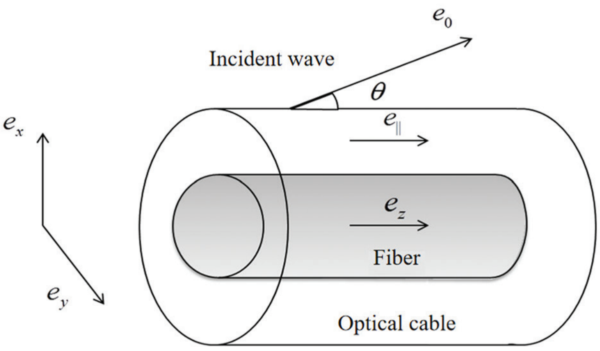

Figure 1. Schematic diagram of the effect of seismic waves on optical cables.

The circumference of the ellipse is $\tilde{a}=\pi(b_1+b_2)2\pi\tilde{R}$, where $\tilde{R}$ is the approximate radius of the ellipse, $\Delta a/a=\Delta R-R$, and $\Delta R=\tilde{R}-R$, then **Equation I** can be expressed as **Equation III**:

$$e_{ZZ}^{(ff)}=e_{||}^{(c)}\sin^2\alpha+\left\langle e_{rr}^{(c)}\right\rangle\cos^2\alpha \tag{III}$$

where α is the wrapping angle, $e_{ZZ}^{(ff)}=\frac{\Delta L}{L}$ is the axial strain of the optical fiber, $e_{||}^{(c)}=\frac{\Delta b}{b}$ is the axial strain of the optical cable, $\left\langle e_{rr}^{(c)}\right\rangle=\frac{\langle\Delta R\rangle}{R}$ is the radial strain of the optical cable, cos α = a/L, and sin α = b/L.

This relationship can be derived as follows (**Equation IV**):

$$e_{ZZ}^{(f)}=e_{||}^{(w)}\sin^2\alpha+\frac{(\lambda+2N)e^{(w)}-(\lambda_c+2N)e_{||}^{(w)}}{2(\lambda_c+N_c+N)}\cos^2\alpha \tag{IV}$$

The internal strain of the loaded wave is taken as the unit strain, that is, $e^{(w)}=1$. According to the previous analysis, $e^{(w)}=\cos^2\theta$ can be expressed as follows (**Equation V**):

$$e_{ZZ}^{(f)}=\cos^2\theta\sin^2\alpha+\frac{(\lambda+2N)e^{(w)}-(\lambda_c+2N)e_{||}^{(w)}}{2(\lambda_c+N_c+N)}\cos^2\alpha \tag{V}$$

According to **Equation V,** the strain of the spiral fiber is related not only to the Lamme coefficient of the fiber and optical cable, but also to the wrapping angle and the incidence angle of the seismic wave. Without considering the fiber and optical cable material, the simplified **Equation V** can be obtained through **Equation VI**:

$$e_{ZZ}^{(f)}=\cos^2\theta\sin^2\alpha+\frac{1}{2}\cos^2\theta\cos^2\alpha \tag{VI}$$

According to **Equation VI**, when the wrapping angle of the fiber is constant, the relationship between the relative

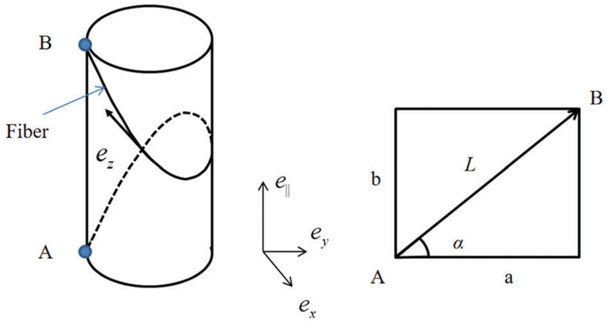

Figure 2. Schematic diagram of the distributed fiber wrapping.

fiber strain and the incidence angle of the seismic wave is shown in Figure 3. For the incident wave of the same angle, different wrapping angles will produce different optical fiber strains, and for the same wrapping angle, different angle incident waves will also produce different optical fiber strains. When α is 90°, the optical fiber is linear, the sensitivity is minimal, and the angle of incidence has the greatest influence on the relative strain. When α is 0°, the relative fiber strain is large, that is, the sensitivity is high, and the consistency is also affected by the incident angle. When the wrapping angle α is about 30°, the sensitivity is relatively large, and the consistency of the relative strain of the fiber is good.

To identify the optimal wrapping angle, we analyzed angles between 27° and 36° in 2° increments (Figure 3). At a wrapping angle of 33°, the fiber exhibits not only high sensitivity but also minimal variation in strain response across different incident angles.

According to **Equation VI**, the relationship between relative fiber strain and fiber wrapping angle is shown in Figure 4 when the incident angle is constant. When the incident angles are 0°, 20°, 40°, 60°, and 80°, there are two intersection points between 0 ~ π in the fiber wrapping angle, and the effect of the two intersection points on the fiber strain is the same. If one of the points is selected, its radius is 0.58; hence, the angle is 33°, and the strain generated at this point is the same for different incident angles. Thus, it has the same strain response characteristics.

3. High-definition (HD) distributed optical fiber acoustic wave sensing technology

HD-DAS is implemented based on the principle of self-coherent heterodyne demodulation,[19,20] with its schematic diagram as shown in Figure 5A. The system uses the optical signal modulation module to modulate the continuous light emitted by the ultra-narrow linewidth laser into a pair of pulses, where the two pulse frequencies are f_1 and f_2, respectively, and the heterodyne frequency is $\Delta f = f_1 - f_2$. The pulses are first amplified by the optical amplifier, and then injected into the sensing fiber through the circulator. The Rayleigh backscattered signal in the fiber reaches the signal detection module through the circulator and is then demodulated through the demodulation module for the heterodyne algorithm to obtain the phase change of the light wave caused by the external sound field. The system does not need the interference of Rayleigh scattering and local light, and the scattered light of the two pulses will interfere with each other to achieve a self-coherent effect. Then, the phase change caused by the external sound wave is modulated to the heterodyne frequency, and the high-precision phase signal can be obtained by a heterodyne demodulation algorithm. In addition, given that the noise environment experienced by the double pulse is the same, the common mode noise can be eliminated to a large extent after self-coherence, and the system can obtain a good noise background. Figure 5B shows the assembled HD-DAS system engineering prototype. Table 1 shows the specific technical specifications of the HD-DAS system.

4. Data acquisition

4.1. Acquisition of geometry design

The HWC seismic acquisition test was conducted within a 3D survey area located in Xinghua City, Jiangsu. The acquisition utilized a single-point high-density 3D geometry. The receiver array consisted of I-nodal and SmartSolo nodal units. The seismic source consisted of 3D explosive charges deployed in shot holes at 12 m depth with a shot interval of 40 m; a total of 100 shots were fired. The HWC receiver line (total length: 2 km) was positioned 200 m away from the shot line.

To extend the spatial coverage for comparative analysis, the HWC receiver array was repositioned three times as the shot points advanced. Each repositioning involved moving the HWC forward by 1 km. After three movements, seismic data covering a total profile length of 5 km were acquired (Figure 5).

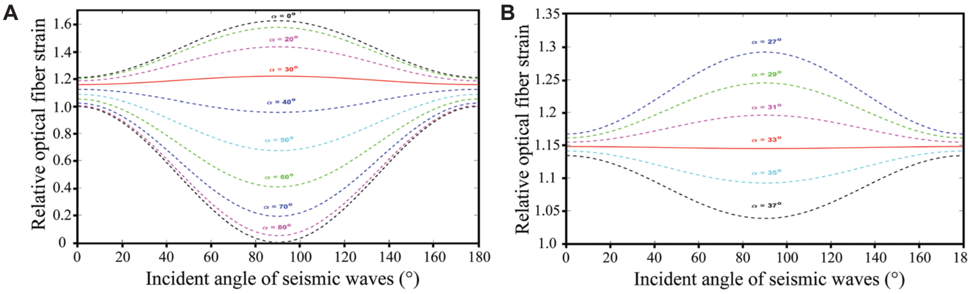

Figure 3. Relative optical fiber strains. Relation between relative fiber strain and (A) incidence angle and (B) local magnification.

Based on the theoretical analysis presented in Section 2 (Figures 3 and 4), a wrapping angle of approximately 30°–33° is identified as optimal for achieving high sensitivity to vertically incident waves while maintaining good angular response consistency. However, manufacturing HWC with a precise 30° wrapping angle presents significant process challenges and higher costs compared to angles closer to the natural lay of fibers, such as 60°. Theoretically, a 60° wrapping angle is expected to exhibit inferior acquisition performance, particularly for vertical waves. To quantitatively assess the impact of this parameter on field data quality and evaluate the viability of 60° HWC, the 2 km cable was constructed with two distinct segments: (i) an 860 m segment with a 60° wrapping angle, and (ii) a 1,140 m segment with a 30° wrapping angle.

In the receiver array layout, the 30° and 60° segments were concatenated into a single cable spanning the survey line, with the 30° segment occupying the northern 1,140 m (Traces 1–1,140) and the 60° segment the southern 860 m (Traces 1,141–2,000) (Figure 6). This placement ensured that data from segments with different wrapping angles were acquired under identical geological conditions, source characteristics, and near-surface effects. Directly comparing data quality between these segments under comparable field conditions provides an unambiguous assessment of the wrapping angle's impact on acquisition fidelity.

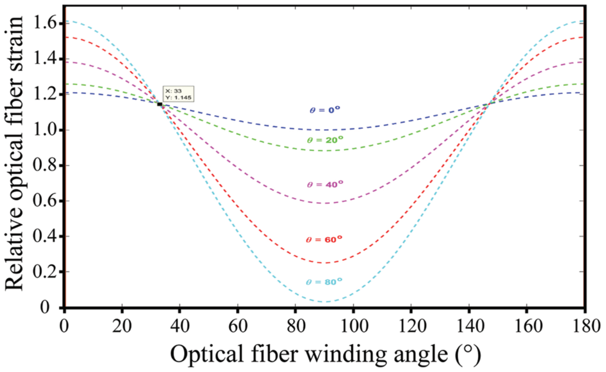

Figure 4. The relationship between the relative fiber strain and the fiber wrapping angle.

4.2. Deployment of HWC

Effective mechanical coupling between the HWC and the surrounding geological medium is paramount for high-quality seismic data acquisition. Poor coupling acts as a low-pass filter, attenuating high-frequency signal components, and introduces spurious noise, severely degrading signal-to-noise ratio and resolution. Common HWC deployment methods for surface seismic include:

(i) Trenching: Excavating deep trenches (typically >0.5 m) using machinery and burying the cable, providing good coupling but at high cost and environmental impact.

(ii) Surface laying: Placing the cable directly on the ground surface. This is logistically simple but results in very poor coupling efficiency and high susceptibility to

Table 1. High-definition distributed optical fiber acoustic wave sensing system technical specifications

Index item	Technical index value
Noise background ($dB\ ref\ rad/\sqrt{HZ}$)	−80
Stress resolution ($p\varepsilon/\sqrt{HZ}$)	2.5
Measurement bandwidth (kHz)	2
Spatial resolution (m)	1
Scale length (m)	8
Dynamic range (dB)	>100
Sensing distance (m)	50~2,500

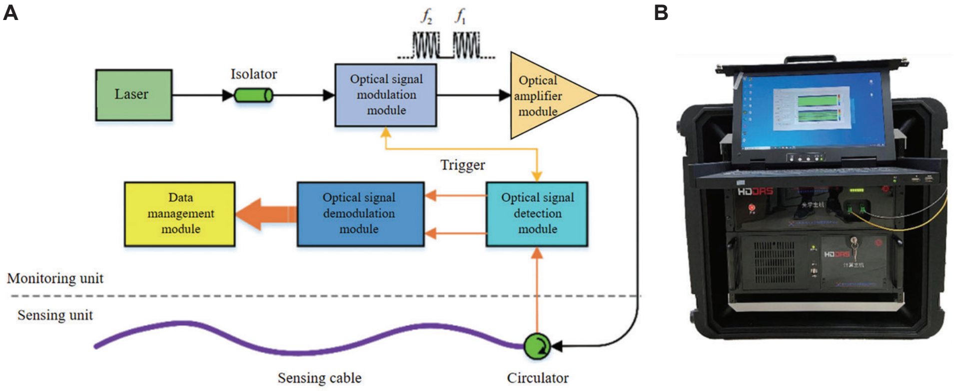

Figure 5. System overview and implementation. (A) High-definition distributed optical fiber acoustic wave sensing system principle and (B) engineering prototype.

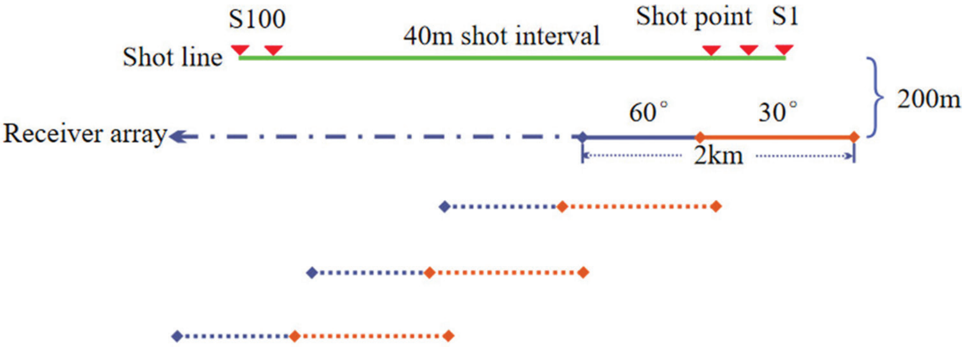

Figure 6. Schematic diagram of the helically wound cable acquisition geometry.

ground roll, wind noise, and cultural noise, leading to significantly degraded data quality.

While trench burial has been used in some international HWC trials, its applicability is often limited to relatively short cable lengths (typically <600 m in reported studies) due to the prohibitive cost and time required for excavating and reinstating long trenches. Given the 2 km length of our HWC and the requirement for three repositionings (totaling 5 km of cable deployment), conventional trench burial was deemed economically and logistically impractical.

To overcome this critical challenge and ensure effective coupling for the entire length of the cable during all deployment phases, we designed and implemented an innovative underwater deployment scheme. The HWC was carefully laid on the riverbed along the section parallel to the seismic line (Figure 7). Water provides excellent coupling due to its incompressibility and efficiently transmits seismic P-waves propagating as acoustic waves. Crucially, these acoustic waves in water fully retain the reflected P-wave information from subsurface structures, despite the difference in propagation velocity compared to the solid earth. This principle is supported by the theory of Ainslie,[21] which demonstrates that the dynamics of P-waves in fluids are analogous to those in solid media (lacking only the shear component), aligning perfectly with our objective of P-wave acquisition (Section 2.1). Repositioning the 2 km cable for the roll-along acquisition was efficiently achieved using a small tugboat (Figure 7), significantly reducing deployment time and cost compared to trenching.

5. Data analysis and results

5.1. Single-shot analysis

Figure 8A compares shot gathers acquired simultaneously by the 30° and 60° HWC segments. A significant performance contrast was evident: the left section (30° HWC) displayed recognizable seismic signals, particularly in shallow layers, despite interference from ground roll and other noise. Conversely, the right section (60° HWC) was severely contaminated by noise, resulting in a critically low signal-to-noise ratio that renders effective wave identification nearly impossible. Spectral analysis (Figure 8B) provided quantitative confirmation of the 30° segment's superiority. The amplitude spectrum of the 30° HWC data showed higher amplitudes across a broader frequency range than the 60° segment. Crucially, the 30° HWC demonstrated a significantly broader effective bandwidth, preserving more high-frequency content essential for achieving higher seismic resolution. The 60° segment's spectrum exhibited noticeable attenuation, particularly at higher frequencies, and lower overall energy, consistent with its noisy time-domain character.

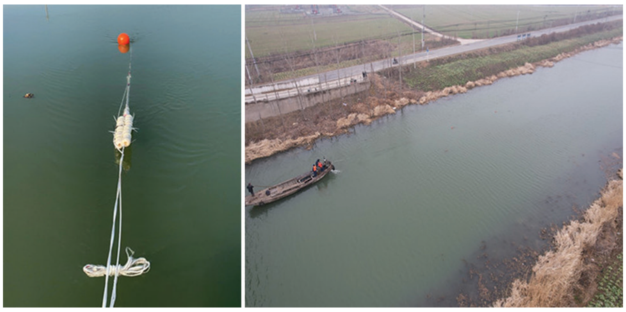

Figure 7. Field deployment documentation of helically wound cable.

The superior quality of the 30° HWC data enabled comparison with nodal acquisition. Comparison with nodal acquisition revealed key differences. The 30° HWC gather exhibited stronger ground roll amplitudes but weaker first arrivals compared to the nodal data, highlighting distinct sensor sensitivities and radiation patterns that warrant further investigation into coupling effects. Due to the shorter receiver spread length (2 km) and finer trace interval (1 m) of the HWC array, reflection hyperbolas appeared significantly flatter than those in the nodal gather. This fine spatial sampling is a key DAS advantage for high-resolution imaging, particularly of shallow, steeply dipping events.

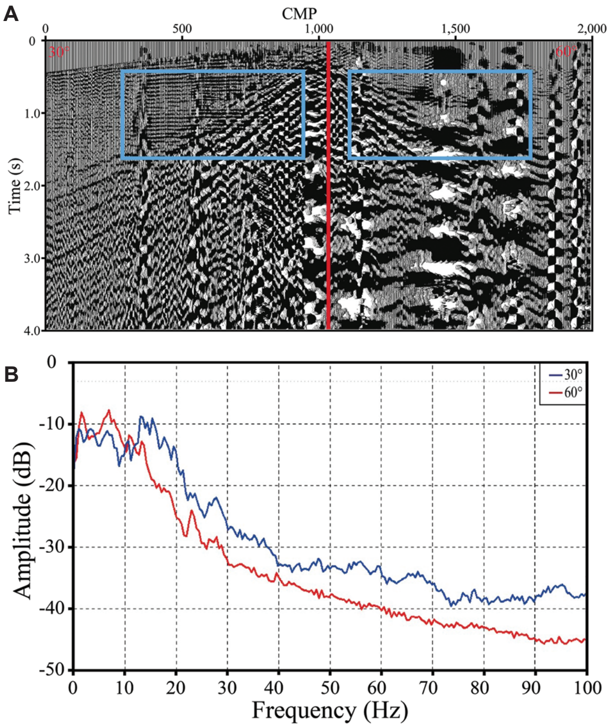

Figure 8. Performance comparison of shot gathers from different wrapping angles. (A) Shot records and (B) spectral analysis.
Abbreviation: CMP: Common midpoint.

Frequency-band scanning of the shot records (Figure 9) showed that effective reflection wave energy for both systems occupied a similar band (5–60 Hz). While waveform characteristics differed—likely due to sensor response, coupling, and directional sensitivity variations—the fundamental similarity in detected frequency content confirms both systems captured primary subsurface reflections. The HWC data showed good coherence within each filtered band, comparable to the nodal data.

5.2. Profile analysis

Given the extremely poor data quality of the 60° HWC segment (Figure 8A), incorporating it into the full processing flow would severely degrade the final stacked section. Consequently, we applied a split processing strategy during data conditioning. Data from the 30° and 60° sections were processed separately. While this isolation preserved the integrity of the 30° signals, it introduced significant compromises:

(i) Reduced fold coverage: The effective spread length contributing to any common midpoint bin was reduced (utilizing only the 30° or 60° segment, not the full 2 km cable).

(ii) Spatially inconsistent coverage: Fold coverage became highly variable along the profile, dropping sharply at the boundaries between segments and remaining low within each segment compared to the nodal array.

(iii) Dead trace zones: Some common midpoint bins, particularly at segment boundaries or due to the roll-along geometry, received zero coverage (“dead traces”), creating gaps in the stacked section (Figure 10 illustrates the discontinuous coverage).

Stacked profile comparisons between the 60° and 30° HWC segments (Figure 10) revealed significant differences. In the 60° stacked section (Figure 10A), reflection events were identifiable only in isolated, very shallow zones (likely corresponding to strong, near-surface reflectors). Throughout the vast majority of the section, reflection signals were scarcely discernible above the background noise. The overall data quality was markedly inferior, confirming the severely limited capability of the 60° HWC to effectively capture reflected wave energy under these field conditions. The theoretical prediction of inferior performance is strongly validated.

The 30° stacked section (Figure 10B), despite processing challenges (low/uneven fold, gaps), showed clear improvement. Continuous reflection events with reasonably coherent wave group characteristics were identifiable, particularly at shallow-to-intermediate depths (down to 1.0–1.5 s two-way time. This demonstrates the fundamental capability of the optimally designed 30° HWC to acquire coherent surface seismic reflections and produce a meaningful subsurface image, even under suboptimal acquisition conditions.

To further validate HWC feasibility, we compared the stacked profile from the 30° HWC segment with a nodal array profile acquired concurrently. The nodal profile benefited from single-point high-density acquisition and a fold coverage exceeding 800. The HWC profile faced inherent limitations: a short total cable length (2 km), separate processing of segments reducing effective spread length, and the roll-along geometry, resulting in extremely uneven fold coverage with a maximum of only 55.

Despite a significantly lower fold, the 30° HWC profile (Figure 11A) displayed clear reflection events with reasonably continuous wave groups. The fine 1-meter trace spacing of the HWC provides superior vertical and horizontal resolution in the shallow section compared to the nodal profile. However, the limited maximum offset (~1.4 km) resulted in weaker mid-to-deep section reflections. Nevertheless, reflection events consistent with the nodal profile were observable in the mid-to-deep section (ellipse, Figure 11A), though with weaker amplitudes and poorer continuity, constrained by the

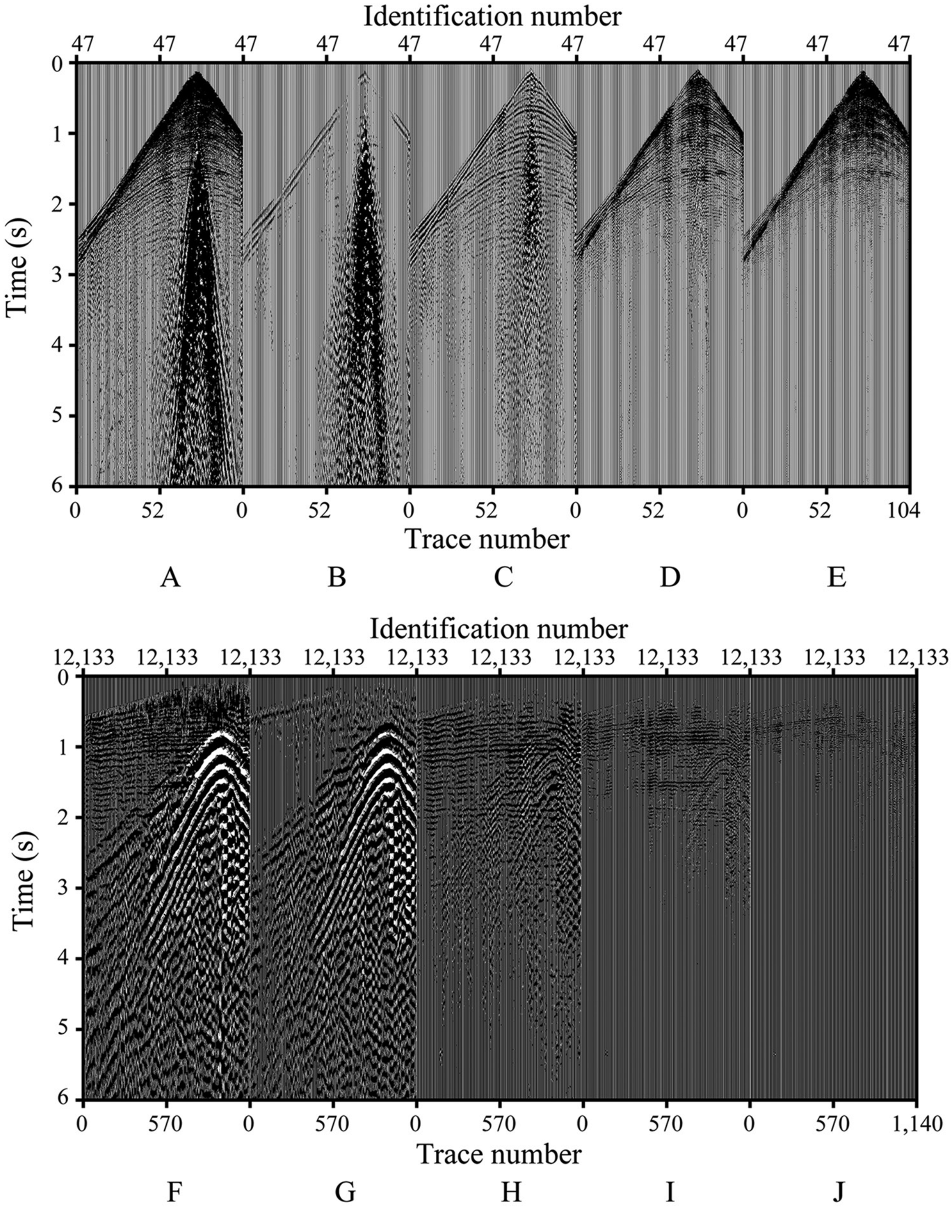

Figure 9. Frequency-band scanning comparison of shot gathers with (A-E) nodal acquisition and (F-J) 30° HWC acquisition. (A and F) Raw shot gather; (B-G) 5–10Hz; (C–H) 10–20Hz; (D–I) 20–40Hz; (E-J) 0–60Hz.

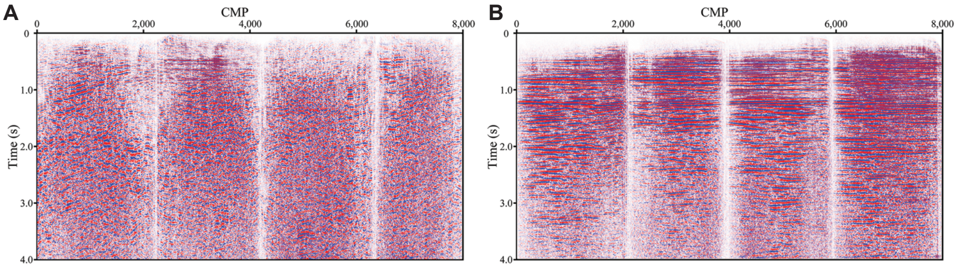

Figure 10. Performance comparison of seismic acquisition methods: (A) 60° HWC and (B) 30° HWC.
Abbreviations: CMP: Common midpoint; HWC: Helically wound cable.

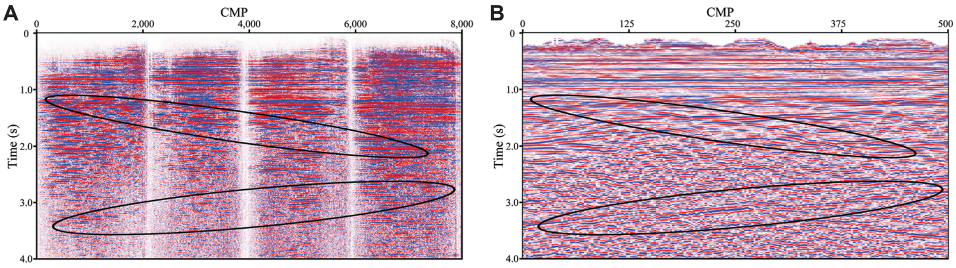

Figure 11. Performance comparison of seismic acquisition methods: (A) the HWC acquisition profile and (B) the seismic profile. Abbreviations: CMP: Common midpoint; HWC: Helically wound cable.

low/uneven fold and limited offsets. Overall, the HWC demonstrated a clear capability to acquire surface seismic reflection data, showing significant practical potential.

6. Discussion

While this study demonstrates significant promise, it also highlights areas for further development. The current limitations in fold coverage and maximum offset inherent in our test setup impacted the mid-to-deep section quality. Future work should focus on deploying longer HWC arrays or multiple parallel cables to achieve sufficient fold and offset distribution for robust imaging of deeper targets. Quantitative comparisons of signal fidelity, resolution, and noise characteristics between HWC and geophones with matched fold conditions are needed. Furthermore, developing specialized processing flows tailored to HWC DAS data, particularly addressing its unique noise fields, amplitude behavior, and directional sensitivity, will be crucial for maximizing its potential. From an economic viewpoint, considering cable manufacturing costs, deployment efficiency, and operational scalability compared to large nodal arrays requires a detailed assessment as the technology advances. Nevertheless, this successful field trial marks a substantial step forward. Distributed HWC technology, with its unique combination of high-density sampling, operational flexibility in challenging environments, and proven ability to capture surface seismic reflections, offers a compelling pathway for next-generation seismic acquisition systems aimed at higher resolution, lower cost, and reduced environmental footprint.

7. Conclusion

This study proposed and field-tested an HWC for DAS in land seismic exploration. Combining theoretical analysis with field experimentation, we optimized the HWC design and evaluated its performance, yielding the following key conclusions. To overcome the single-component (axial) sensitivity limitation of conventional straight-fiber DAS, we developed the HWC concept. Helically winding the sensing fiber enhances sensitivity to both compressional (P-) and shear (S-) waves, significantly expanding DAS applicability to surface seismic exploration. Field data acquired with optimally wound (30°) HWC exhibited clear seismic signals, continuous wave groups, and high resolution (particularly shallow), demonstrating its viability for practical surface seismic acquisition. Deploying HWC cables in challenging terrains, such as water networks and tidal flats, through our innovative underwater scheme effectively resolved coupling issues. This approach leverages the inherent advantages of high spatial sampling density offered by DAS and eliminates the problem of missing traces encountered when deploying conventional geophones in inaccessible areas.

Acknowledgments

None.

Funding

This study was financially supported by the Sinopec Project “Development and Pilot Test of Distributed Spiral Optical Fiber Sensing System” (Grant No. SGC-2024-21).

Conflict of interest

The authors declare they have no competing interests.

Author contributions

Conceptualization: Jingyuan Wang, Bin Liu
Formal analysis: Jing Zhu, Weiwei Duan
Investigation: Bin Liu,Jing Zhu
Methodology: Jingyuan Wang, Weiwei Duan
Visualization: Jing Zhu, Weiwei Duan
Writing–original draft: Jingyuan Wang, Bin Liu
Writing–review & editing: All authors

Availability of data

All data analyzed have been presented in the paper.

References

1. Wang C, Shang Y, Zhao WA, *et al*. Investigation and comparison of Φ-OTDR and OTDR-interferometry via

phase demodulation. *IEEE Sens J*. 2018;18(4):1501-1505.

doi: 10.1109/JSEN.2017.2785358

2. Shi Y, Feng H, Zeng ZM. Distributed fiber sensing system with wide frequency response and accurate location. *Opt Lasers Eng*. 2016;77:219-224.

   doi: 10.1016/j.optlaseng.2015.08.010

3. Du QC, Wang C, Shang Y, *et al*. Study on distributed fiber seismic wave detection system and its layout optimization. *Shandong Sci*. 2017;30(5):55-61.

   doi: 10.3976/j.issn.1002-4026.2017.05.010

4. Lin TF, Dou LR, Gan LD. Development history and prospect of seismic exploration technology. *World Pet Ind*. 2023;30(1):57-69.

   doi: 10.20114/j.issn.1006-0030.2023.01.012

5. Song ZH, Zeng XF, Xu SH, Hu JP, Sun TW, Wang BS. Distributed acoustic sensing for imaging shallow structure I: Active source survey. *Chin J Geophys*. 2020;63(2):532-540.

   doi: 10.6038/cjg2020N0184

6. Sui WB, Liu RQ, Cui K. Application and research progress of distributed optical fiber acoustic sensing monitoring for hydraulic fracturing. *Sci Sin Technol*. 2020;51(4):1622-1629.

   doi: 10.1360/SST-2020-0195

7. Li YP, Li F, Li JG, Jin QH, Liu CW, Wu JJ. Application of distributed acoustic sensing in borehole seismic exploration. *Geophys Prospect Petroleum*. 2020;59(2):242-249.

   doi: 10.3969/j.issn.1000-1441.2020.02.007

8. Mestayer J, Karam S, Cox B, *et al*. Distributed Acoustic Sensing for Geophysical Monitoring. In: *Expanded Abstracts of 74th EAGE Conferenceand Exhibition*; 2012. p. 4253-4557.

   doi: 10.3997/2214-4609.20148800

9. Zhou R. Development status and prospect of optical fiber seismic wave detection technology. *Sci Technol Innov*. 2020;(3):15-16.

10. Cao DP, Lv JJ, Sun SR, Ma GQ, Yin JJ. Three-componet signal acquisition mechanism of distributed acoustic sensing based on helically winding fiber-optic. *Geophys Prospect Pet*. 2022;61(1):60-69.

    doi: 10.3969/j.issn.1000-1441.2022.01.006

11. Hornman JC. Field trial of seismic recording using distributed acoustic sensing with broadside sensitive fibre-optic cables. *Geophys Prospect*. 2017;65(1):35-46.

    doi: 10.1111/1365-2478.12358

12. Hornman K, Kuvshinov B, Zwartjes P, Franzen A. Field Trial of a Broadside-Sensitive Distributed Acoustic Sensing Cable for Surface Seismic. In: *Expanded Abstracts of 75th EAGE Conference and Exhibition*.

13. Wuestefeld A, Wilkd M. How to twist and turn a fiber: Performance modeling for optimal DAS acquisitions. *Leading Edge*. 2019;38(3):226-231.

    doi: 10.1190/tle38030226.1

14. Innanen KA. Parameterization of a Helical DAS Fibre Wound about an Arbitrarily Curved Cable Axis. In: *79th EAGE Conference and Exhibition*. Vol. 1; 2017. p. 1-5.

    doi: 10.3997/2214-4609.201701202

15. Innanen KA. Determination of Seismic-Tensor Strain from Helical Winding Cable-Distributed Acoustic Sensing Cable with Arbitrary and Nested-Helix Winds. In: *Expanded Abstract of 87th Annual Internat SEG MTG*; 2017. p. 926-930.

16. Eaid MV, Li JX, Innanen KA. Modeling the Response of Shaped DAS Fibres to Microseismic Moment Tensor Sources. In: *Expanded Abstracts of 88th Annual Internat SEG MTG*; 2018. p. 4698-4702.

    doi: 10.1190/segam2018-2998378.1

17. Eaid MV, Keating SD, Innanen KA. Multi-parameter seismic elastic full waveform in version with combined geophone and shaped fiberoptic cable data. *Geophysics*. 2020;85(6):1-66.

    doi: 10.1190/geo-2020-0170.1

18. Egorov A, Correa J, Bona A, *et al*. Elastic full-waveform inversion of vertical seismic profile data acquired with distributed acoustic sensors. *Geophysics*. 2018;83(3):273-281.

    doi: 10.1190/geo2017-0718.1

19. He XG, Pan Y, You HJ, *et al*. Fibre optic seismic sensor for down-well monitoring in the oil industry. *Measurement*. 2018;123(1):145-149.

    doi: 10.1016/j.measurement.2018.03.047

20. He XG, Zhang M, Gu LJ, Xie SR, Liu F, Lu HL. Performance improvement of dual-pulse heterodyne distributed acoustic sensor for sound detection. *Sensors*. 2020;203(4):999.

    doi: 10.3390/s20040999

21. Ainslie MA, McColm JG. A simplified formula for viscous and chemical absorption in sea water. *J Acoust Soc Am*. 1998;103(3), 1441-1445.

    doi: 10.1121/1.421258

ACCSCIENCE PUBLISHING

Journal of Seismic Exploration

ARTICLE

Quantifying the effects of micro-cracks on velocity anisotropy in lacustrine shales with variable sedimentary structures

Wenhui Tan[1,2], **Weihua Liu**[1,2], **Yang Wang**[1,2*], **and Hui Shen**[1,2]

[1]SINOPEC Geophysical Research Institute Co., Ltd., Nanjing, Jiangsu, China

[2]SINOPEC Key Laboratory of Geophysics, Nanjing, Jiangsu, China

(This article belongs to the *Special Issue: Seismic Wave Propagation Theories and Reservoir Characterization Technologies for Complex Anisotropic Media*)

Abstract

Understanding the relationship between micro-cracks and elastic anisotropy is crucial for characterizing subsurface flow pathways, optimizing hydraulic fracturing, and enhancing seismic interpretation in unconventional shale reservoirs. Although clay content and total organic carbon (TOC) are recognized primary controls on anisotropy, the specific influence of sedimentary structures on micro-crack parameters (such as crack porosity, crack density, and aspect ratio) and their contribution to anisotropic behavior have not been fully quantified, particularly in lacustrine shales with varied sedimentary architectures. In this study, 17 shale samples were categorized into three sedimentary structural types: laminated, bedded, and massive, based on their microstructure characteristics. Ultrasonic velocity measurements were performed on 17 paired shale plugs under confining pressures to quantify the relationship between micro-crack parameters and elastic anisotropy. Experimental results reveal a clear difference in stress sensitivity of bedding-normal velocities: Laminated shales > bedded shales > massive shales, which are attributed to varying degrees of micro-crack alignment and density. Laminated shales exhibit the strongest anisotropic properties, followed by bedded shales, while massive shales show weak anisotropy. Velocity predictions from the Mori-Tanaka effective medium model are in good agreement with the measurements, validating its applicability for shales with diverse structures. Micro-crack analysis indicates a positive correlation between crack density/porosity and anisotropy magnitude. Notably, laminated shales are characterized by the highest crack porosity (0.012–0.015%), high clay content (average 40%), and moderate TOC, indicating a combined effect of composition and microstructure on anisotropy. This study highlights that sedimentary structure plays a key role in controlling micro-crack development and related anisotropy in lacustrine shales, with laminated shales exhibiting the most significant combined effect, thus improving the accuracy of minimum-horizontal-stress prediction and hydraulic-fracture design.

Keywords: Lacustrine shale; Micro-cracks; Thomsen anisotropic parameters; Ultrasonic experiment; Mori-Tanaka model

***Corresponding author:**
Yang Wang
(wangyang.swty@sinopec.com)

Citation: Tan W, Liu W, Wang Y, Shen H. Quantifying the effects of micro-cracks on velocity anisotropy in lacustrine shales with variable sedimentary structures. *J Seismic Explor*. 2025;34(4):28-41. doi: 10.36922/JSE025340060

Received: August 18, 2025

Revised: September 12, 2025

Accepted: September 17, 2025

1. Introduction

In recent years, lacustrine shale oil and gas reservoirs in China have emerged as a critical focus in the development of unconventional hydrocarbon resources. Shale is a self-generating and self-storing reservoir. Its unique properties make it a strategic target for boosting China's oil and gas reserves.[1-3] In the exploration and development of shale oil and gas, elastic anisotropy is the key geological attribute to determine the physical properties of reservoirs. Studies have shown that shale reservoirs generally exhibit significant anisotropic characteristics.[4,5] This anisotropy controls wave propagation, fluid flow, and mechanical response. Consequently, it affects seismic imaging, log interpretation, reservoir characterization, and fracturing design. This characteristic has a direct impact on seismic imaging accuracy, logging interpretation reliability, reservoir physical characterization, and hydraulic fracturing scheme design by controlling seismic wave propagation law, seepage capacity, and mechanical response.[6-9] Accurately characterizing the anisotropic characteristics of shale can not only improve the prediction accuracy of seismic data on reservoir boundary and quality, but also effectively reduce engineering risks and costs by optimizing exploration and development strategies. However, due to the influence of geological deposition and diagenesis, the coupling of horizontal bedding, organic-inorganic mineral facies, and pore space in organic-rich shale leads to the extremely complex formation mechanism of elastic anisotropy, which brings severe challenges to the establishment of a universal anisotropy model. At the micro-scale, micro-cracks are the key factor controlling the anisotropy of shale, and there is still a significant uncertainties remain in quantifying the influence mechanism of micro-cracks on velocity anisotropy. In addition, the differences in experimental conditions (such as stress state and fluid properties) and the diversity of theoretical models (such as equivalent medium theory and discrete fracture network simulation) in the current research lead to the lack of comparability between different results, and a unified scientific understanding has not yet been established.[10-12]

As a typical fine-grained sedimentary rock, shale exhibits significant anisotropy shaped by micro-cracks, the preferred orientations of platy clay particles, and lenticular kerogen.[4,5] Researchers worldwide have conducted extensive experimental studies on shale samples to identify the controlling factors of intrinsic anisotropy. Vernik and Liu[13] performed ultrasonic measurements on the Bakken shale (USA). They observed maximum elastic anisotropy at total organic carbon (TOC) values of 15–20%. This reveals the critical role of organic matter content in shale elasticity; bedding-parallel organic matter may significantly influence medium anisotropy by altering mineral grain contacts or micro-crack alignment. Notably, there are obvious geological differences in the influence of organic matter on anisotropy. The anisotropy of Wufeng-Longmaxi Formation shale in China has no obvious correlation with organic matter content, while the organic matter content of Bakken shale in the United States and Bazhenov shale in Russia is the key controlling factor of anisotropy. This difference is attributed to the different maturity, occurrence form, and distribution characteristics of organic matter. Laminated clay minerals represent another key factor. Comparative studies by Sone and Zoback[14] on North American shales (Barnett, Haynesville, Eagle Ford) showed a significant positive correlation between clay content and anisotropy intensity, consistent with theories with transversely isotropic proposed by Hornby *et al.*[15] and Sayers[16] that laminated clay induces the formation of transversely isotropic shale. Further studies indicate that preferred orientation of clay platelets directly affects shale elastic parameters.[17-24] Liu *et al.*[12] measured ultrasonic pulses in Longmaxi Shale and found a 0.82 correlation between clay content and velocity anisotropy parameters: The higher the degree of clay orientation, the more significant the anisotropy characteristics. Liu *et al.*[25] studied Jurassic lacustrine shale from the Sichuan Basin and proposed an "effective parameter" (total porosity + clay content + kerogen volume) to distinguish elastic and anisotropic characteristics among four lithofacies, based on ultrasonic velocity measurements under varying confining pressures.

In recent years, beyond studies on the intrinsic anisotropy of shale under high-pressure conditions, the fracture response information embedded in velocity variations with confining pressure has become a research focus for scholars. Vernik[26] first quantified the dynamic relationship between micro-crack-induced anisotropy and mineral-oriented intrinsic anisotropy through confining pressure-velocity experiments on mature source rock shales: as confining pressure increases, progressive micro-crack closure leads to a decrease of anisotropy, while intrinsic anisotropy from preferred orientation clay/kerogen tends to stabilize. This achievement provides key mechanical insights into the anisotropy evolution of stress-sensitive reservoirs. Ciz and Shapiro[27] established a porosity-deformation approach for transversely isotropic shales and, combined with ultrasonic measurement data from North Sea shale samples, inverted crack contribution through the confining pressure response of elastic moduli, verifying the dominant role of micro-crack closure in anisotropy.[11,28-31] These previous studies revealed the coupled relationship between cracks, confining pressure, and anisotropy through experimental observations, theoretical modeling, and numerical simulations. Nevertheless, the current rock physics approach to inverting the response mechanism of cracks and reservoir parameters still faces multiple challenges. At present, the research on anisotropy induced by stress-induced cracks mainly focuses on marine shale. However, due to the complexity of the microstructure of la cuisine shale, the effective medium model is limited in its application. In addition, there are significant differences in the anisotropy values generated by stress-induced cracks in different lithofacies, underscoring the urgent need for more in-depth investigations in this domain.

In this study, we focus on lacustrine shales from the Songliao Basin in Northeast China. Based on their microstructural characteristics, these shales are classified into three lithofacies types. Using ultrasonic velocity measurement experiments and inversion based on the Mori-Tanaka (M-T) effective medium theory, we systematically investigate the anisotropic responses of stress-induced micro-cracks in lacustrine shales and elucidate the underlying mechanism by which micro-cracks contribute to shale anisotropy. The results offer critical experimental evidence and theoretical basis for predicting micro-crack development in lacustrine shale reservoirs via seismic data, as well as optimizing reservoir evaluation and development strategies.

2. Experimental methodology

2.1. Basic characteristics of the sample

Seventeen full-diameter shale samples used in this study were collected from a Cretaceous lacustrine reservoir located in Northeastern China. The mud shale in such a formation is frequently characterized by its large thickness, high TOC, moderate thermal maturity, and overpressure.[32-34] A total of 17 cylindrical plugs, each with a diameter of 25 mm and a length of approximately 50 mm, were drilled from the full-diameter samples along the bedding direction. The cylinders then underwent a drying process with a temperature of 80°C for over 48 h, until the sample weight does not vary. Subsequently, the porosity of each cylindrical shale sample is measured using the helium gas method.

TOC of each sample is measured by the Rock-Eval Pyrolysis tests. The results revealed that TOC of 17 samples ranges from 0.1 to 3.2%. The mineral composition of each shale sample was determined through the powder X-ray diffraction analysis (Figure 1). The collected shales are mainly composed of clay, quartz + feldspar + pyrite (QFP), and carbonate minerals. From the core photos and the thin section images in Table 1, the fine-grained rocks can be described as either laminated, bedded, or massive,[34,35] according to the thickness of beddings. The laminated rocks, with bedding thickness <10 mm, display obvious grain-size changes. The silt and clay laminae terminate sharply at their margins, as shown in Table 1. The bedding thickness of bedded rocks is normally >1 cm with silt or clay beddings alternately stacking together, as shown in Table 1. The massive samples, with bedding thickness larger than 50 cm, are distributed either near the 100%-carbonate-end or the 100%-QFP-end in the ternary diagram (Figure 1).

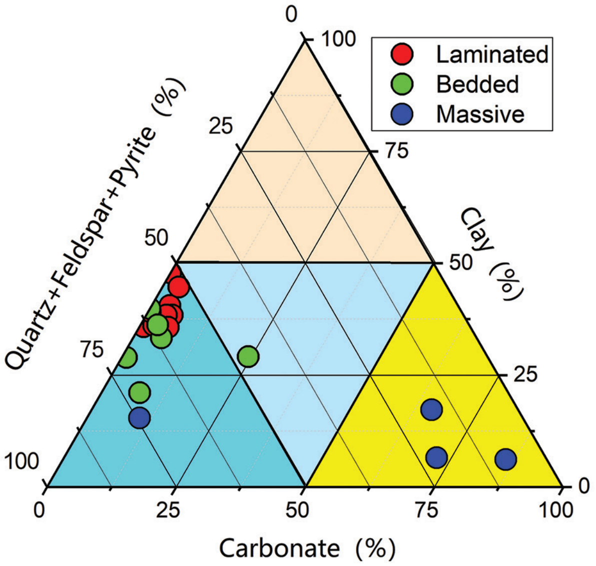

Figure 1. Ternary diagram for 17 shale samples with different sedimentary structures. The red circle represents laminated, the green circle represents bedded, and the blue circle represents massive.

From Table 1, the development of micro-cracks varies with the sedimentary structures. In general, the micro-cracks are most developed in laminated shales, followed by bedded shales. Nearly no micro-cracks could be seen in the massive shales from the amplified thin section image. The development of micro-cracks in laminated shales could be attributed to two main reasons. From one aspect, in the weak plane between silt and clay laminae, it is easy to develop bedding cracks or diagenetic contraction cracks along bedding directions. From the other aspect, the stripped kerogen in laminated shales is at the peak of oil generation (R_o ~ 1.3%). A mass of hydrocarbon would be generated and migrated along the weak plane between beddings, leaving hydrocarbon-expulsion micro-cracks behind.[36] For bedded shales, the inter-bedded micro-cracks (at the silt-clay interfaces) dominate, while less hydrocarbon-expulsion micro-cracks develop. For massive shale, due to its homogeneous mineral composition and lack of laminae weak planes, only sporadically isolated contraction cracks develop.[37,38]

2.2. Measurement of anisotropic ultrasonic velocity

We performed ultrasonic velocity measurements on 17 horizontal shale samples by using the pulse

Table 1. Cores and thin sections of laminated shale, bedded shale, and massive shale

Samples	Cores	Thin sections	Descriptions
Laminated shale		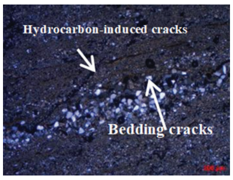	• Alternating deposition of silt and clay laminae, with thickness <10 mm. • Bedding cracks, diagenetic contraction cracks, and hydrocarbon-expulsion cracks develop along bedding directions.
Bedded shale	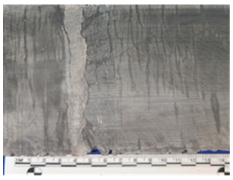	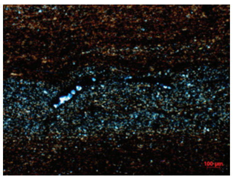	• Bedding thickness is >1 cm with silt or clay beddings alternately stacking together. • The inter-bedded micro-cracks (at the silt-clay interfaces) dominate.
Massive shale	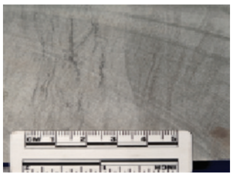	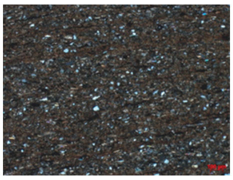	• The mineral composition is uniform, lacking laminae or bedding interfaces. • Micro-cracks are less developed.

transmission method.[39] To gain velocities in different directions from one single horizontal plug, three pairs of P-wave transducers (0°, 45°, and 90° with respect to the symmetry axis) and two pairs of S-wave transducers (propagating along beddings, polarizing in both bedding-normal and bedding-parallel direction) were mounted in the sample, as shown in Figure 2. The central frequencies for P- and S-wave transducers were 1 MHz and 0.5 MHz, respectively. The horizontal shale was wrapped with the rubber sleeve and put into a confining vessel filled with silicon oil. The velocities were measured at varied confining pressures ranging from 5 MPa to 35 MPa. Five velocities were all measured in one single horizontal shale plug: $V_p(0°)$, $V_p(90°)$, $V_p(45°)$, $V_{sh}(90°)$, and $V_{sv}(90°)$, allowing for a thorough analysis of the full stiffness tensor and anisotropy of transversely isotropic (TI) shales. It is noteworthy that the relative systematic error in velocity measurements is approximately ±1% for P-waves and ±2% for S-waves.

Unconventional shales are often depicted to be a transversely isotropic medium with a vertical rotational symmetry axis (VTI). According to the anisotropic Hooke's law, a VTI medium can be characterized by five independent stiffnesses (C_{11}, C_{33}, C_{44}, C_{66}, C_{13}). With five direction-dependent velocities and the measured bulk density (ρ), five independent stiffnesses could be derived as follows:

$$C_{11} = \rho V_p^2(90°) \qquad \text{(I)}$$

$$C_{33} = \rho V_p^2(0°) \qquad \text{(II)}$$

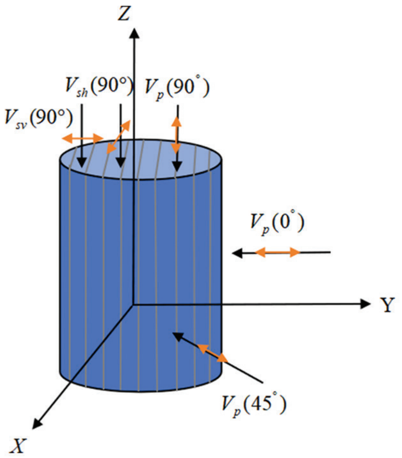

Figure 2. Schematic diagram of the direction-dependent velocity measurement with one-single-horizontal shale sample[39]

$$C_{44} = \rho V_{sv}^2(90°) \qquad \text{(III)}$$

$$C_{12} = C_{11} - 2\rho V_{sh}^2(90°) \qquad \text{(IV)}$$

$$C_{13} = -C_{44} + \sqrt{(C_{11} + C_{44} - 2\rho V_p^2(45°))(C_{33} + C_{44} - 2\rho V_p^2(45°))} \qquad \text{(V)}$$

Subsequently, P- and S-wave velocity anisotropy could be expressed with Thomsen's parameters, ε and γ, respectively[40]:

$$\varepsilon = \frac{C_{11} - C_{33}}{2C_{33}} \qquad \text{(VI)}$$

$$\gamma = \frac{C_{66}\text{-}C_{44}}{2C_{44}} \tag{VII}$$

3. Pressure-dependent properties

3.1. Experimental results

Figure 3 displays the directional velocities ($V_p(0°)$, $V_p(90°)$, $V_{sh}(90°)$, and $V_{sv}(90°)$) as a function of the applied confining pressure for three typical samples with laminated, bedded, and massive structure. Overall, despite the rock structure, all four velocities increase with the increasing pressure. Both P- and S-wave velocities in the bedding-normal direction ($V_p(90°)$ and $V_{sv}(90°)$) satisfy the following relationship: laminated < bedded < massive.

The pressure-dependent velocities in Figure 3, to some extent, reveal the effects of bedding-related micro-cracks. In general, the bedding-normal velocities show strong non-linear behavior at low pressures and subsequently get flattened at high pressures, while the bedding-parallel velocities are almost linear over the entire range of confining pressure.[26] By assuming that the flattened bedding-normal velocities indicate all micro-cracks are closed at the highest pressure,[41] we define a stress sensitivity parameter, $V/V(35\text{MPa})$, to qualitatively characterize the effects of micro-cracks for three types of rocks. It should be noted that V denotes $V_p(0°)$ or $V_{sv}(90°)$ at the varied confining pressures (5 MPa, 10 MPa, 15 MPa, 25 MPa, and 35 MPa), while $V(35\text{MPa})$ suggests $V_p(0°)$ or $V_{sv}(90°)$ at the confining pressure of 35 MPa. Figure 4 shows the plot of the stress sensitivity parameter against the applied confining pressure for $V_p(0°)$ and $V_{sv}(90°)$. Both stress sensitivity parameters vary non-linearly up to 1 at the highest confining pressure, revealing a process of micro-cracks closure. The stress sensitivity of bedding-normal

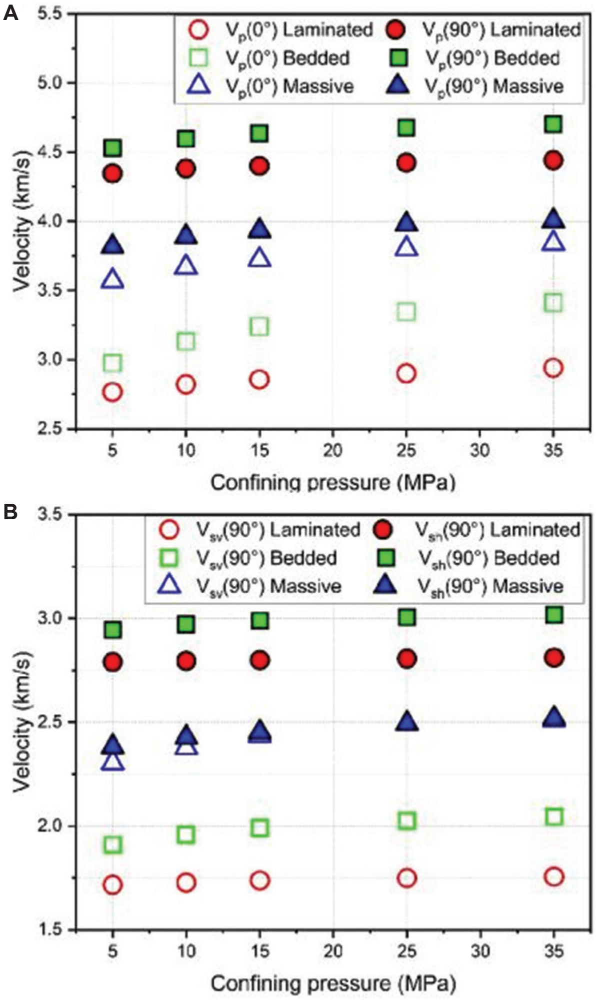

Figure 3. P-wave (A) and S-wave velocities (B) in both bedding-normal and bedding-parallel directions as a function of the applied confining pressure for three typical samples with laminated, bedded, and massive structure

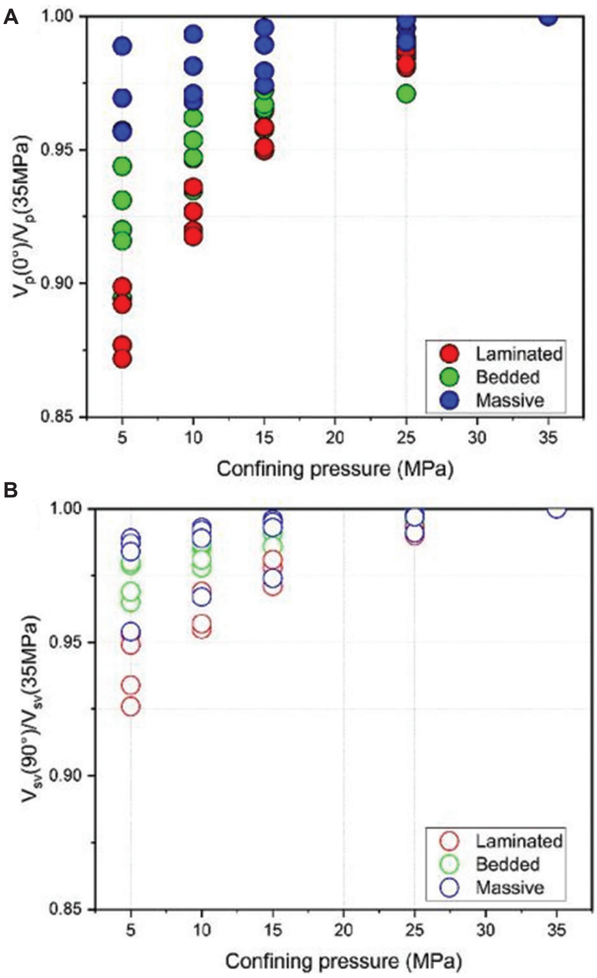

Figure 4. Stress sensitivity parameter as a function of the applied confining pressure for $V_p(0°)$ (A) and $V_{sv}(90°)$ (B)

velocities relies on the rock structures, satisfying the following relationship: laminated > bedded > massive.

As shown in Figure 3, the bedding-parallel velocities are generally greater than the bedding-normal ones, especially for laminated and bedded shales, displaying obvious velocity anisotropy. The anisotropy degree of P- and S-wave velocities is expressed with ε and γ, calculated based on **Equations VI** and **VII**. Accordingly, Figure 5 shows plots of ε and γ against the applied confining pressure for three typical samples. Figure 5A shows both ε and γ for laminated and bedded samples decrease non-linearly as the confining pressure increases from 5 MPa to 25 MPa, and get relatively flattened at the subsequently confining pressure. However, ε and γ for the massive shale are much lower, combined with relatively constant values over the entire confining pressure range. Figure 5B presents a crossplot of Thomsen's anisotropy parameters ε and γ for three structural types. Overall, ε and γ show a good positive linear correlation. The laminated samples exhibit stronger anisotropy, generally occupying higher values of both ε and γ =, while the massive samples cluster at lower values, and the bedded samples show an intermediate distribution.

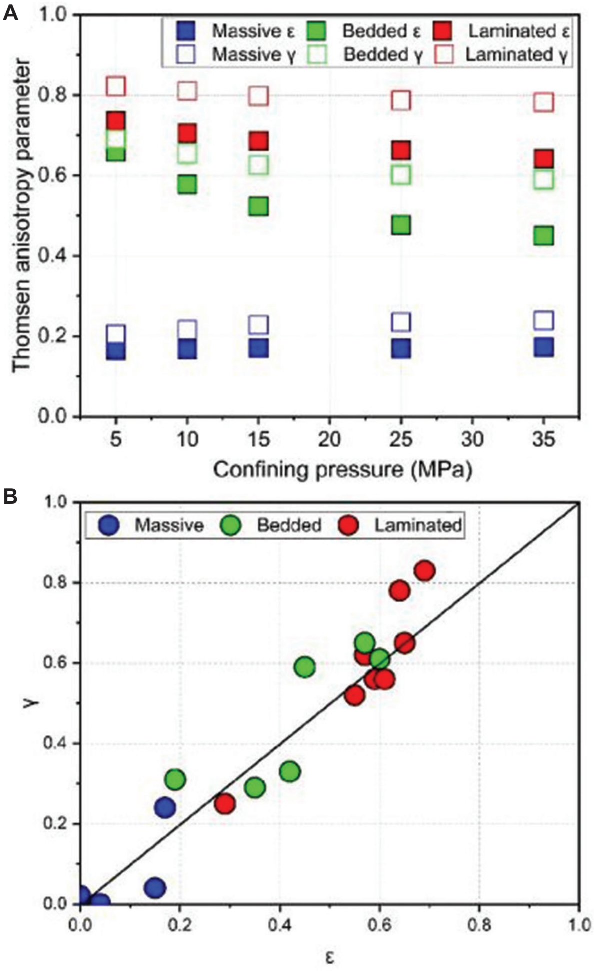

Figure 5. Anisotropic characteristics of shale with three typical samples. (A) ε and γ as a function of the applied confining pressure for three typical samples with laminated, bedded, and massive structure. (B) A plot of anisotropy parameter γ versus anisotropy parameter ε for three typical samples with laminated, bedded, and massive structure.

3.2. Mechanism of shale anisotropy

Shale velocity anisotropy is frequently attributed to the combined effects of many intrinsic and extrinsic factors.[8] Intrinsic velocity anisotropy primarily stems from three key mechanisms: The alternation of lithologies or laminae, the preferred orientation of clay platelets or kerogen, and the bedding-parallel micro-cracks.[13,42,43] Figure 5B shows a plot of γ versus ε at the highest confining pressure (35 MPa), revealing the effects of rock texture (laminated, bedded, massive) and mineral composition on intrinsic anisotropy. Based on Figure 5B, the anisotropy degree of 17 lacustrine shales satisfies the following relationship: laminated > bedded > massive. As shown in Figure 1, the total clay content ranges from 5% to 45%, with an average value of 40% for laminated shales and 32% for bedded shales. For Cretaceous shale reservoirs, clay minerals have thoroughly experienced the transition from smectite to illite. Clay minerals are dominated by illite and illite-smectite mixed layers with obvious preferred orientation along beddings after sedimentary compaction, resulting in relatively strong anisotropy. However, for massive shales, the anisotropy degree is relatively low due to the low clay content and lack of bedding texture. Besides, the kerogen tends to align subparallel to beddings with a strip-like pattern for laminated and bedded shales, as shown in Table 1, further amplifying the velocity contrast in bedding-normal and bedding-parallel directions.

In addition, the pressure-dependent properties of bedding-normal velocities (Figure 4) and anisotropy parameters (Figure 5A) indicate that micro-cracks might be a non-negligible factor in evaluating shale anisotropy. As discussed in Table 1, micro-cracks mainly originate from two sources: Bedding-parallel micro-cracks and hydrocarbon-expulsion-induced micro-cracks. These cracks are closed at *in situ* conditions. In the process of coring, these micro-cracks tend to open due to the stress relief. By applying confining pressure to the approximate *in situ* stress condition in the laboratory, these opened cracks close gradually, revealing the pressure-dependence of bedding-normal velocities. Conversely, the pressure dependence of velocities can, to some extent, be used to quantitatively evaluate the contribution of micro-cracks to shale anisotropy. In the next section, we will focus on the quantitative inversion and evaluation of micro-crack effects on anisotropy.

4. Effects of micro-cracks on shale anisotropy

4.1. M-T theory

To quantitatively evaluate the effects of micro-cracks on shale anisotropy, the key is to accurately invert micro-crack parameters from the pressure-dependent bedding-normal velocities (Figure 3). We employed the M-T theory,[44] which has been widely recognized for its capability to capture the intricate interactions between the micro-structural features of materials and their macroscopic mechanical properties.

Mori and Tanaka[44] established the relationship between the elastic modulus of rocks and their microscopic pore structure. The stiff moduli of rocks are expressed as:

$$K_{stiff} = \frac{K_0}{(1 + {\phi_{stiff}}/{1-\phi_{stiff}} \, P)} \tag{VIII}$$

$$G_{stiff} = \frac{G_0}{(1 + {\phi_{stiff}}/{1-\phi_{stiff}} \, Q)} \tag{IX}$$

Where K_{stiff} and G_{stiff} are the effective bulk and shear modulus of rocks, when only stiff inter-particle pores exist. K_0 and G_0 are bulk and shear moduli of mineral grains, respectively. Φ_{stiff} indicates the porosity contributed from inter-particle pores. P and Q represent shape factors of stiff pores, which are related to the aspect ratio α of ellipsoidal pores and Poisson's ratio v_s of mineral grains,[41,45] as shown in **Equations X-XII**. By assuming that low-aspect-ratio micro-cracks (soft pores) are completely closed at extreme high confining pressure, K_{stiff} and G_{stiff} could be calculated through $V_p(0°)$ and $V_{sv}(90°)$ measured at confining pressure of 35 MPa, as shown in Figure 3. Based on **Equation VIII**, α can be obtained through the least squares regression of K_{stiff}.

$$P = \frac{1\text{-}\upsilon_s}{6(1-2\upsilon_s)} \cdot \frac{\begin{gathered}4(1+\upsilon_s)+2\alpha^2(7\text{-}2\upsilon_s)\text{-}[3(1+4\upsilon_s)\\+12\alpha^2(2-\upsilon_s)]g\end{gathered}}{2\alpha^2+(1-4\alpha^2)g+(\alpha^2-1)(1+\upsilon_s)g^2}, \tag{X}$$

$$Q = \frac{4(\alpha^2\text{-}1)(1-\upsilon_s)}{15\left\{8(\upsilon_s-1)+2\alpha^2(3-4\upsilon_s)+[(7-8\upsilon_s)-4\alpha^2(1-2\upsilon_s)]g\right\}} \cdot \left\{\begin{gathered}\frac{\begin{gathered}8(1-\upsilon_s)+2\alpha^2(3+4\upsilon_s)+[(8\upsilon_s-1)-4\alpha^2(5+2\upsilon_s)]g\\+6(\alpha^2-1)(1+\upsilon_s)g^2\end{gathered}}{2\alpha^2+(1-4\alpha^2)g+(\alpha^2-1)(1+\upsilon_s)g^2}\\-3\left[\frac{8(\upsilon_s-1)+2\alpha^2(5-4\upsilon_s)+[3(1-2\upsilon_s)+6\alpha^2(\upsilon_s-1)]g}{-2\alpha^2+[(2-\upsilon_s)+\alpha^2(1+\upsilon_s)]g}\right]\end{gathered}\right\}, \tag{XI}$$

Where $\upsilon_s = (3K_0 - 2G_0)/(6K_0 + 2G_0)$, and

$$g = \begin{cases}\dfrac{\alpha}{(1-\alpha^2)^{3/2}}\left(\arccos\alpha - \alpha\sqrt{1-\alpha^2}\right)(\alpha < 1)\\ \dfrac{\alpha}{(1-\alpha^2)^{3/2}}\left(\alpha\sqrt{1-\alpha^2} - \operatorname{arccosh}\alpha\right)(\alpha > 1)\end{cases} \tag{XII}$$

With the rock only including minerals and stiff pores as the background medium, the effective bulk and shear moduli are expressed as follows by considering the effect of soft micro-cracks:

$$K_{eff} = K_{stiff} / \left(1 + \frac{16(1-(\upsilon_{stiff})^2\Gamma}{9(2-\upsilon_{stiff})}\right) \tag{XIII}$$

$$G_{eff} = G_{stiff} / \left(1 + \frac{32(1-\upsilon_{stiff})(5-\upsilon_{stiff})\Gamma}{45(2-\upsilon_{stiff})}\right) \tag{XIV}$$

Where $v_{\text{stiff}} = (3K_{\text{stiff -}} G_{\text{stiff}})/(6K_{\text{stiff}} + 2G_{\text{stiff}})$ is the Poisson's ratio of stiff pores. And Γ is the cumulative micro-crack density.

Given that the pressure-dependent effective moduli are closely related to the micro-crack density, the cumulative micro-crack density $\Gamma_p(\alpha)$ at each pressure can be fitted based on the measured elastic moduli and **Equations XIII** and **XIV** with the least-square regression method. Then, the quantitative relationship between micro-crack density and the effective pressure[46] is expressed as:

$$\Gamma_p(\alpha) = \Gamma^i e^{-p/\check{p}} \tag{XV}$$

Where Γ^i represents the initial micro-crack density at zero effective pressure; and $\check{p}$ is a pressure constant with the same order of magnitude as the effective pressure p, which can be obtained by fitting data with **Equations XIII** and **XIV**.

We can obtain the distribution characteristics of micro-crack porosity and density based on the lab-measured P- and S-wave velocities. The relationship between micro-crack porosity ϕ_c and crack density Γ_p is described by David and Zimmerman[41] as follows:

$$\varphi_c = \frac{4\pi\alpha_p}{3}\Gamma_p \tag{XVI}$$

In addition, the relationship between pore aspect ratio and the effective pressure is expressed as:

$$\alpha_p = {4[1-(\upsilon_{eff})^2]p}/{\pi E_{eff}} \tag{XVII}$$

Where $E_{eff} = 3K_{eff}[1-2\upsilon_{eff}]$ is the effective Young's modulus under high confining pressure; and $\upsilon_{eff} = (3K_{eff} - 2G_{eff})/(6K_{eff} + 2G_{eff})$ is the effective Poisson's ratio under high confining pressure.

4.2. Inversion of micro-crack parameters

According to **Equations VIII-IX**, we first inverted the high-pressure velocities of three shale samples with different structures to estimate the aspect ratios of stiff pores. Since the measured velocities of the samples did not fully reach asymptotic values at 35 MPa, exponential curve fitting of the measured data was performed to estimate the high-pressure velocities. The confining pressure (P)-velocity fitting relationship of sample G1 is V_p = 2628*$P^{0.03116}$, V_s = 1681*$P^{0.01215}$. The confining pressure-velocity fitting relationship of sample G2 is V_P = 2284*$P^{0.08616}$, V_s = 1676*$P^{0.0318}$. The confining pressure-velocity fitting relationship of sample G3 is V_p = 4040*$P^{0.0341}$, V_s = 2338*$P^{0.0356}$. The porosity of the laminated sample G1 is 6.5%, that of the bedded sample G2 is 1.5%, and that of the massive sample G3 is 1.2%. The elastic moduli of grains (K0, G0) were obtained using the Voigt-Reuss-Hill theory for inverting high-pressure data, and the inversion parameters of high-pressure velocities are listed in Table 2. As expected, the inversion crack density/crack porosity is much higher for laminated shale than for bedded and massive shales, as shown in Table 2. The primary causes of crack development in laminated shale are as follows: Silt and clay laminae creates weak planes prone to forming bedding cracks, and oil expulsion during the thermal maturation of organic matter generates micro-cracks arranged parallel to bedding planes as shown in Table 1. Figure 6 shows the effective medium simulation results of P-wave and S-wave velocities for the laminated shale G1, bedded shale G2, and massive shale G3. The P-wave and S-wave velocities inverted based on the M-T theoretical model are in good agreement with the measured data within the error range. Notably, the model's predictions are more accurate for P-waves for than S-waves. These results validate the reliability of the model in predicting shale micro-crack parameters and demonstrate its effectiveness in characterizing the elastic properties of shales with different structure types.

Table 2. Inversion result for the high-pressure velocities

Sample ID	Type	Porosity (%)	K0 (GPa)	G0 (GPa)	α	Crack density	Crack porosity
G1	Laminated shale	6.5	21.5	11	0.09	0.0051	6.38E−05
G2	Bedded shale	1.5	38	13	0.02	0.0042	4.49E−05
G3	Massive shale	1.2	39	21	0.16	0.0021	1.01E−05

Figure 7 illustrates the porosity distribution of soft pores across aspect ratios for shales with distinct structures. The laminated shale (red) features the highest peak crack porosity, occurring at a relatively larger crack aspect ratio. The bedded shale (green) has a lower peak crack porosity than the laminated shale, while the massive shale (blue) shows the lowest peak crack porosity among the three. Across all aspect ratios shown, the laminated shale consistently maintains higher crack porosity than the bedded and massive shales. Figure 8 displays the cumulative crack density distribution of soft pores for the three shale types. The laminated shale has the largest cumulative crack porosity (6.38 × 10^{-3}%), followed by the bedded shale (4.49 × 10^{-3}%), and the massive shale (1.01 × 10^{-3}%) due to its slowest crack development and the lowest cumulative

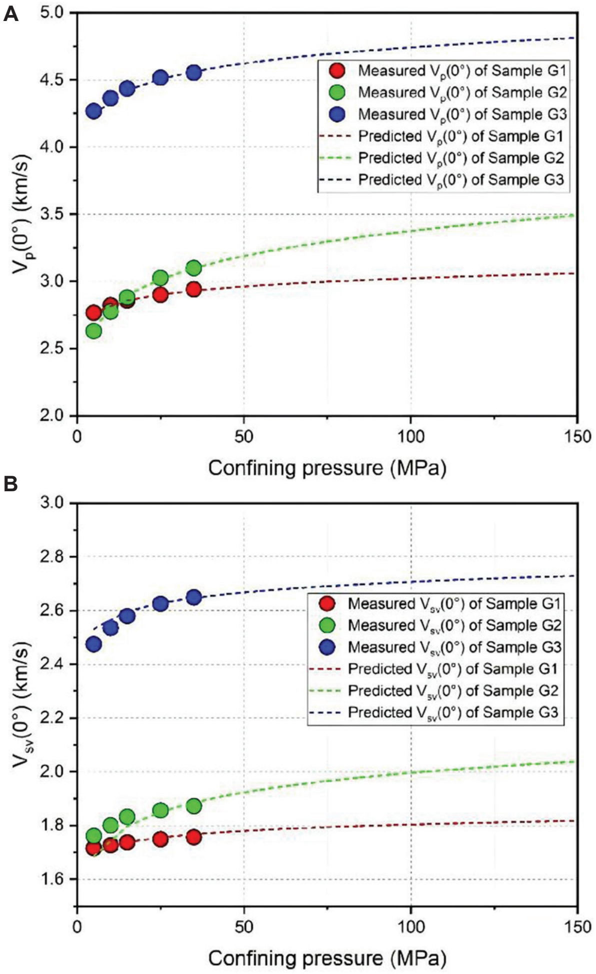

Figure 6. A comparison between the measured pressure-P-wave and S-wave velocities of the samples G1/G2/G3 and those inverted by the Mori-Tanaka model

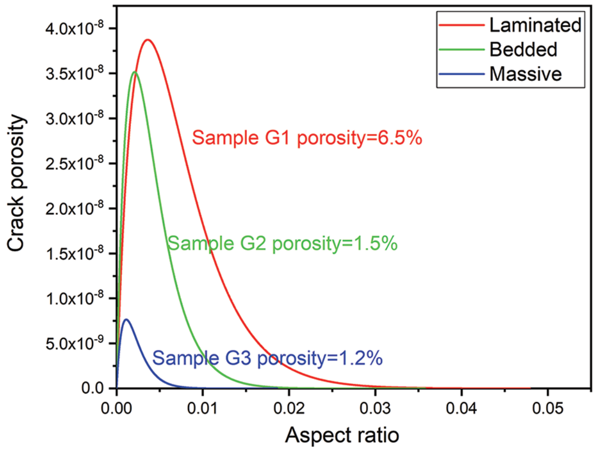

Figure 7. Crack porosity distribution as a function of aspect ratio for different structures

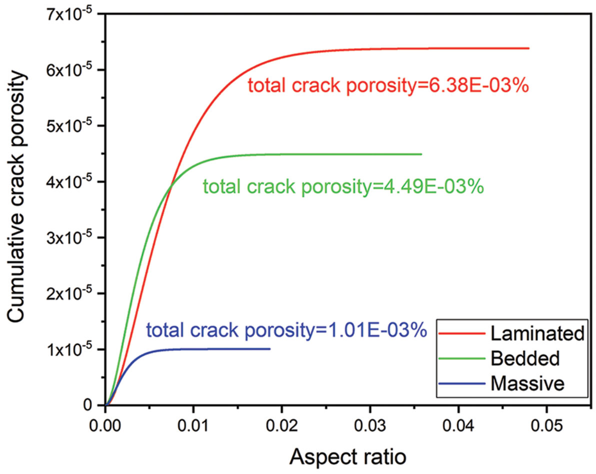

Figure 8. The relationship between cumulative crack porosity and crack aspect ratio for different structures

porosity. Overall, cumulative crack porosity rises initially and stabilizes, with the laminated shale having the highest values, the bedded shale intermediate, and the massive shale the lowest. As shown in Figure 4, the laminated shale exhibits a non-linear stress-sensitive curve (steep velocity-pressure response), while the bedded and massive shales show gentler stress-sensitive curve changes (gradual velocity-pressure response), reflecting their structural and mineralogical differences in pore compressibility.

Figure 9 illustrates the relationship between crack density and crack porosity for three different shale structures. Data points for the laminated shale are widely distributed, with crack porosity reaching approximately 0.015% and corresponding crack density around 0.012. This indicates extensive crack development in laminated shale. In contrast, data for the bedded shale cluster more

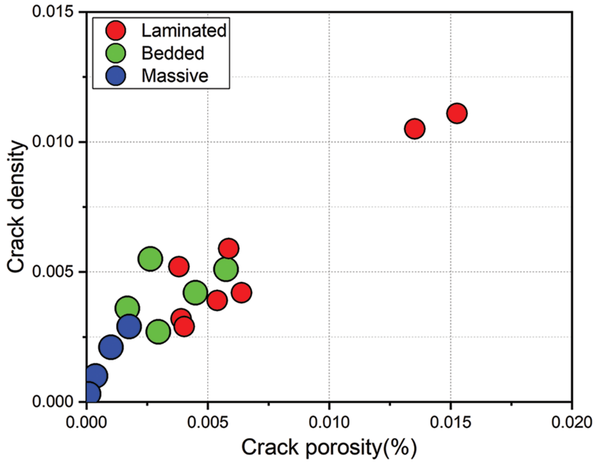

Figure 9. Crossplot of the relationship between crack density and crack porosity

tightly in the medium-to-low range, with crack porosity mostly below 0.006% and crack density typically below 0.006, suggesting moderate crack development. For the massive shale, data points concentrate near the origin, with crack porosity values mostly below 0.003% and crack density consistently below 0.003, indicating the poorest crack network development among the three types. As shown in Figure 1 and Table 1, the high clay mineral content in laminated shale (G1) results in strong clay orientation, forming bedding weak planes. In addition, during hydrocarbon generation and expulsion from organic matter maturation, pressure release along these weak planes generates numerous bedding-parallel cracks, leading to high crack porosity (reflecting interlaminar pores and cracks). Bedded shale (G2) exhibits distinct mud-sand interbedding but with slightly poorer bedding continuity and slightly higher mineral content (e.g., silty quartz) than G1. Bedding weak planes still dominate crack development (primarily bedding-parallel), but some cracks form due to stress concentration at mineral interfaces, resulting in lower crack and total porosity (1.5%) compared to laminated shale. Finally, massive shale (G3) lacks distinct bedding, is dominated by rigid minerals (quartz, feldspar), has low clay content, and exhibits dense intergranular cementation—all of which inhibit crack development, resulting in the lowest crack and total porosity. These results highlight the significant influence of shale structural differences on crack development characteristics, which cannot be overlooked.

4.3. Effects of micro-cracks on shale anisotropy

Analysis of the influencing factors of anisotropy in shale (Figures 10 and 11) reveals two distinct controlling patterns of shale anisotropy: One dominated by micro-crack

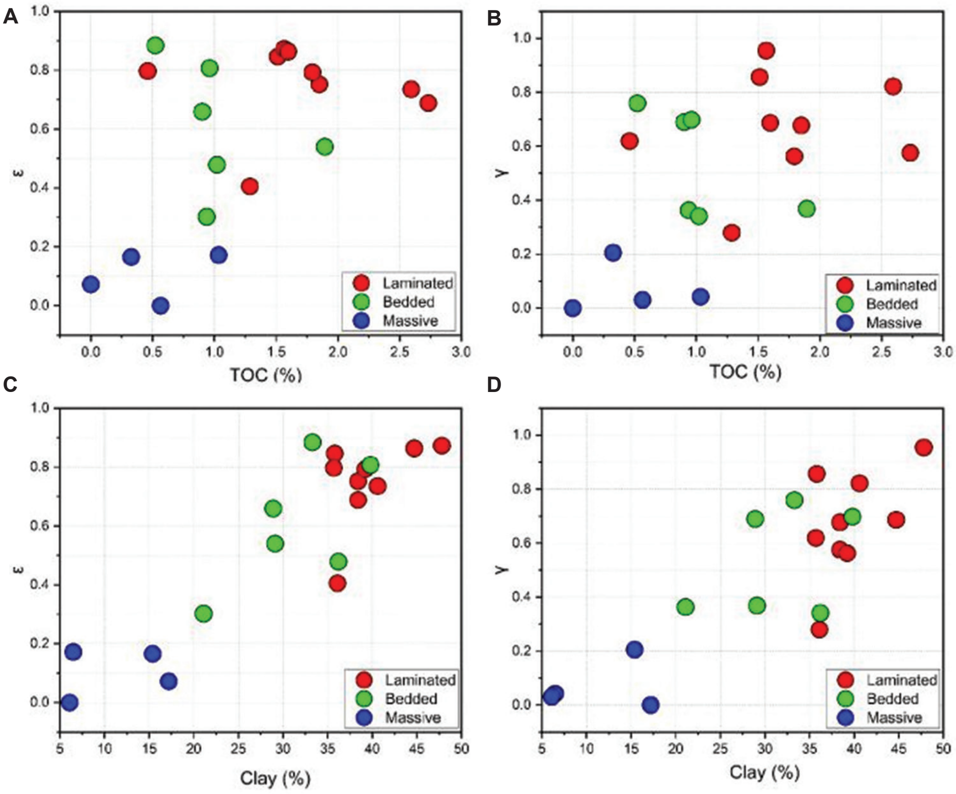

Figure 10. The influence of total organic carbon (TOC)/clay on anisotropic parameters. (A) The relationship between the anisotropy parameter ε and the TOC. (B) The relationship between the anisotropy parameter γ and the TOC. (C) The relationship between the anisotropy parameter ε and the clay. (D) The relationship between the anisotropy parameter γ and the clay.

development and the other by composition. As shown in Figure 10A and B, the Thomsen parameters ε and γ exhibit a clear positive correlation with TOC, particularly in laminated and bedded shales, indicating that organic matter content enhances intrinsic anisotropy. Similarly, Figures 10C and D demonstrate a strong dependence of ε and γ on clay content, highlighting the essential role of clay mineral orientation in forming anisotropic backgrounds. Within this compositional framework, micro-crack porosity further differentiates the anisotropy degree among shale structures (Figure 11). Laminated shale, characterized by high clay content (average 40%) and moderate TOC, exhibits the strongest positive correlation between crack porosity (up to 0.015%) and Thomsen parameters (ε = 0.3–0.8; γ = 0.2–1.0). Results presented in Figure 1 and Table 1 suggest a synergistic effect between clay-induced intrinsic anisotropy and crack-related extrinsic anisotropy. The preferred orientation of clay minerals resulting from smectite-to-illite transformation establishes a foundation of intrinsic anisotropy,[47,48] while hydrocarbon-expulsion-induced micro-cracks, aligned parallel to bedding, further amplify the anisotropic expression.[4,49] Bedded shale, with slightly lower clay content (average 32%), comparable TOC, and lower crack porosity (<0.006%), shows moderate anisotropy (ε = 0.2–0.6; γ = 0.3–0.6). Its interlayered silty quartz disrupts clay fabric continuity, leading to less aligned micro-cracks and thus reduced anisotropy. In contrast, massive shale, with low clay content and minimal TOC, and the lowest crack porosity (<0.003%) exhibits near isotropy (ε, γ → 0). The dominance of rigid minerals (quartz + feldspar >60%) and the absence of continuous bedding or organic alignment result in an isotropic elastic response, as predicted by Backus averaging theory for homogeneous media.[50,51] Thus, shale anisotropy is co-controlled by composition (TOC and clay) and micro-structure (micro-crack development), with laminated shales exhibiting the most significant combined effect.

This study investigates the correlation between anisotropy and micro-cracks using the M-T theoretical model, providing valuable insights for exploration and development of lacustrine shale reservoirs. Specifically, in seismic data interpretation, integrating shale anisotropy characteristics and dynamic effects of micro-cracks can improve reservoir prediction accuracy. For example, the significant anisotropy and bedding-parallel

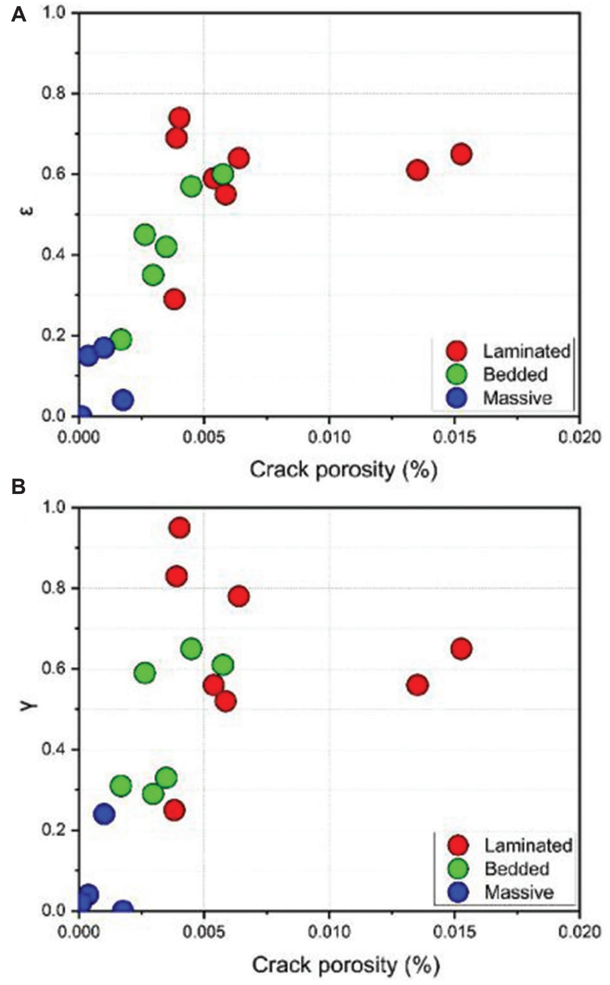

Figure 11. The relationships between the anisotropy parameter ε and the crack porosity (A), as well as between the anisotropy parameter γ and the crack porosity (B)

micro-cracks in laminated shale highlight the need for targeted exploration focus on such intervals. In addition, optimizing well locations to match dominant micro-cracks directions and considering anisotropy in fracturing designs can significantly enhance hydrocarbon recovery efficiency. Collectively, these findings provide critical, practice-oriented guidance for the efficient development of unconventional resources like shale oil and gas.

However, this study has some limitations. Firstly, due to limited core availability, only 4–6 samples were available for each structural type, potentially resulting in uncertainty when extrapolating to the entire reservoir. Future work should increase the sample size and combine digital rock physics to reduce statistical bias. Then, the model assumes an ideal uniform distribution of micro-cracks in the medium, which fundamentally differs from the complex heterogeneous fracture networks observed in real shales. This may lead to prediction biases in anisotropy characteristics. Therefore, future research could refine the model by incorporating both uniformly distributed random fractures and preferentially oriented bedding-parallel cracks, thereby capturing the heterogeneous characteristics of real reservoirs more accurately.

5. Conclusion

In this study, 17 shale samples from a Cretaceous lacustrine reservoir were classified into three structural types: Laminated, bedded, and massive, based on their micro-fabric characteristics. Ultrasonic velocity measurements were performed on 17 pairs of shale plugs under varied confining pressures to quantitatively analyze the relationship between micro-crack parameters and elastic anisotropy. The results indicate that the stress sensitivity of bedding-normal velocities relies on rock sedimentary structure, in the order of: laminated > bedded > massive. Specifically, laminated shales exhibit the most pronounced anisotropic properties, followed by bedded shales, while massive shales display the weakest anisotropic characteristics. Measured velocities showed good agreement with predictions from the M-T model, validating its applicability for structurally diverse shales. Furthermore, a trend was observed where a higher crack aspect ratio correlates with higher crack porosity in non-closable pores, a feature predominantly found in laminated samples. As crack density and porosity increase, the degree of anisotropy in lacustrine shales intensifies. Among the three structural types, laminated shales exhibit the highest crack porosity, which is consistent with their pronounced anisotropic characteristics. Within the studied lacustrine shales, sedimentary structure appears to be the dominant factor controlling micro-crack development and anisotropy, although clay and TOC also play contributory roles. This study has specific guiding significance for seismic anisotropy inversion, hydraulic fracturing design, or well logging interpretation.

Acknowledgments

We gratefully acknowledge the guidance of Professor Dehua Han from the Rock Physics Laboratory at the University of Houston, USA, in this project.

Funding

This research was supported by the National Natural Science Foundation of China (grant number: 42430810).

Conflict of interest

The authors declare that they have no conflicts of interest.

Author contributions

Conceptualization: Wenhui Tan, Yang Wang
Data curation: Wenhui Tan, Yang Wang
Formal analysis: Weihua Liu
Investigation: Weihua Liu
Methodology: Wenhui Tan
Supervision: Hui Shen
Visualization: Weihua Liu
Writing–original draft: Wenhui Tan
Writing–review & editing: Yang Wang

Availability of data

The data supporting this study are available from the corresponding author on reasonable request.

References

1. Zou CN, Yang Z, Zhu RK, *et al*. Progress in China's unconventional oil & gas exploration and development and theoretical technologies. *Acta Geol Sin*. 2015;89(6):979-1007.

   doi: 10.1111/1755-6724.12491

2. Jin ZJ, Wang GP, Liu GX, *et al.* Research progress and key scientific issues of continental shale oil in China. *Acta Petrol Sin*. 2021;42(7):821-835.

   doi: 10.7623/syxb202107001

3. Li MW, Ma XX, Jin ZJ, *et al*. Diversity in the lithofacies assemblages of marine and lacustrine shale strata and significance for unconventional petroleum exploration in China. *Oil Gas Geol*. 2022;43(1):1-25.

   doi: 10.11743/ogg20220101

4. Vernik L, Nur A. Ultrasonic velocity and anisotropy of hydrocarbon source rocks. *Geophysics*. 1992;57:727-735.

   doi: 10.1190/1.1443286

5. Vernik L, Landis C. Elastic anisotropy of source rocks: Implications for hydrocarbon generation and primary migration. *AAPG Bull*. 80(4):531-544.

6. Wright J. The effects of transverse isotropy on reflection amplitudes versus offset. *Geophysics*. 1987;52:564-567.

   doi: 10.1190/1.1442325

7. Sayers CM. Seismic anisotropy of shales. *Geophys Prospect*. 2005;53:667-676.

   doi: 10.4236/ijg.2016.73027

8. Vernik L. Chapter 3: Seismic Rock properties and rock physics. In: Vernik L, editor. *Seismic petrophysics in Quantitative Interpretation*. Houston: Society of Exploration Geophysicists; 2016. p. 43-86.

   doi: 10.1190/1.9781560803256.ch3

9. Zoback MD, Kohli AH. *Unconventional Reservoir Geomechanics: Shale Gas, Tight Oil, and Induced Seismicity.* Cambridge: Cambridge University Press; 2019.

10. Yin XY, Zong ZY, Wu GC. Research on seismic fluid identification driven by rock physics. *Sci Chin Earth Sci*. 2015;58:159-171.

    doi: 10.1007/s11430-014-4992-3

11. Chen HZ, Yin XY, Gao JH, Liu BY, Zhang GZ. Seismic inversion for underground fractures detection based on effective anisotropy and fluid substitution. *Sci China Earth Sci*. 2015;58:805-814.

    doi: 10.1007/s11430-014-5022-1

12. Liu Z, Zhang F, Li X. Elastic anisotropy and its influencing factors in organic-rich marine shale of southern China. *Sci China Earth Sci*. 2019;62:1805-1818.

    doi: 10.1007/s11430-019-9449-7

13. Vernik L, Liu X. Velocity anisotropy in shales: A petrophysical study. *Geophysics*. 1997;62(2):521-532.

    doi: 10.1190/1.1444162

14. Sone H, Zoback MD. Mechanical properties of shale-gas reservoir rocks-Part 1: Static and dynamic elastic properties and anisotropy. *Geophysics*. 2013;78:D381-D392.

    doi: 10.1190/geo2013-0050.1

15. Hornby BE, Schwartz LM, Hudson JA. Anisotropic effectivemedium modeling of the elastic properties of shales. *Geophysics*. 1994;59:1570-1583.

    doi: 10.1190/1.1443546

16. Sayers CM. The elastic anisotrophy of shales. *J Geophys Res*. 1994;99:767-774.

    doi: 10.1029/93JB02579

17. Lonardelli I, Wenk HR, Re Y. Preferred orientation and elastic anisotropy in shales. *Geophysics*. 2007;72:D33-D40.

    doi: 10.1190/1.2435966

18. Wenk HR, Lonardelli I, Franz H, Nihei K, Nakagawa S. Preferred orientation and elastic anisotropy of illite-rich shale. *Geophysics*. 2006;72:E69-E75.

    doi: 10.1190/1.2432263

19. Bandyopadhyay K. *Seismic Anisotropy-Geological Causes and its Implications to Reservoir Geophysics. Dissertation for Doctoral Degree*. Palo Alto: Stanford University; 2009.

20. Qian K, Zhang F, Chen S, Li X, Zhang H. A rock physics model for analysis of anisotropic parameters in a shale reservoir in Southwest China. *J Geophys Eng*. 2016;13:19-34.

    doi: 10.1088/1742-2132/13/1/19

21. Zhang F, Li X, Qian K. Estimation of anisotropy parameters for shale based on an improved rock physics model, part 1: Theory. *J Geophys Eng*. 2017;14:143-158.

    doi: 10.1088/1742-2140/14/1/143

22. Zhang F. Estimation of anisotropy parameters for shales based on an improved rock physics model, part 2: Case study. *J Geophys Eng*. 2017;14:238-254.

    doi: 10.1088/1742-2140/aa5afa

23. Zhang F. A modified rock physics model of overmature organicrich shale: Application to anisotropy parameter prediction from well logs. *J Geophys Eng*. 2019;16:92-104.

    doi: 10.1093/jge/gxy008

24. Tan KJ, Deng JX, Liu ZH, Sun X. Rock physical properties and variation patterns of Chang 7 lacustrine shale oil reservoir in the Triassic Yangchang Formation, Ordos Basin. *Chinese J Geophys*. 2025;68(2):652-667.

    doi: 10.6038/cjg2023Q0862

25. Liu WH, Wang Y, Shen H, Li M, Fan WH. Ultrasonic velocity anisotropy of Jurassic shales with different lithofacies. *J Geophys Eng*. 2024;21(4):1103-1118.

    doi: 10.1093/jge/gxae061

26. Vernik L. Microcrack-induced versus intrinsic elastic anisotropy in mature HC-source shales. *Geophysics*. 1993;58(11):1703-1706.

    doi: 10.1190/1.1443385

27. Ciz R, Shapiro SA. Stress-dependent anisotropy in transversely isotropic rocks: Comparison between theory and laboratory experiment on shale. *Geophysics*. 2009;74(1):D7-D12.

    doi: 10.1190/1.3008546

28. Sarout J, Molez L, Gueguen Y, Hoteit N. Shale dynamic properties and anisotropy under triaxial loading: Experimental and theoretical investigations. *Phys Chem Earth Parts A/B/C*. 2007;32(8):896-906.

    doi: 10.1016/J.PCE.2006.01.007

29. Sayers C, Munster J, King MS. Stress-induced ultrasonic anisotrophy in Berea sandstone. *Int J Rock Mech Mining Sci Geomech Abstr*. 1990,27:429-436.

    doi: 10.1016/0148-9062(90)92715-Q

30. Kohli AH, Zoback MD. Frictional properties of shale reservoir rocks. *J Geophys Res Solid Earth*. 2013;118(9):5109-5125.

    doi: 10.1002/jgrb.50346

31. Yan BH, Zhao JG, Xiao ZJ, *et al*. Analysis of elastic properties and anisotropic rock physics modeling of Qianjiang Formation shale. *Chinese J Geophys*. 2024;67(7):2802-2819.

    doi: 10.6038/cjg2022Q0724

32. Zhang JC, Lin LM, Li YX, Tang X, Zhu LL, Xin YW. Classification and evaluation of shale oil. *Earth Sci Front*. 2012;19(5):322-331.

33. Liu B, Lyu Y, Ran Q, *et al*. Geological conditions and exploration potential of shale oil in Qingshankou Formation, Northern Songliao Basin. *Oil Gas Geol*. 2014;35(2):280-285.

    doi: 10.11743/ogg20140216

34. Liu B, Shi JX, Fu XF, *et al*. Petrological characteristics and shale oil enrichment of lacustrine fine-grained sedimentary system: A case study of organic-rich shale in first member of Cretaceous Qingshankou Formation in Gulong Sag, Songliao Basin, NE China. *Petrol Explor Dev*. 2018;45(5):828-838.

    doi: 10.1016/S1876-3804(18)30091-0

35. Lazar OR, Bohacs KM, Macquaker JH, Schieber J, Demko T. Capturing key attributes of fine-grained sedimentary rocks in outcrops, cores, and thin sections: Nomenclature and description guidelines. *J Sediment Res*. 2015;85(3):230-246.

    doi: 10.2110/jsr.2015.11

36. Vernik L. Hydrocarbon generation-induced microcracking of source rocks. *Geophysics*. 1994;59(4):555-563.

    doi: 10.1190/1.1443616

37. Sun LD, Wang XJ, Feng ZH, *et al*. Formation mechanisms of nano-scale pores/fissures and shale oil enrichment characteristics for Gulong shale, Songliao Basin. *Oil Gas Geol*. 2023;44(6):1350-1365.

    doi: 10. 11743/ogg20230602

38. He WY, Zhao Y, Zhong JH, Sun NL. Characteristics and significance of micron pores and micron fractures in shale oil reservoirs of Cretaceous Qingshankou Formation in Gulong sag, Songliao Basin. *Lithol Reserv*. 2024;36(3):1-18.

39. Wang Z. Seismic anisotropy in sedimentary rocks, part 1: A single plug laboratory method. *Geophysics*. 2002;67(5):1415-1422.

    doi: 10.1190/1.1512787

40. Thomsen L. Weak elastic anisotropy. *Geophysics*. 1986;51(10):1954-1966.

    doi: 10.1190/1.1442051

41. David EC, Zimmerman RW. Pore structure model for elastic wave velocities in fluid-saturated sandstones. *J Geophys Res*. 2012;117(B7): B07210.

    doi: 10.1029/2012JB009195

42. Lo TW, Coyner KB, Toksöz MN. Experimental determination of elastic anisotropy of Berea sandstone, Chicopee shale, and Chelmsford granite. *Geophysics*. 1986;51(1):164-171.

    doi: 10.1190/1.1442029

43. Johnston JE, Christensen NI. Seismic anisotropy of shales. *J Geophys Res*. 1995;100:5991-6003.

44. Mori T, Tanaka K. Average stress in matrix and average elastic energy of materials with misfitting inclusions. *Acta Metall*. 1974;21(5):571-574.

doi: 10.1016/0001-6160(73)90064-3

45. Zhang L, Ba J, Fu LY, Carcione José M, Cao CH. Estimation of pore microstructure by using the static and dynamic moduli. *Int J Rock Mech Min Sci*. 2019;113:24-30.

    doi: 10.1016/j.ijrmms.2018.11.005

46. Shapiro SA. Elastic piezosensitivity of porous and fractured rocks. *Geophysics*. 2003;68(2):482-486.

    doi: 10.1190/1.1567215

47. Kaarsberg EA. Introductory studies of natural and artificial argillaceous aggregates by sound-propagation and x-ray diffraction methods. *J Geol*. 1959;67(4):447-472.

    doi: 10.1086/626597

48. Wenk HR, Voltolini M, Mazurek M, Loon LRV, Vinsot A. Preferred orientations and anisotropy in shales: Callovo-oxfordian shale (France) and Opalinus clay (Switzerland). *Clays Clay Miner*. 2008;56(3):285-306.

    doi: 10.1346/CCMN.2008.0560301

49. Curtis JB. Fractured shale-gas systems. *AAPG Bull*. 2002;86:1921-1938.

50. Backus GE. Long-wave elastic anisotropy produced by horizontal layering. *J Geophys Res*. 1962;67(11):4427-4440.

    doi: 10.JZ067i011p04427

51. Mavko G, Mukerji T, Dvorkin J. *The Rock Physics Handbook: Tools for Seismic Analysis of Porous Media*. 2nd ed. Cambridge: Cambridge University Press; 2009.

    doi: 10.1017/CBO9780511626753

ACCSCIENCE PUBLISHING

Journal of Seismic Exploration

ARTICLE

A physics-constrained sparse basis learning method for mixed noise suppression

Yongsheng Wang[1,2†], **Deying Wang**[3,4†], **Kai Zhang**[3], **Wenqing Liu**[4], **Longjiang Kou**[4], **and Huailiang Li**[1,2*]

[1]State Key Laboratory of Geohazard Prevention and Geoenvironment Protection, University of Technology, Chengdu, Sichuan, China

[2]PetroChina Qinghai Oilfield Company, Dunhuang, Gansu, China

[3]School of Geosciences, China University of Petroleum (East China), Qingdao, Shandong, China

[4]Seismic Data Processing and Interpretation Center, Research Institute of Petroleum Exploration and Development-Northwest, PetroChina, Lanzhou, Gansu, China

(This article belongs to the *Special Issue: Advanced Artificial Intelligence Theories and Methods for Seismic Exploration*)

Abstract

Suppressing complex mixed noise in seismic data poses a significant challenge for conventional methods, which often cause signal damage or leave residual noise. While sparse basis learning is a promising approach for this task, traditional data-driven learning methods are often insensitive to the physical properties of seismic signals, leading to incomplete noise removal and compromised signal fidelity. To address this limitation, we propose a physics-constrained sparse basis learning method for mixed noise suppression. Our method integrates local dip attributes—estimated and iteratively refined by a plane-wave destructor filter—as a physical constraint within the dictionary learning framework. This constraint guides the learning process to achieve high-fidelity signal reconstruction while effectively suppressing multiple noise types. Tests on complex synthetic and real data demonstrate that the proposed method outperforms conventional techniques and industry-standard workflows in attenuating mixed noise, including strong anomalous amplitudes, ground roll, and random and coherent components, thereby significantly enhancing the signal-to-noise ratio and imaging quality.

Keywords: Multiple-type noise suppression; Dictionary learning; Physical constraint; Plane-wave destructor filter

1. Introduction

The evolution of seismic data denoising techniques reflects a deepening understanding of signal and noise characteristics and the continuous refinement of processing methodologies.[1] Early methods primarily relied on fixed-basis transforms, such as the Fourier transform (F-K filtering) and the wavelet transform. These approaches operate on the assumption that effective signals and noise exhibit distinct characteristics in the transformed domain, allowing for their separation through filtering or thresholding.[2]

[†]*These authors contributed equally to this work.*

***Corresponding author:**
Huailiang Li
(lihl@cdut.edu.cn)

Citation: Wang Y, Wang D, Zhang K, Liu W, Kou L, Li H. A physics-constrained sparse basis learning method for mixed noise suppression. *J Seismic Explor*. 2025;34(4):42-59. doi: 10.36922/JSE025280034

Received: July 13, 2025

1st revised: August 25, 2025

2nd revised: September 6, 2025

Accepted: September 9, 2025

The underlying principle for many of these techniques is sparse representation, which aims to find the most compact signal representation within an overcomplete dictionary, thereby enabling effective compression, feature extraction, and denoising.[3,4] Transforms such as the curvelet and shearlet were developed to better represent the linear and curvilinear features common in seismic wavefields, offering improved performance over traditional wavelets in preserving edges and suppressing coherent noise.[5-7] However, the efficacy of these fixed-basis methods is inherently limited; they may introduce artifacts or damage signals when the characteristics of the signal and noise overlap in the transform domain.[8,9] To overcome the rigidity of fixed bases, adaptive dictionary learning methods such as K-singular value decomposition (K-SVD) and the method of optimal directions were introduced. These techniques learn the dictionary atoms directly from the data, allowing the basis to adapt to the specific morphological features of seismic signals.[10,11]

In recent years, deep learning (DL) has been widely applied to seismic data denoising due to its powerful nonlinear modeling and feature learning capabilities.[12] Initial supervised models, such as the denoising convolutional neural network, demonstrated state-of-the-art performance by using residual learning to focus on noise components.[13] However, their reliance on large volumes of paired clean and noisy data for training significantly increases the preprocessing workload and limits their application in scenarios where clean reference data is unavailable.[13] To address this, recent research has shifted toward more flexible DL paradigms. Self-supervised learning models, for instance, can be trained effectively on noisy data alone, eliminating the need for clean labels by leveraging the statistical properties of the data and noise.[14] Furthermore, physics-informed neural networks (PINNs) have emerged as a promising direction. By incorporating physical laws, such as the acoustic wave equation, directly into the network's loss function, PINNs ensure that the denoising process respects the underlying wave propagation physics, which enhances generalization and produces more physically plausible results.[15]

Despite these advancements, significant challenges remain. Data-driven dictionary learning, if unconstrained, is prone to learning non-physical features that mimic noise, leading to incomplete noise suppression and signal damage. DL models, while powerful, often lack interpretability, and their performance can be unreliable when applied to data with characteristics different from the training set.[9,16,17] To address these issues, this paper proposes a physics-constrained sparse basis learning method for mixed noise suppression. This method constructs a joint optimization model that introduces a dip regularization term, penalizing components in the reconstructed signal that do not conform to local coherence. By simultaneously imposing a smoothness constraint on the dictionary atoms, the learned basis is guided to be more physically meaningful. A plane-wave destructor (PWD) filter is used to iteratively estimate and update the local dip field, ensuring that the physical constraint adapts to the progressively refined signal. Tests on synthetic and real data demonstrate that our method outperforms conventional techniques in suppressing complex mixed noise while preserving the integrity of the effective signal.

2. Materials and methods

2.1. Dip-constrained and gradient-optimized learning framework

The core idea of the novel prestack seismic data joint denoising framework proposed in this study is to combine the signal representation capability of sparse transforms with the dip attributes of effective signals. This integration aimed to achieve high-fidelity, effective signal reconstruction while simultaneously performing multi-type noise suppression.[18]

Prestack seismic data $Y \in \mathbb{R}^{N_t \times N_z}$ (where N_t represents the number of time samples and N_z represents the number of traces) can be expressed as the sum of effective seismic signals $X \in \mathbb{R}^{N_t \times N_z}$ and multiple types of noise $N \in \mathbb{R}^{N_t \times N_z}$:

$$Y{=}X{+}N \tag{I}$$

The primary goal of denoising was to estimate the effective signal X from the raw data Y. Within the framework of basis learning, we assume that the effective signal X can be approximately represented by a dictionary (set of basis functions) $D \in \mathbb{R}^{N_t \times N_z}$ and its corresponding sparse coefficient matrix $A \in \mathbb{R}^{N_t \times N_z}$:

$$X{=}{\approx}DA \tag{II}$$

Here, the column vectors of $D = [d_1,d_2...,d_{Nk})]$, denoted as d_j, are referred to as atoms or basis functions, and N_k is the number of atoms. Each column a_i of the sparse coefficient matrix A represents the sparse representation of the corresponding trace x_i under the dictionary D. The core challenge is to learn a dictionary D that provides a compact representation of the effective signal features and to solve for the corresponding sparse coefficients A.

Conventional basis function learning is achieved by solving the following optimization problem:

$$\overset{min}{D,A}\left\| Y - DA \right\|_F^2 + \lambda_s R_s(A), \tag{III}$$

where $\|Y-DA\|_F^2=\sum_{i,j}\left(Y_{i,j}-(DA)_{i,j}\right)^2$ represents the data fidelity term, which measures the error between the reconstructed data DA and the Raw data Y. $R_s(A)$ is the regularization term for the sparse coefficients A, used to introduce a sparsity prior. The L_1-norm regularization, i.e., $\mathcal{R}_s(A)=\|A\|_1=\sum_{i,j}\|A_{i,j}\|$, is commonly used to induce sparse solutions, meaning that the information for each seismic trace can be represented by a linear combination of a few atoms from the dictionary.[6] $\lambda_s > 0$ represents the weighting balance between the data fidelity term and the sparse regularization term. The selection of an appropriate value for the hyperparameter λ_s is critical to the success of the denoising task, as it governs the trade-off between fitting the data and enforcing sparsity. A very small λ_s would cause the optimization to prioritize the data fidelity term, leading the model to fit the noisy data Y too closely and fail to remove noise. Conversely, a very large λ_s would heavily penalize non-sparse solutions, forcing the coefficient matrix A to be extremely sparse, at the risk of over-smoothing the data and removing important features of the effective signal. Therefore, an optimal λ_s must be chosen to ensure that the sparsity constraint is strong enough to separate noise, while the data fidelity term preserves the integrity of the underlying signal. The optimal value is data-dependent, influenced by factors such as the noise level, and is typically determined empirically.

In prestack data, effective reflection signals typically exhibit good spatial coherence and predictable dips within local regions. For instance, in common midpoint gathers or common offset gathers, reflection events possess specific kinematic characteristics. This coherence is a key feature that distinguishes signals from various interferences such as random noise, linear noise, anomalous amplitudes, and ground roll. To make the basis learning framework more suitable for seismic data denoising and to enhance denoising performance by incorporating physical meaning, this study introduced local dip attributes as a physical constraint within the learning framework.[16]

This research presents a dip regularization term to penalize components in the reconstructed signal DA that does not conform to local coherence. This constraint was built upon the local dip $P=\{p_{i,j}\}$ (the local dip at data point (i,j)). First, we defined a linear operator L_p, which depends on the local dip field P and is used to enhance signal smoothness along the dip direction or to suppress different components. Ideally, if the signal DA is perfectly aligned along the dip P, then the value of $L_p\,(DA)$ will be close to zero. This constraint term can be expressed as:

$$\text{will be close to } R_{coh}(DA,P)=\|L_p(DA)\|_F^2, \tag{IV}$$

where the local dip field P can be estimated, computed, and updated during the iterative process based on the current reconstructed signal DA, allowing this constraint to adaptively match the local structural features of the data.

This paper posits that the basic building blocks of effective signals (atoms in the dictionary D) inherently possess certain physical properties. For example, they should exhibit smoothness and band-limited characteristics, rather than containing excessive high-frequency noise or irregular oscillations. To ensure that the learned atoms are more physically meaningful, this method imposes a smoothness constraint on the dictionary D itself by penalizing its gradient:

$$\min_{D,A,P} j(D,A,P)=\|Y-DA\|_F^2+\lambda_s\|A\|_1+\lambda_{coh}\|L_p(DA)\|_F^2 +\lambda_{atom}\|\nabla D\|_F^2 \tag{V}$$

where λ_s, λ_{coh}, and λ_{atom} are regularization parameters used to balance the weights of different constraints. The local dip field P, as part of the regularization term, reflects the model's adaptability to data characteristics. The objective function above, by jointly optimizing the dictionary D, sparse coefficients A, and physical parameter P, yields a solution that fits the effective signal while satisfying both sparsity and physical priors.

Given that the objective function $j\ (D,\ A,\ P)$ is non-convex with respect to D, A, and P, we employed an alternating iterative optimization strategy that decomposes the problem into the following four sub-steps:

Sub-step one: Initialization

(i) Initialize dictionary $D^{(0)}$: Randomly select data patches from the raw data Y or use Ricker wavelets for initialization
(ii) Initialize sparse coefficients $A^{(0)}$: Use a zero matrix or small random values
(iii) Initialize local dip field $P^{(0)}$: Estimate from the raw data Y using the PWD method
(iv) Set current iteration $t = 0$ and maximum iterations T_{max}.

Sub-step two: Updating sparse coefficients

(i) Fix $D^{(t)}$ and $P^{(t)}$ and establish the objective function for solving A:

$$A^{(t+1)}=\underset{A}{\operatorname{argmin}}\|Y-D^{(t)}A\|_F^2+\lambda_s\|A\|_1+\lambda_{coh}\|L_{P^{(t)}}(D^{(t)}A)\|_F^2 \tag{VI}$$

(ii) The function above is an L_1-norm minimization problem with a quadratic regularization term. Assuming $L_{P(t)}$ is a linear operator, let $Q^{(t)}=\mathcal{L}_{P^{(t)}}D^{(t)}$. Then, this subproblem can be rewritten as:

$$A^{(t+1)}=\underset{A}{\operatorname{argmin}}\|Y-D^{(t)}A\|_F^2+\lambda_s\|A\|_1+\lambda_{coh}\|Q^{(t)}A\|_F^2 \tag{VII}$$

This can be transformed into:

$$A^{(t+1)} = \underset{A}{\operatorname{argmin}} \left\| \begin{pmatrix} Y \\ 0 \end{pmatrix} - \begin{pmatrix} D^{(t)} \\ \sqrt{\lambda_{coh}} Q^{(t)} \end{pmatrix} A \right\|_F^2 + \lambda_s \tag{VIII}$$

This problem can be efficiently solved using methods such as the fast iterative shrinkage-thresholding algorithm or the alternating direction method of multipliers.

Sub-step three: Updating the dictionary

(i) Fix $A^{(t+1)}$ and $P^{(t)}$ and solve the subproblem for D:

$$\mathrm{D}^{(t+1)} = \underset{\mathrm{D}}{\operatorname{argmin}} \left\| \mathrm{Y} - \mathrm{DA} \right\|_{\mathrm{F}}^{(t)2} + \lambda_{\mathrm{coh}} \left\| \mathcal{L}_{\mathrm{P}^{(t)}} (\mathrm{DA}^{(t+1)}) \right\|_{\mathrm{F}}^2 + \lambda_{\mathrm{atom}} \left\| \nabla \mathrm{D} \right\|_{\mathrm{F}}^2 \tag{IX}$$

(ii) The equation above is a quadratic programming problem with respect to D. If optimized column-by-column d_k, it can be simplified as:

$$\underset{D}{\min} \left\| \begin{pmatrix} Y \\ 0 \\ 0 \end{pmatrix} - \begin{pmatrix} I \otimes (A^{(t+1)})^T \\ \sqrt{\lambda_{coh}} M_{P^{(t)},\, A^{(t+1)}} \\ \sqrt{\lambda_{atom}} \mathrm{N} \end{pmatrix} vec(D) \right\|_2^2 \tag{X}$$

where M and N are matrix forms of expressing $\left\| \mathcal{L}_{P^{(t)}} (DA^{(t+1)}) \right\|_F^2$ and $\left\| \nabla D \right\|_F^2$ as quadratic forms with respect to $vec(D)$; $\otimes$ denotes the Kronecker product; and $vec(.)$ is the vectorization operator. This results in a large-scale least squares problem that can be solved using iterative methods such as gradient descent or the conjugate gradient method.[9]

Sub-step four: Local dip field update

Fix $D^{(t+1)}$ and $A^{(t+1)}$ to obtain the current effective signal estimate $X^{(t+1)}=D^{(t+1)} A^{(t+1)}$. Then, update the local dip field $X^{(t+1)}$ based on P:

$$P^{(t+1)} = \mathrm{PWD}(X^{(t+1)}) \tag{XI}$$

2.2. Plane-wave deconstruction filtering dip angle estimation

In the aforementioned constrained learning framework, the core of the physical constraint lies in the quantification and utilization of seismic signal local coherence. The PWD filter, proposed and developed by Sergey Fomel, cannot only be used to estimate the local dip field but also directly serve as a coherence constraint operator, providing strong support for this objective.[17]

The PWD theory assumes that, within a local time-space window, seismic data can be approximately viewed as a superposition of a series of plane waves. A 2D plane wave can be expressed as:

$$d(t,x) = f(t-\sigma x), \tag{XII}$$

where σ represents the local dip of the plane wave. PWD is essentially a steerable prediction-error filter. The prediction error at the filter's output is minimized when the correct local dip is applied. Any components that do not conform to this local plane wave model (such as various types of noise) cannot be effectively predicted and thus manifest as larger energy at the filter output. Assuming a 2D seismic data $d(t,x)$, the theory aims to predict the value of $d(t,x)$, based on information from neighboring traces. According to the plane wave assumption, the following differential relationship is derived:

$$\frac{\partial d}{\partial x} + \sigma \frac{\partial d}{\partial t} = 0 \tag{XIII}$$

The above equation indicates that the directional derivative along the plane wave direction (t,x) domain is zero. PWD is the discrete realization of this differential operator. A first-order PWD operator can be used to predict the value at a central point $d_{i,j.}$ Its predicted value $d_{Ei,j}$ is calculated from two neighboring points $d_{i,j-1}$ and $d_{i,j+1}$ in the x-direction. To introduce the dip σ into the prediction, a shift in the time direction needs to be considered:

$$d_{Ei,j} = \frac{1}{2}\left[d_{i-round(\sigma),j-1} + d_{i+round(\sigma),j+1} \right] \tag{XV}$$

To address the precision issue caused by the integer shifts in the above equation, Fomel proposed more accurate Taylor expansion and finite-difference methods:

$$e_{i,j} = d_{i,j} - [c_{-1}(\sigma) d_{i,j-1} + c_1(\sigma) d_{i,j+1}], \tag{XV}$$

where $e_{i,j}$ represents the prediction error of $d_{i,j}$. c_{-1} (σ) and c_1 (σ) are functions of the local dip σ, used to perform data interpolation or extrapolation along the dip direction. In practical applications, a separable approximation is commonly used, where a three-point PWD operator F_σ applied to a data point $d_{i,j}$ can be approximated as: can be approximated as

$$F_\sigma(d_{i,j}) \approx \frac{d_{i,j+1} - d_{i,j-1}}{2\Delta x} - \sigma_{i,j} D_t(d_{i,j}) \tag{XVI}$$

where D_t is a differential operator in the time direction, and $\sigma_{i,j}$ is the local dip at point (i,j). The output energy reflects the degree to which the data deviates from the local plane wave assumption. Conversely, this can be used to find a dip value σ that minimizes the output energy of the PWD filter. For each local window in the data, the optimal local dip σ is estimated by solving the following minimization problem:

$$\underset{\sigma}{\min} \left\| \mathcal{F}_\sigma(d) \right\|_F^2, \tag{XVII}$$

where d represents the data within the local window, and F_σ is the PWD operator parameterized by the dip σ.

The PWD theory aligns well with the joint denoising framework proposed in this study, providing a concrete implementation for crucial steps of the algorithm. In our objective **Equation (VI)**, the local coherence constraint term is $\lambda_{coh}\left\|\mathcal{L}_P(DA)\right\|_F^2$. We define the PWD operator as L_P, so this constraint term becomes:

$$R_{coh}(DA,P)=\left\|F_{P\sigma}(DA)\right\|_F^2 \quad \text{(XVIII)}$$

where, $P \equiv \sigma(t,x)$ represents the local dip field required by the PWD, and F^{σ} is the PWD operator guided by this dip field. It constrains all components in the reconstructed signal DA that cannot be predicted by the local plane wave model.

Furthermore, for sub-step four predicted by the local plane **(Equation VI)**—this can be achieved by solving the PWD-based dip estimation problem:

$$P^{(t+1)} = \underset{P}{\overset{argmin}{}}\left\|\mathcal{F}_P(X^{(t+1)})\right\|_F^2 \quad \text{(XIX)}$$

This process ensures that the dip field consistently aligns with the continuously improving signal estimation throughout the iterative process, thereby guiding the entire optimization toward clearer physical meaning and a more distinct signal structure.

2.3. Learning-based seismic data denoising framework

Unlike the training phase, where D, A, and P are optimized simultaneously, in the denoising phase, the dictionary D_{opt} and the dip field P_{opt} are treated as known optimal parameters. The objective function for solving the sparse coefficient matrix A_f is:

$$\underset{A}{\overset{min}{}}\left\|Y-D_{opt}A\right\|_F^2+\lambda_s\left\|A\right\|_1+\lambda_{coh}\left\|L_{P_{opt}}(D_{opt}A)\right\|_F^2, \quad \text{(XX)}$$

where $\left\|Y-D_{opt}A\right\|_F^2$ is the data fidelity term, which ensures that the sparse representation, after reconstruction using the optimal dictionary D_{opt}, has minimal error with respect to the raw data Y, thus preserving the fidelity of the denoising process. The term $\lambda_s\left\|A\right\|_1$ is the sparse regularization term, encouraging the solution to be represented sparsely using only a few atoms from D_{opt}. $\lambda_{coh}\left\|\mathcal{L}_{P_{opt}}(D_{opt}A)\right\|_F^2$ is the dip constraint term, which uses the estimated dip field P_{opt} to enforce structural constraints on the denoised data, requiring that the final denoising result conforms to the local coherence structure defined by P_{opt}.

By solving the optimization problem in **Equation I**, we obtain the sparse coefficient matrix A_f. Combining it with D_{opt} yields the final denoising result:

$$X_f = D_{opt}A_f \quad \text{(XXI)}$$

The proposed method achieves a relative balance among data fidelity, sparse representation, and structural constraint. The estimated noise $N_e = Y - X_f$ includes interference components that are neither effectively represented by the dictionary nor conform to the local coherence constraint. The proposed method comprises two distinct phases within a single workflow, as illustrated in Figure 1: A learning phase and an application phase. The "iterative optimization" block constitutes the learning phase, during which the optimal dictionary (D_{opt}) and dip field (P_{opt}) are learned from the raw data. The subsequent steps form the application phase, in which these learned parameters are used to process the raw data once to obtain the final denoised result. Unlike the learning phase, where D, A, and P need to be optimized simultaneously, in the application phase, the dictionary D_{opt} and dip field P_{opt} are treated as known, optimal parameters.

3. Results

3.1. Synthetic data example

To validate the proposed method, we conducted comparative denoising experiments on three synthetic datasets (Blocks A, B, and C), derived from a complex physical model based on a block in Western China. The performance of our method was benchmarked against three techniques: shearlet transform, DL model (a classic supervised learning framework based on the denoising convolutional neural network), and traditional dictionary learning. The first dataset, Block A, was contaminated with strong anomalous amplitude interference, random noise, and coherent noise, as shown in the raw shot gather in Figure 2A. Figure 2 compares the denoising results, where the proposed method (Figure 2E) effectively removes vertical interference while preserving signal continuity, outperforming the shearlet (Figure 2B), DL (Figure 2C), and traditional dictionary learning (Figure 2D) methods, which exhibit residual noise or signal loss. The removed noise profiles are displayed in Figure 3. The results from the comparative methods show significant signal leakage (Figure 3A-C), whereas the noise removed by our method consists primarily of interference, with almost no effective signal components, demonstrating superior signal preservation (Figure 3D). Figure 4 presents the final constrained dip fields, where the result from our method (Figure 4E) exhibits weaker residual noise and better preservation of effective signal features compared to the raw data and other results (Figure 4A-D). Finally, the dictionary iteration process is shown in Figure 5. Compared to the initial dictionary (Figure 5A) and the traditional result (Figure 5B), the dictionary learned by the proposed method (Figure 5C) more effectively captures signal features while discarding noise elements.

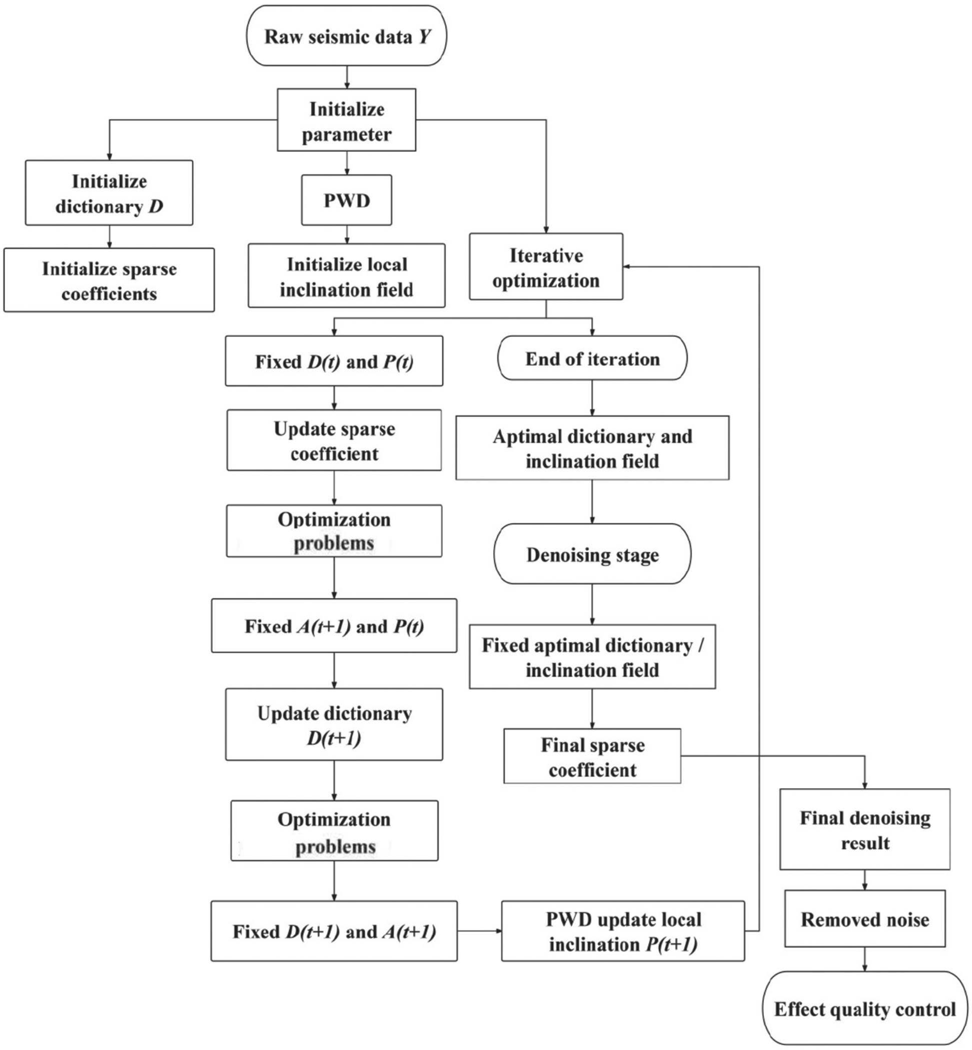

Figure 1. Flowchart of the proposed method
Abbreviation: PWD: Plane-wave destructor.

The second dataset, Block B, was characterized by strong ground roll, as depicted in Figure 6A. The results in Figure 6 demonstrate that while the benchmark methods (Figure 6B-D) struggled to suppress the ground roll, our proposed method (Figure 6E) achieved excellent multi-type noise removal while preserving the underlying signal. The removed noise sections in Figure 7 confirm this: While the other methods showed significant signal leakage (Figure 7A-C), our method successfully isolated the ground roll (Figure 7D). The corresponding dip fields and dictionary iterations are shown in Figures 8 and 9, respectively. The conclusions are consistent with those of the first experiment: In contrast to the dip fields of the raw data (Figures 8A), the shearlet result (Figures 8B), the deep learning result (Figures 8C), and the traditional dictionary learning result (Figures 8D), our method produced a much cleaner dip field (Figures 8E). Additionally, when compared with the initial dictionary (Figure 9A) and the result from traditional dictionary learning (Figure 9B), our method yielded a dictionary more representative of the true signal structure (Figure 9C). The third dataset, Block C, contained a complex mix of strong noise, including intermixed vertical amplitudes and coherent acquisition noise (Figure 10A). As illustrated in Figure 10, the comparative methods (Figure 10B-D) had a minimal effect on this complex noise, while the proposed method (Figure 10E) effectively resolved the issue. Figure 11 further depicts that the other techniques showed a mixture of noise and signal in the removed components (Figure 11A-C), whereas our method cleanly separated the complex noise structures (Figure 11D). These findings are further validated in Figure 12 and Figure 13. In contrast to the dip fields of the raw data (Figure 12A), the shearlet result (Figure 12B), the deep learning result (Figure 12C),

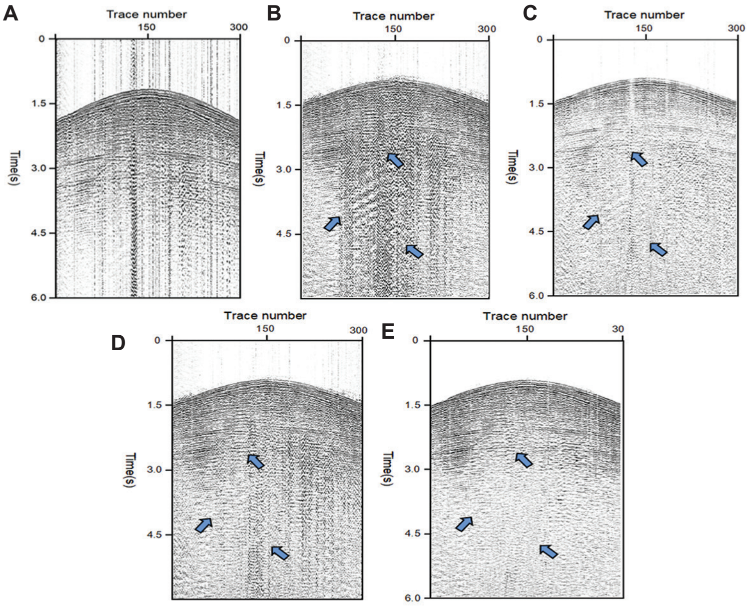

Figure 2. Raw data and denoised data of Block A. (A) Raw data. (B) Result using shearlet. (C) Result using deep learning. (D) Result using traditional dictionary learning. (E) Result using the proposed method.

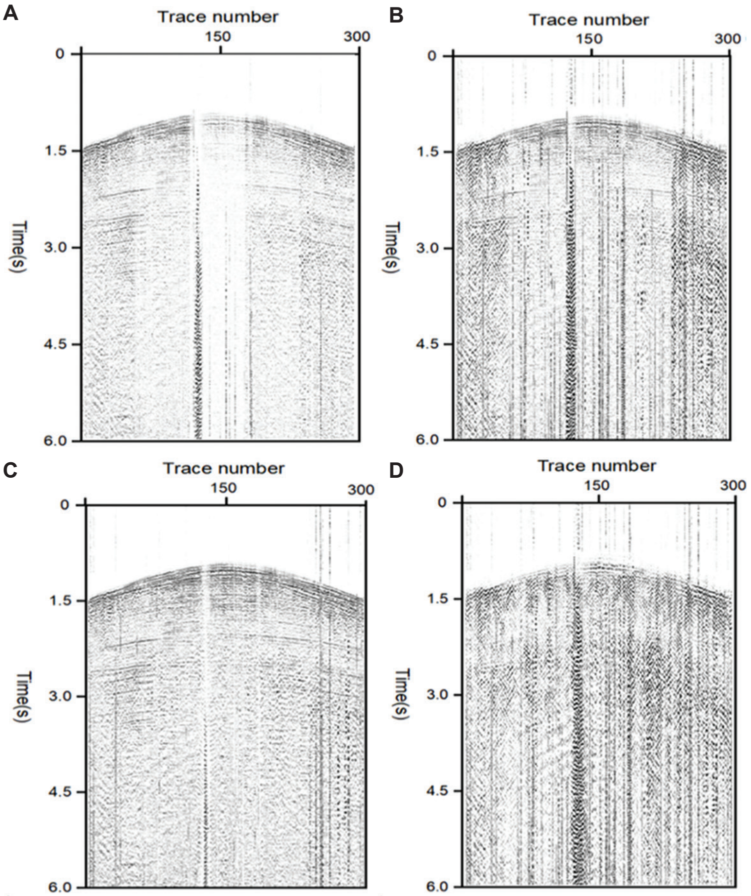

Figure 3. Removed noise using different methods for Block A. (A) Removed noise using shearlet. (B) Removed noise using deep learning. (C) Removed noise using traditional dictionary learning. (D) Removed noise using the proposed method.

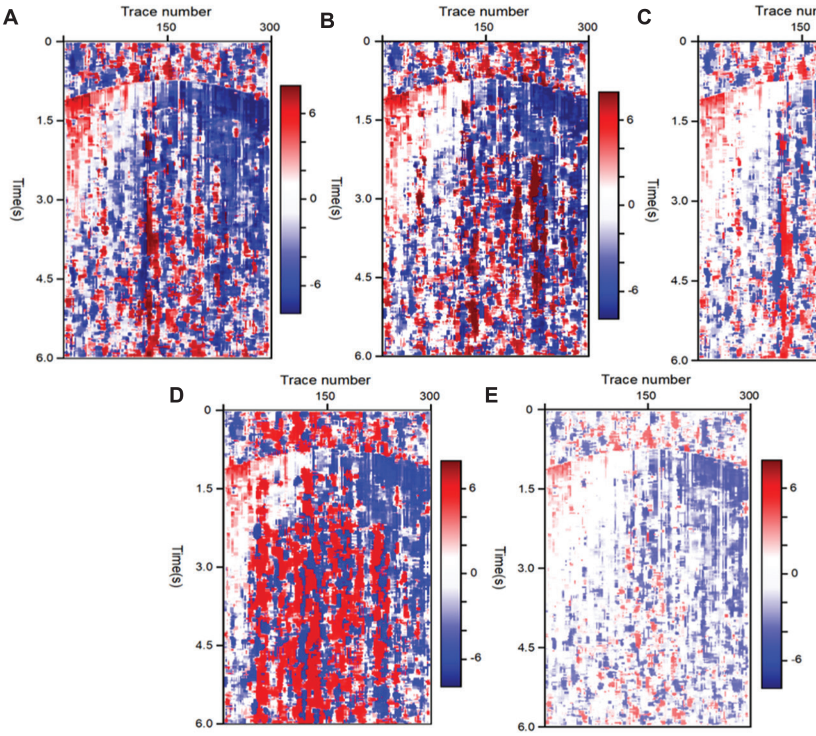

Figure 4. Dip fields of raw data and denoised data for Block A. (A) Dip field of raw data. (B) Dip field of result using shearlet. (C) Dip field of result using deep learning. (D) Dip field of result using traditional dictionary learning. (E) Dip field of result using the proposed method.

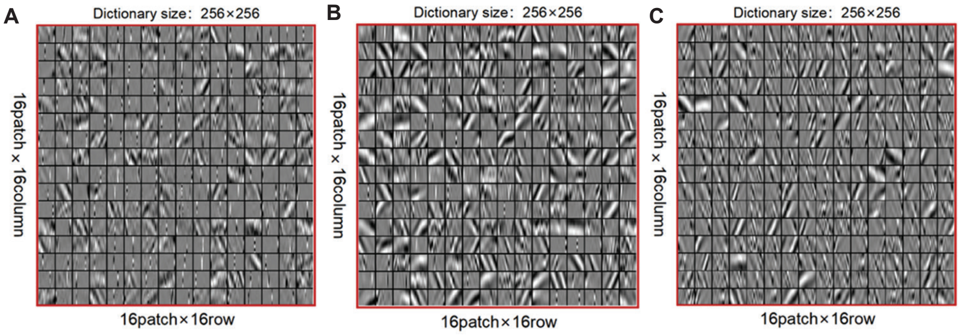

Figure 5. Initial dictionary and final learned dictionary of Block A. (A) Initial dictionary. (B) Result using traditional dictionary learning. (C) Result using the proposed method.

and the traditional dictionary learning result (Figure 12D), our method yields a cleaner final dip field (Figure 12E). Similarly, when compared with the initial dictionary (Figure 13A) and the result from traditional dictionary learning (Figure 13B),our method produces a more signal-focused dictionary (Figure 13C). Finally, the stacked sections for all three blocks are presented. For Block A (Figure 14), Block B (Figure 15), and Block C (Figure 16), the stacks processed by our method consistently demonstrated significant improvements in signal-to-noise ratio and continuity of geological events compared to the raw data and the results from the benchmark methods. In all cases, weak signals previously masked by strong noise were effectively recovered, highlighting the practical applicability of the proposed approach.

3.2. Real data example

To further validate the effectiveness and applicability of our method, we processed real seismic data from a work area in Western China. The performance was benchmarked against a DL method and a conventional industrial workflow.

A raw shot gathered from the dataset is shown in Figure 17A, which is heavily contaminated by severe ground

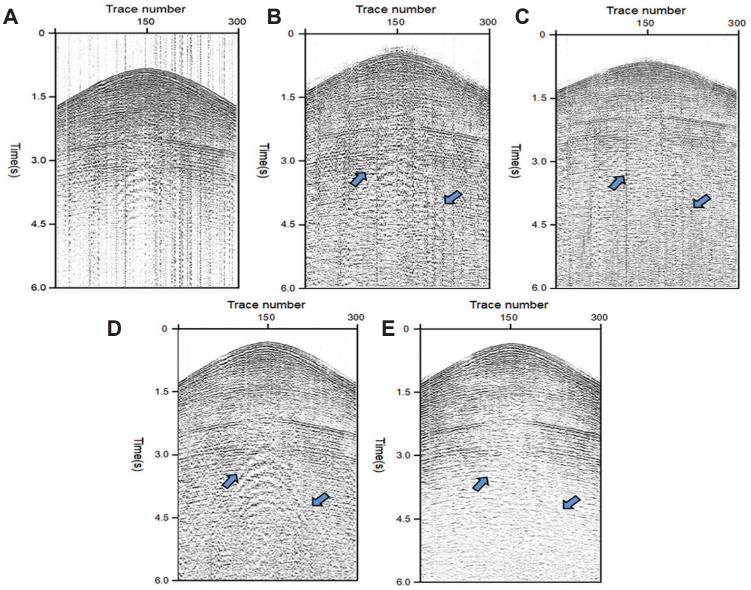

Figure 6. Raw data and denoised data for Block B. (A) Raw data. (B) Result using shearlet. (C) Result using deep learning. (D) Result using traditional dictionary learning. (E) Result using the proposed method.

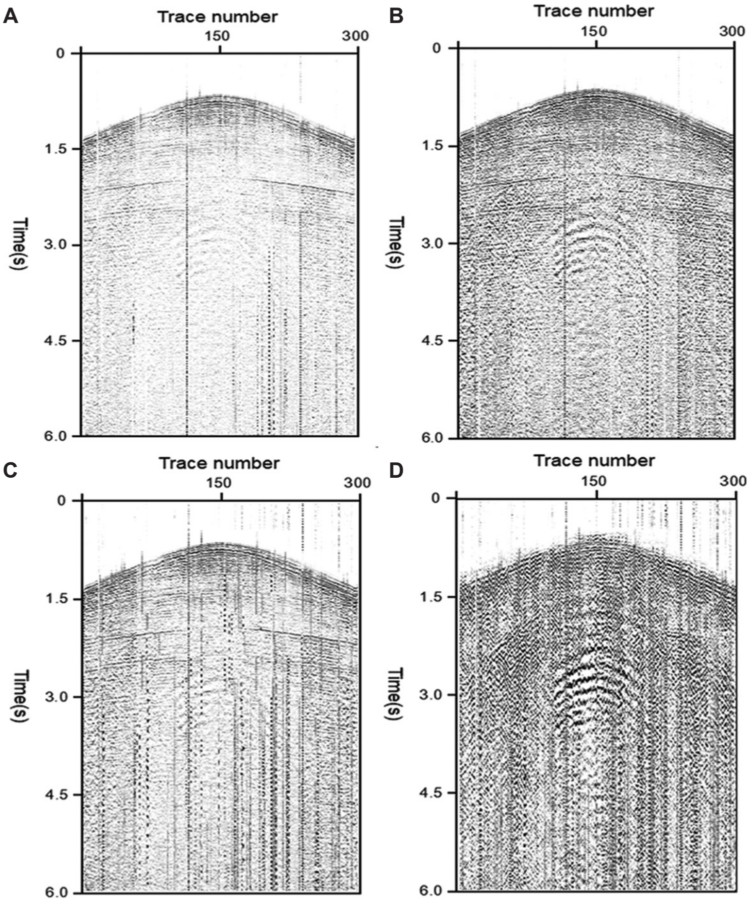

Figure 7. Removed noise using different methods for Block B. (A) Removed noise using shearlet. (B) Removed noise using deep learning. (C) Removed noise using traditional dictionary learning. (D) Removed noise using the proposed method.

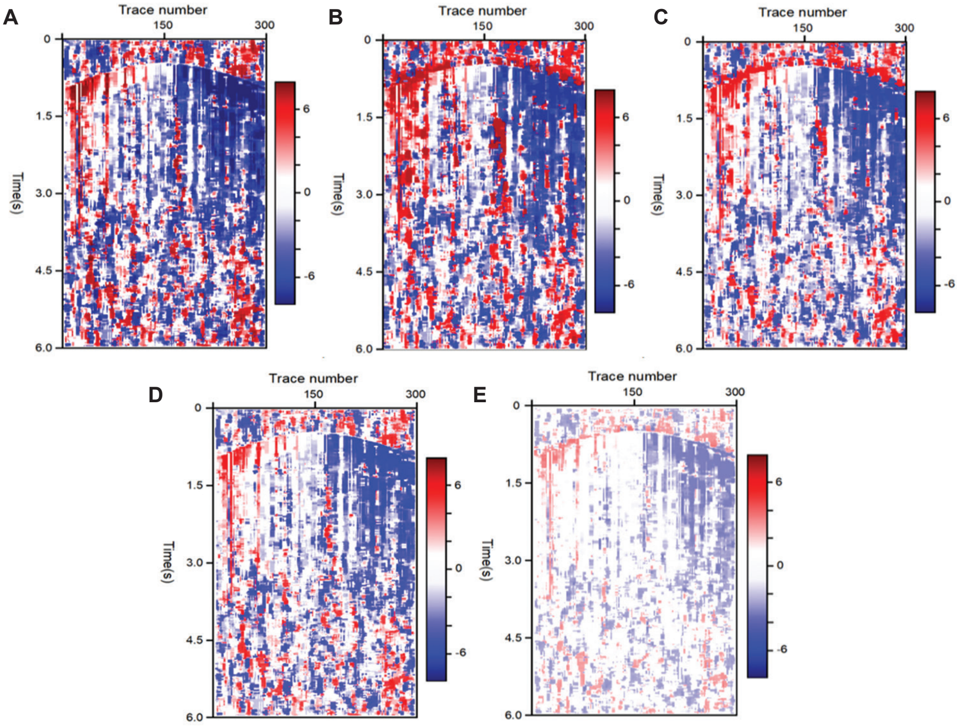

Figure 8. Dip fields of raw and denoised data from Block B. (A) Dip field of raw data. (B) Dip field of result using shearlet. (C) Dip field of result using deep learning. (D) Dip field of result using traditional dictionary learning. (E) Dip field of result using the proposed method.

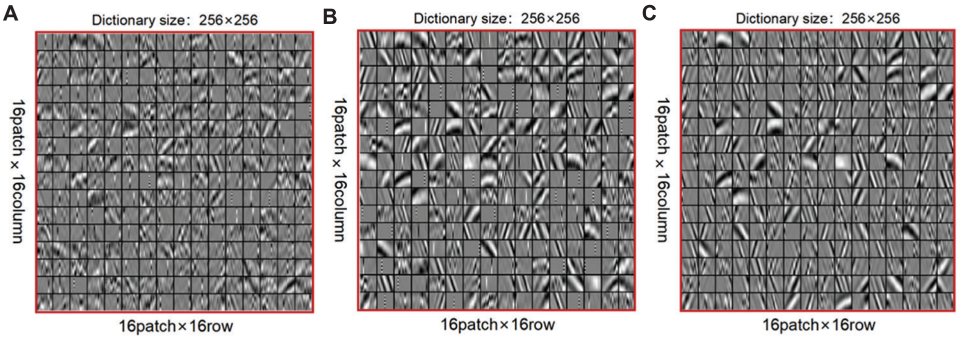

Figure 9. Initial dictionary and final learned dictionary of Block B. (A) Initial dictionary. (B) Result using traditional dictionary learning. (C) Result using the proposed method.

roll and random noise. This results in a low signal-to-noise ratio, where effective signals are obscured. Figure 17 presents the denoising results, displaying that all three methods removed a substantial amount of noise (Figure 17B-D). For a more detailed comparison of signal preservation, a partial enlargement is provided in Figure 18. In contrast to the raw data (Figure 18A), the DL method produced a cleaner result but with subtle smearing along the reflections (Figure 18B), and the conventional workflow left noticeable residual noise and compromised the continuity of reflection events (Figure 18C). The result from our proposed method (Figure 18D), however, shows superior noise removal while preserving signal integrity. The noise profiles for each method are depicted in Figure 19A-C. The coherence plots[19-21] for the DL method (Figure 19D) and the conventional workflow (Figure 19E) exhibit higher coherence values along noise and main reflection events, indicating weaker denoising and poorer signal preservation. The plot for our method (Figure 19F) demonstrates significantly lower correlation between the removed noise and the denoised result, confirming higher-fidelity separation of signal from noise. Finally, we evaluated the impact of denoising on seismic imaging by comparing stacked sections for two sub-regions. For region A, shown in Figure 20, the stacked

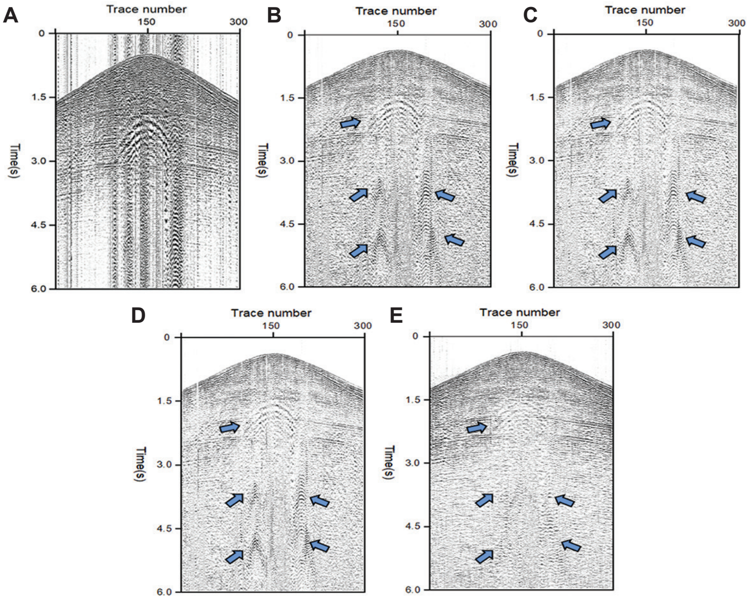

Figure 10. Raw data and denoised data of Block C. (A) Raw data. (B) Result using shearlet. (C) Result using deep learning. (D) Result using traditional dictionary learning. (E) Result using the proposed method.

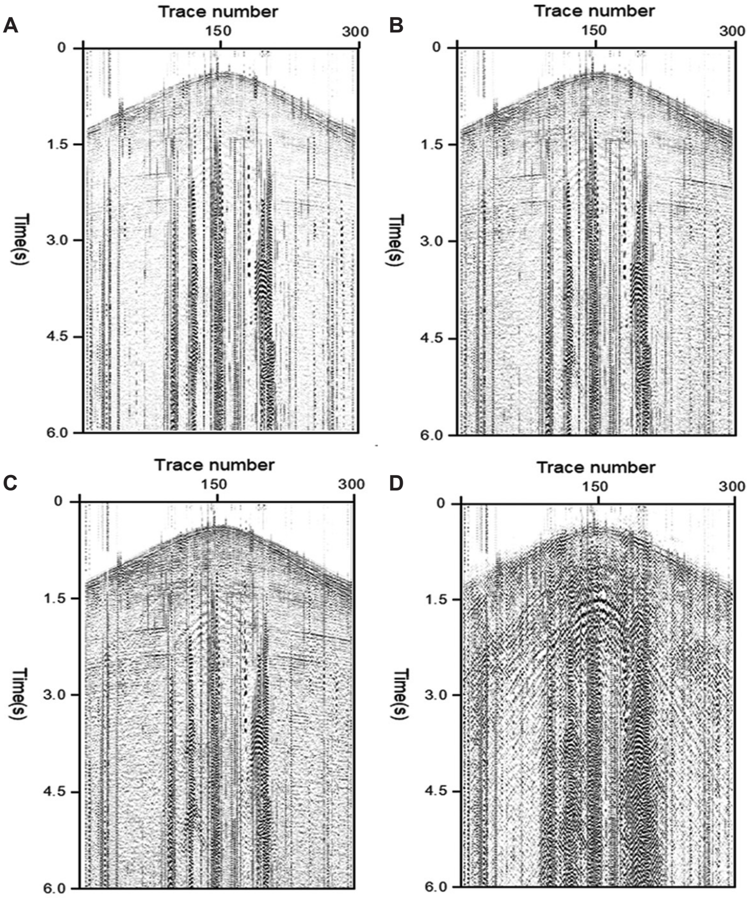

Figure 11. Removed noise using different methods for Block C. (A) Removed noise using shearlet. (B) Removed noise using deep learning. (C) Removed noise using traditional dictionary learning. (D) Removed noise using the proposed method.

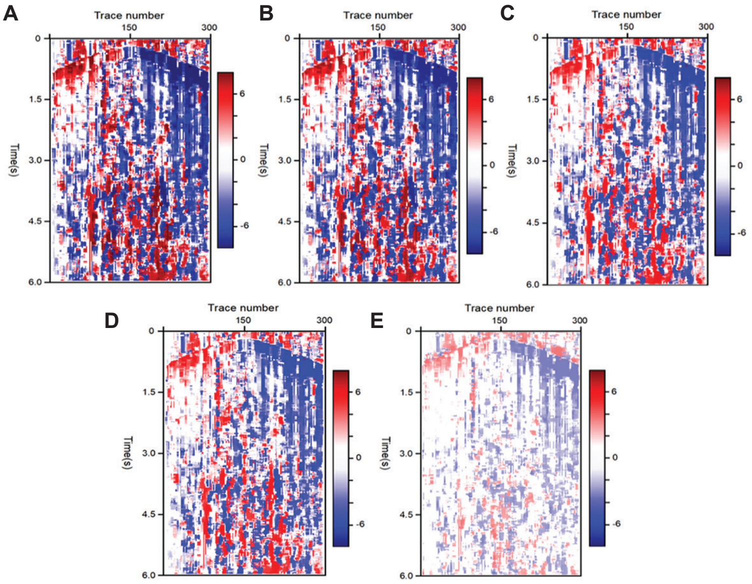

Figure 12. Dip fields of raw data and denoised data from Block C. (A) Dip field of raw data. (B) Dip field of result using shearlet. (C) Dip field of result using deep learning. (D) Dip field of result using traditional dictionary learning. (E) Dip field of result using the proposed method.

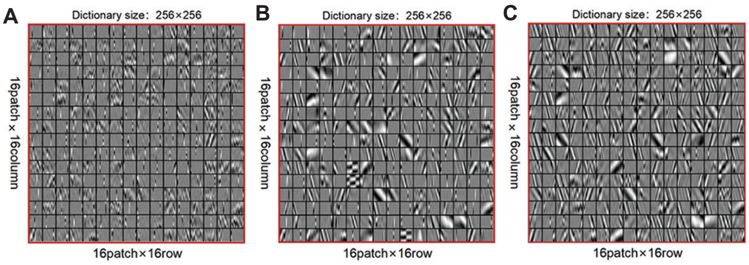

Figure 13. Initial dictionary and final learned dictionary for Block C. (A) Initial dictionary. (B) Result using traditional dictionary learning. (C) Result using the proposed method.

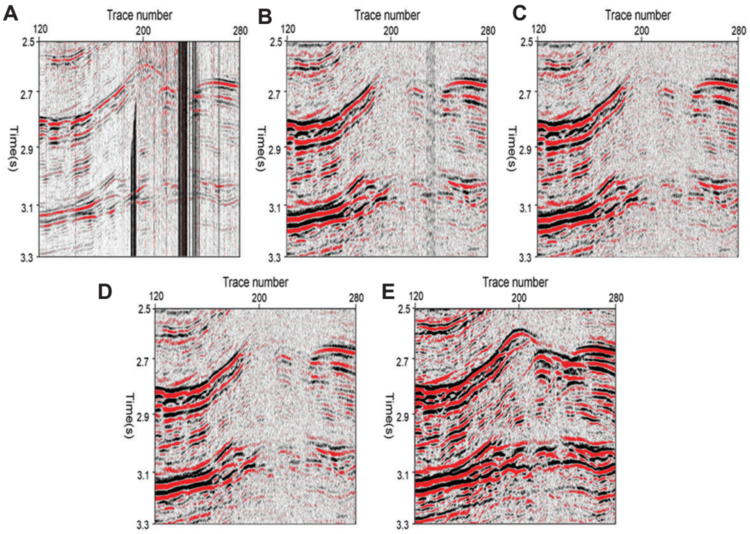

Figure 14. Stacked sections comparing raw data, traditional method results, and the proposed method for Block A. (A) Stack of raw data. (B) Stack of shearlet-denoised data. (C) Stack of deep learning-denoised data. (D) Stack of dictionary learning-denoised data. (E) Stack of proposed method-denoised data.

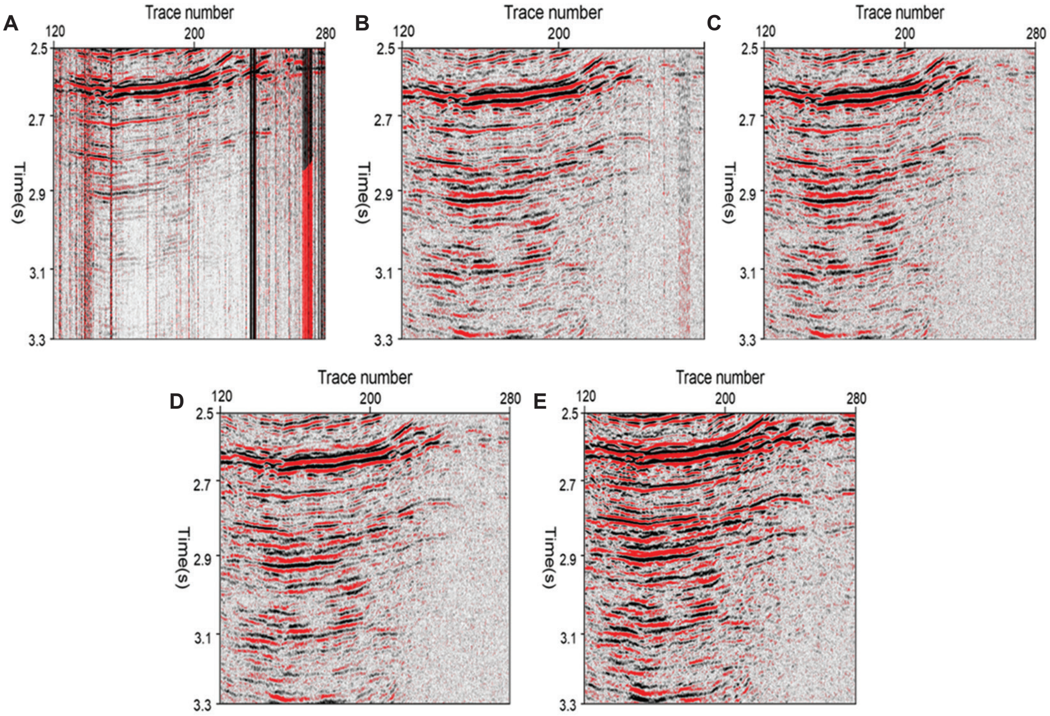

Figure 15. Stacked sections comparing raw data, traditional method, and the proposed method for Block B. (A) Stack of raw data. (B) Stack of shearlet-denoised data. (C) Stack of deep learning-denoised data. (D) Stack of dictionary learning-denoised data. (E) Stack of proposed method-denoised data.

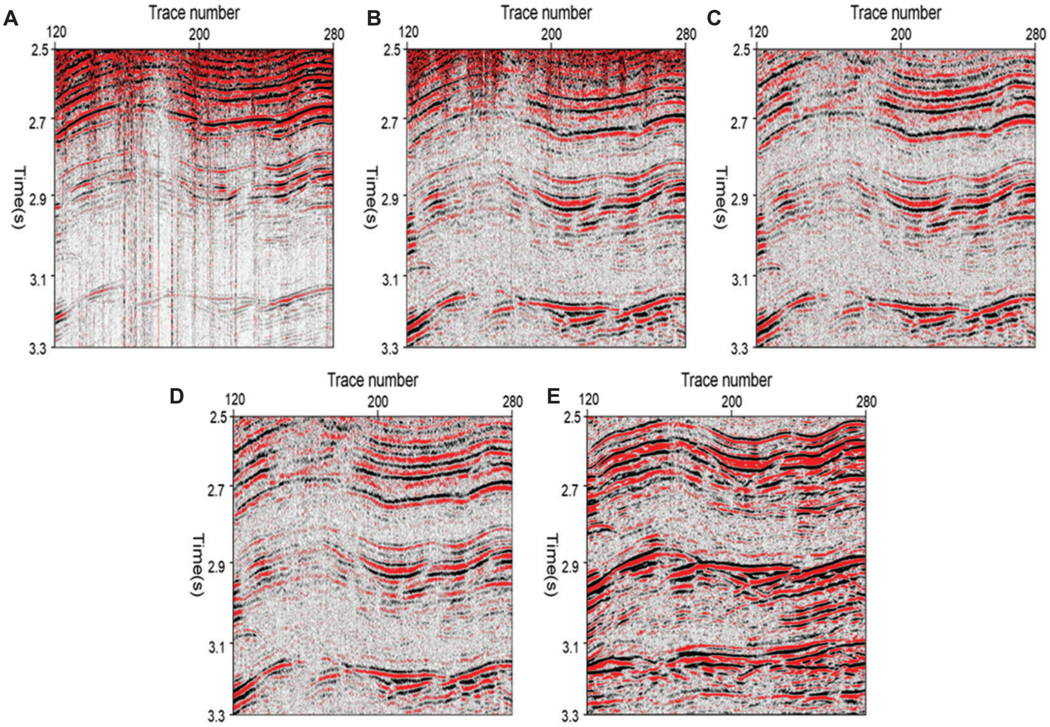

Figure 16. Stacked sections comparing raw data, traditional method, and the proposed method for Block C. (A) Stack of raw data. (B) Stack of shearlet-denoised data. (C) Stack of deep learning-denoised data. (D) Stack of dictionary learning-denoised data. (E) Stack of proposed method-denoised data.

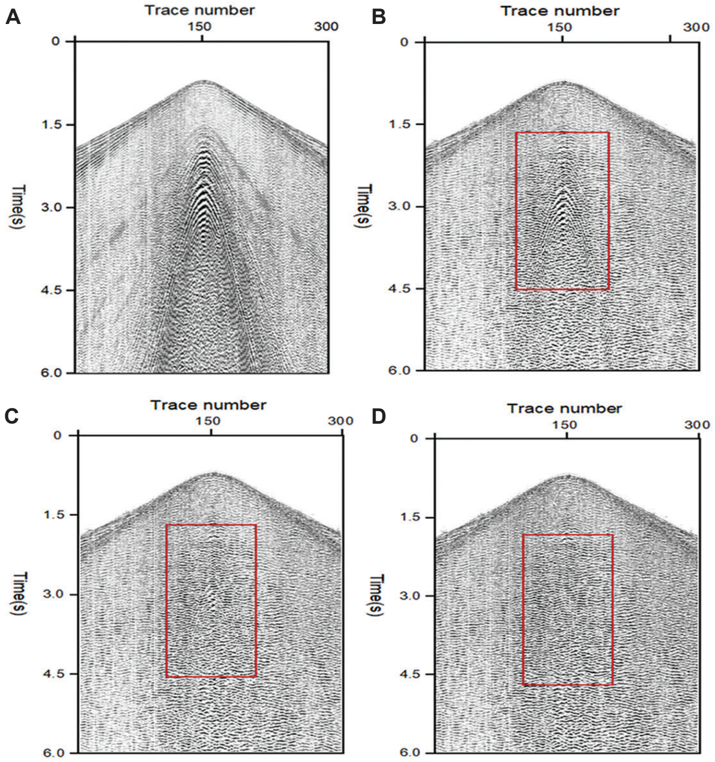

Figure 17. Raw data and denoised results. (A) Raw data. (B) Result using deep learning. (C) Result using conventional industrial workflow. (D) Result using the proposed method.

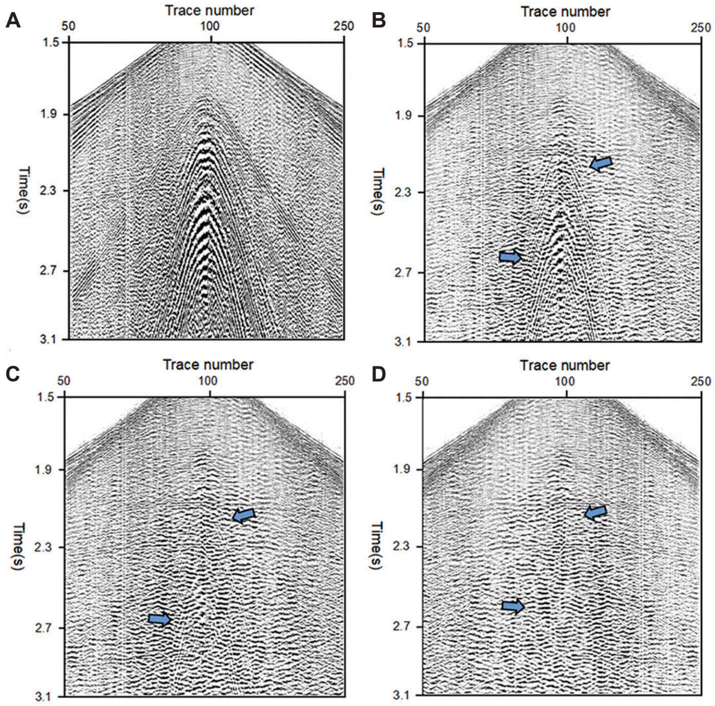

Figure 18. Partial enlarged image of raw data and denoised data. (A) Raw data. (B) Result using deep learning. (C) Result using conventional industrial workflow. (D) Result using the proposed method.

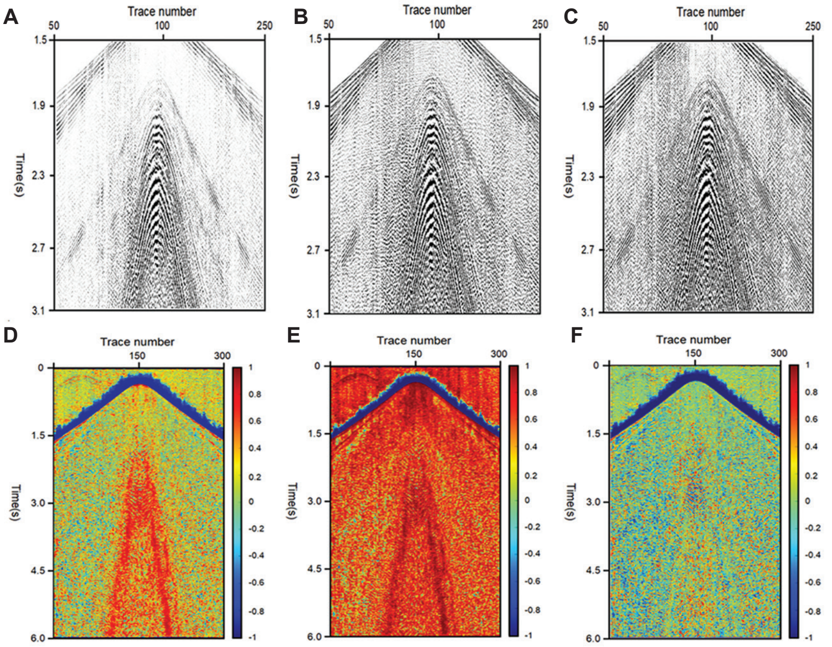

Figure 19. Removed noise and local coherence analysis. (A) Removed noise using deep learning. (B) Removed noise using a conventional industrial workflow. (C) Removed noise using the proposed method. (D) Local coherence between the removed noise and the denoised result using deep learning. (E) Local coherence between the removed noise and the denoised result using a conventional industrial workflow. (F) Local coherence between the removed noise and the denoised result using the proposed method and raw data.

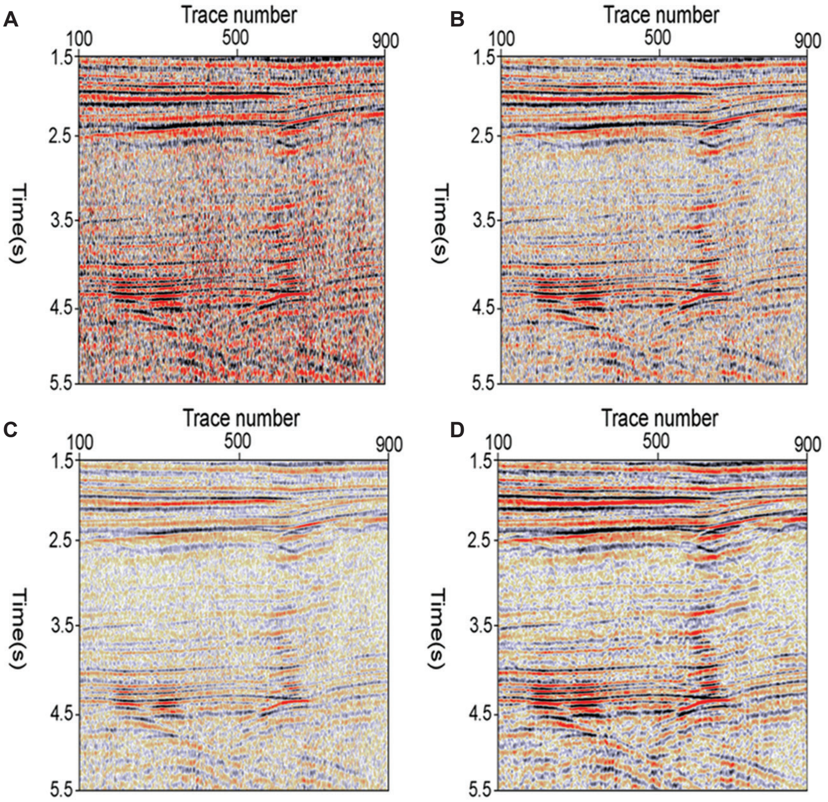

Figure 20. Stacked sections of raw data and denoised data in Region A. (A) Raw data. (B) Result using deep learning. (C) Result using conventional industrial workflow. (D) Result using the proposed method.

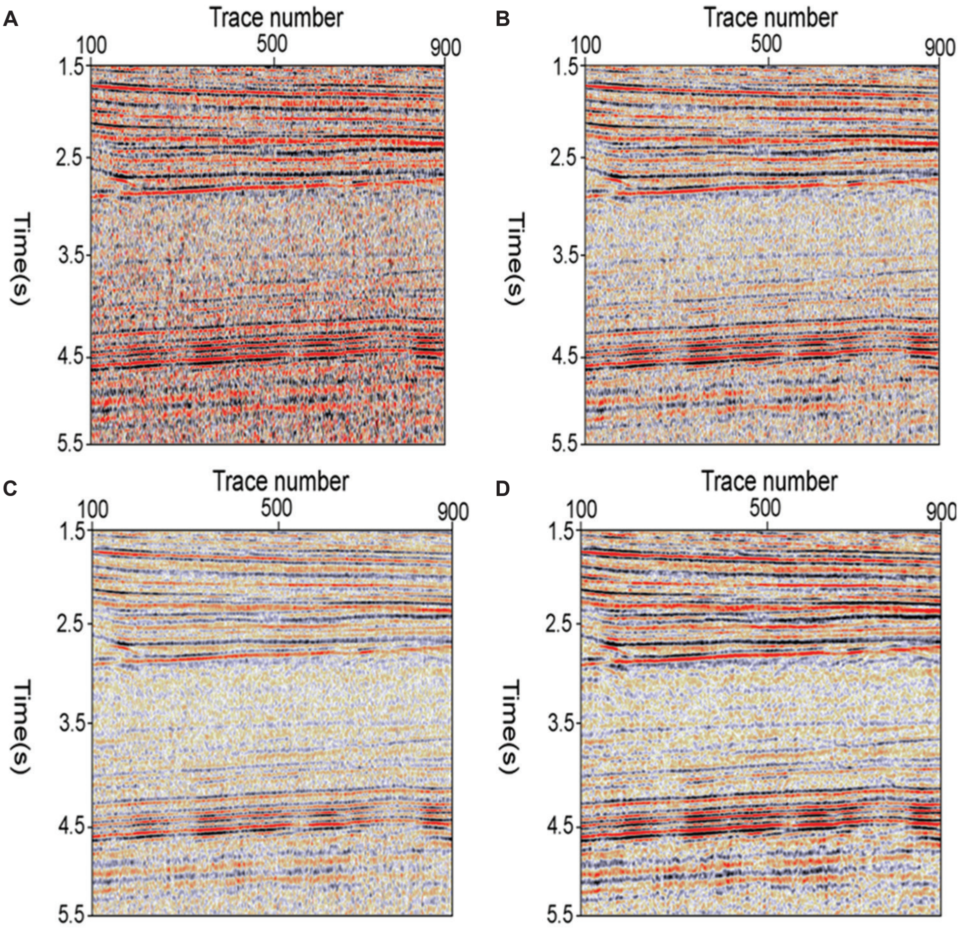

Figure 21. Stacked section of raw data and denoised data in Region B. (A) Raw data. (B) Result using deep learning. (C) Result using conventional industrial workflow. (D) Result using the proposed method.

section from the raw data (Figure 20A) suffers from low SNR and poor reflector continuity. While the results from deep learning (Figure 20B) and the conventional industrial workflow (Figure 20C) offer improvements, the result from the proposed method (Figure 20D) demonstrates the most significant enhancement, with clearer, more continuous reflectors and more prominent structural features such as faults and pinch-outs. A similar conclusion is drawn from the stacked results for Region B, presented in Figure 21. Compared to the raw data stack (Figure 21A) and the results from both deep learning (Figure 21B) and the conventional industrial workflow (Figure 21C), the proposed method's result (Figure 21D) again exhibits substantial improvement. In both regions, our method effectively recovered weak signals previously masked by strong noise, confirming its superior capability and practical value.

4. Discussion

The physics-constrained sparse basis learning approach for seismic data processing holds significant potential for future research. Future research will focus on exploring more advanced methods of incorporating physical attributes, such as geological models, velocity fields, or wavefield propagation theories. These additions could further enhance the recognition and preservation of valid seismic signals. Another promising direction involves integrating the powerful feature extraction capabilities of DL with the theoretical strengths of sparse representation. Hybrid models that combine these elements could lead to more efficient and higher-fidelity adaptive seismic data processing while maintaining physical interpretability.

5. Conclusion

In this study, we proposed a physics-constrained sparse basis learning method to address the critical challenge of suppressing complex, mixed noise in seismic data without damaging effective signals. The primary advantage of our method lies in the integration of local dip information, derived from a PWD filter, as a physical constraint within the dictionary learning framework. This innovation effectively overcomes a key limitation of traditional data-driven approaches by preventing the learned basis from incorporating non-physical, noise-like features, thereby ensuring high-fidelity signal preservation. Our extensive experiments on both synthetic and real data demonstrated that this approach provides superior suppression of mixed noise—including anomalous amplitudes, ground roll, random, and coherent noise—compared to conventional techniques and other learning-based techniques. Ultimately, the enhanced clarity and continuity of reflectors in the final seismic images confirm the practical value of our method for improving the delineation of geological structures and recovering weak signals.

Acknowledgments

None.

Funding

This work was supported by the China National Petroleum Corporation Science and Technology Special Project “Research on Risk Exploration Targets and Engineering Technology Breakthroughs in the Qaidam Basin, Including Field Trials” (2023YQX10108).

Conflict of interest

Huailiang Li is an Editorial Board Member of this journal but was not in any way involved in the editorial and peer-review process conducted for this paper, directly or indirectly. The authors declare that they have no competing interests.

Author contributions

Conceptualization: Deying Wang, Huailiang Li
Formal analysis: Huailiang Li, Longjiang Kou
Funding acquisition: Yongsheng Wang
Investigation: Kai Zhang, Wenqing Liu
Methodology: Deying Wang, Longjiang Kou
Validation: Yongsheng Wang
Writing–original draft: Deying Wang, Huailiang Li
Writing–review & editing: Kai Zhang, Wenqing Liu

Availability of data

The data presented in this study are available from the corresponding author upon reasonable request.

References

1. Zhang H, Chen, X, Li H, *et al*. 3D seismic data denoising approach based on curvelet transform. *Oil Geophys Prospect.* 2017;52(2):226-232.
2. Liu Y, Fomel S, Liu C, Wang D, Liu G, Feng X. High-order seislet transform and its application of random noise attenuation. *Chin J Geophys.* 2009;52(8):2142-2151.

   doi: 10.3969/j.issn.0001-5733.2009.08.024
3. Zhang H, Chen X, Yang H. Optimistic wavelet basis selection in seismic signal noise elimination. *Oil Geophys Prospect.* 2011;46(1):70-75.
4. Wrinch D, Jeffreys H. On certain fundamental principles of scientific inquiry. *Philos Mag.* 1921;42(250):369-390.

   doi: 10.1080/14786442108633773
5. Häuser M, Ma J. Interpolating seismic data via the POCS method based on shearlet transform. *J Geophys Eng.* 2012;9(3):852-861.
6. Herrmann FJ. Curvelet-based seismic data processing: A multiscale and nonlinear approach. *Geophysics*. 2006;71(4):E11-E25.
7. Herrmann FJ, Hennenfent G, Moghaddam PP. Compressive seismic data acquisition: An overview. *Geophysics*. 2008;73(1):R23-R33.
8. Huang X. A simulation of acquisition design and data processing for offshore compressive sensing seismic. *Oil Geophys Prospect.* 2020;55(2):248-256.
9. Starck JL, Candès EJ, Donoho DL. The curvelet transform for image denoising. *IEEE Trans Image Process.* 2002;11(6):670-684.

   doi: 10.1109/tip.2002.1014998
10. Aharon M, Elad M, Bruckstein A. K-SVD: An algorithm for designing overcomplete dictionaries for sparse representation. *IEEE Trans Signal Process.* 2006;54(11):4311-4322.

    doi: 10.1109/TSP.2006.881199
11. Engan K, Aase SO, Husoy JH. Frame Based Signal Compression using Method of Optimal Directions (MOD). In: *1999 IEEE International Symposium on Circuits and Systems, ISCAS'99*. Vol. 4. United States: IEEE; 1999. p. 244-247.

    doi: 10.1109/ISCAS.1999.779928
12. Liu L, Liu Y, Liu C, Zheng Z. Iterative seismic random noise suppression method based on compressive sensing. *Chin J Geophys.* 2021;64(12):4629-4643.

    doi: 10.6038/cjg2021P0045
13. Zhang K, Zuo W, Chen Y, Meng D, Lei L. Beyond a Gaussian denoiser: Residual learning of deep CNN for image denoising. *IEEE Trans Image Process.* 2017; 26(7):3142-3155.

    doi: 10.1109/TIP.2017.2662206
14. Kaur R, Waldeland AU, Alaei R, Solberg AHS. Self-supervised learning for seismic denoising. *IEEE Trans Geosci Remote Sens.* 2022;60:1-12.

15. Song C, Alkhalifah T, Riyanti F. A physics-informed deep learning approach for denoising seismic data. *Geophysics*. 2022;87(5):V239-V250.

16. Sacchi MD, Ulrych TJ, Walker CJ. Interpolation and extrapolation using a high-resolution discrete Fourier transform. *IEEE Trans Signal Process*. 1998;46(1):31-38.

doi: 10.1109/78.651165

17. Yao Z, Sun C, Li H, Yang A. Time-variant wavelet extraction and seismic reflectivity inversion based on basis pursuit. *Oil Geophys Prospect*. 2019;54(1):137-144.

18. Candès EJ, Donoho DL. Curvelets-a new multiresolution representation for visual information. In: *Wavelet Applications in Signal and Image Processing VIII*. Vol. 4119. United States: SPIE; 2000. p. 248-262.

19. Chen Y, Ma J, Fomel S. Seismic noise attenuation using a deep-learning approach with a local-correlation-based structural constraint. *IEEE Trans Geosci Remote Sens*. 2020;58(7):4668-4679.

20. Zhang L, AlRegib G. SSIM-based quality control for seismic processing. *Geophysics*. 2021;86(3):V235-V248.

21. Amini H, Javaherian A. A review of seismic attributes. *J Appl Geophys*. 2022;205:104764.

ACCSCIENCE PUBLISHING

Journal of Seismic Exploration

ARTICLE

A novel wavefield reconstruction inversion method using an approximated model-domain Hessian

Huaishan Liu[1,2,3], **Yuzhao Lin**[3*], **Lei Xing**[3], **Jinghao Li**[3], **Kun Huang**[3] **and Hehao Tang**[3]

[1]State Key Laboratory of Shale Oil and Gas Enrichment Mechanisms and Efficient Development, Beijing, China

[2]Key Laboratory of Oil & Gas Reservoir Geophysics, Sinopec, Beijing, China

[3]Department of Marine Geophysics, College of Marine Geosciences, Ocean University of China, Qingdao, Shandong, China

***Corresponding author:** Yuzhao Lin (linyuzhao@ouc.edu.cn)

Citation: Liu H, Lin Y, Xing L, Li J, Huang K, Tang H. A novel wavefield reconstruction inversion method using an approximated model-domain Hessian. *J Seismic Explor*. 2025;34(4):60-69. doi: 10.36922/JSE025250018

Received: June 16, 2025

Revised: August 15, 2025

Accepted: September 3, 2025

Abstract

The Hessian matrix, though computationally expensive, plays a critical role in ensuring inversion accuracy and mitigating cross-talk in multi-parameter inversion. The well-known wavefield reconstruction inversion (WRI) or extended space full-waveform inversion can reduce nonlinearity and mitigate cycle skipping in traditional FWI. However, most implementations omit the Hessian. In this study, the Hessian—formulated as a function of measurement and theoretical covariance matrices—is incorporated into WRI within a Bayesian inference framework. Furthermore, the connections between the data- and model-domain Hessian equations are discussed, leading to a simplified calculation method for the extended source. Based on this approach, a new definition for the theoretical covariance matrix is proposed and validated through numerical tests, demonstrating its accuracy.

Keywords: Inversion; Bayesian inference; Theory covariance matrix

1. Introduction

Full-waveform inversion (FWI),[1,2] a tool commonly used to invert subsurface structures, has been widely used in geophysics exploration.[3,4] However, as a data-fitting algorithm in the least squares sense, FWI suffers from cycle skipping and nonlinearity, primarily due to the difficulty of predicting the data resulting from the inexpressive wave equation and the limited acquisition aperture.[5]

There are methods specifically designed to address cycle skipping, which generally involves a complex operation for each trace[6,7] or shot[8] to achieve accurate matching. An advanced method for measuring distance using optimal transport distances has garnered the attention of a wide range of researchers and has been well-developed.[9-12] As for nonlinearity, the multi-scale strategy,[12,13] changing the inversion domain,[14] or modifying the objective function form[15] can help alleviate this limitation.

In addition to the above methods, two other directions have been proposed and developed into relatively mature methods. One is an extended space FWI (ES-FWI), which introduces another search space in the inversion.

There are two ways to build the ES-FWI method. The first approach is to add non-physical degrees of freedom to the model, thereby pushing the synthetic data to better fit the observed data.[16] However, new space introduces additional computational costs through either increased calculation time for the new forward operator or more storage requirements for new variables. Various methods have been proposed to reduce computational cost,[17,18] in which the extended source FWI[19] is a more efficient method, as it only inverts the extended source and the model parameters. A study by Symes[20] provided a detailed analysis of why the extended source FWI is effective.

The other method is the wavefield reconstruction inversion (WRI), which starts by incorporating the wave equation into the objective function to reduce nonlinearity and computational cost.[21] Leeuwen and Herrmann[22] conducted a more mathematical analysis of the proposed method and carefully analyzed the selection strategy of the penalty scalar.[22] However, it was initially proposed in the frequency domain, requiring an augmented wave equation that is challenging to solve in the time domain. In addition, the physical meaning of certain variables (reconstructed wavefield, penalty scalar) and the tuning method for the penalty scalar when solving WRI require clarification.

Several studies have been conducted to address the above challenge, including rough approximations that enable WRI in the time domain,[23,24] resulting in more precise solutions proposed. Rizzuti *et al.*[25] proposed a data-dual formulation of WRI, where the Lagrange formula is used to reformulate the WRI, making it easier to apply to large three-dimensional models in the time domain.[25,26] Moreover, the iterative refining-WRI method was proposed, in which an enhanced Lagrange method equipped with operator splitting is used instead of the penalty method, with its regularization and corresponding expansion in other media investigated accordingly.[27-29] For the adjustment of the penalty scalar, a rough local optimization method was used.[30] Gholami *et al.*[31] treated the penalty scalar as a variable that needs to be inverted. In addition, Gholami *et al.*[32] discussed the physical meaning of the reconstructed wavefield, while Lin *et al.*[33] elucidated the mechanism of low-wavenumber update in WRI.

In general, although both extended FWI and WRI are essentially ES-FWI, there are apparent differences between them. Extended FWI expands space by introducing seismic-related variables (e.g., offset, wavelet) into model space, while WRI uses model space in the sense of the wavefield. Extended FWI utilizes the introduced space or variables to achieve an accurate data fit, while WRI reduces the impact of non-linearity and non-physical data through wavefield matching. However, both methods require delicate settings of the inversion parameters. Operto *et al.*[34] reviewed the above ES-FWI methods within the framework of inverse scattering theory, in which the Lippmann–Schwinger equation was used to govern modeling.[34] In addition to ES-FWI, the Hessian is typically used to ensure inversion accuracy in traditional FWI. However, computing the Hessian remains challenging due to its large scale. Furthermore, the Hessian is commonly not included in WRI or ES-FWI.

In this paper, we analyze these inversion methods using the Bayesian inference theory. Notably, all inversion methods can be formulated uniformly using Bayesian inference theory, which can bring substantial advantages.[3,35] First, deriving inversion methods from Bayesian inference can provide a more accurate representation of the problem. Figueiredo *et al.*[36] and Huang *et al.*[37] used the Bayesian theory to develop a more precise inversion method for an anisotropic medium.[36,37] Furthermore, a reduced non-linear inversion can be obtained. Moreover, Leeuwen[38] and Lin *et al.*[39] re-derived WRI from Bayesian inference and accelerated the inversion by redefining the theoretical covariance matrix.[38,39]

The main contribution of this paper is a simplified theoretical definition of the covariance matrix to alleviate the computational problem of WRI. This paper is organized as follows: first, the WRI is re-derived from Bayesian inference to illustrate how the statistical variables included in the model or data domain Hessian affect or improve the inversion methods. Next, by comparing the data and model domain methods, we provide a simplified extended source calculation method. Finally, corresponding numerical tests are shown to demonstrate the effectiveness of different theoretical covariance matrix definitions.

2. Theory

2.1. Seismic inversion based on Bayesian inference

Various ES-FWI methods have been developed for different concerns. In this section, we derive the original WRI from Bayesian inference, in which the Hessian is naturally introduced. First, the wavefield term u is introduced into the Bayesian inference (**Equation I**):[39]

$$\rho_{post}\left(u, m|d\right) \propto \rho_{like}\left(d|m, u\right) \rho_{prior}\left(u, m\right) \tag{I}$$

Where the likelihood of probability density function is:

$$\rho_{like}\left(d|m,u\right) = \quad exp - \frac{1}{2}(d-Pu)^* \Sigma_{obs}^{-1}(d-Pu) + \\ exp - \frac{1}{2}(q-Au)^* \Sigma_{syn}^{-1}(q-Au) \tag{II}$$

in which m denotes the interested model parameters, d represents the observed data, P is the sampling operator, u denotes the seismic source, A is the forward operator, and Σ_{obs}, Σ_{syn} are the measurement and theoretical covariance matrices, respectively (**Equation II**). ρ_{prior} denotes the prior knowledge of the wavefield and model parameters, which will be excluded in this paper to simplify the calculation. Maximizing the posterior leads to the following minimization problem:

$$\phi(m,u) = (d-Pu)^* \Sigma_{obs}^{-1}(d-Pu) + \\ (q-A(m)u)^* \Sigma_{syn}^{-1}(q-A(m)u \tag{III}$$

There are two ways to solve **Equation III**, which will be discussed in the following section.

2.2. WRI based on the data-domain Hessian

We assumed the measurement uncertainty is random, and the measurement covariance matrix is $\Sigma_{obs}^{-1} = \lambda_{obs} I$. Then, by keeping the model m fixed and setting the derivative of **Equation III** with respect to the wavefield to zero, we obtain **Equation IV**:

$$A\hat{u} = q + \lambda_{obs} \Sigma_{syn} A^{-*} P^* \delta d \tag{IV}$$

Where $\delta d = d - P\hat{u}$ and $\hat{u}$ denotes the reconstructed wavefield. The reconstructed wavefield on both sides makes the above equation challenging to solve, and moving the reconstructed wavefield to one side is difficult to perform due to the complex combination of the forward operators. Approximate or alternative measurements have been proposed by Lin *et al.*[12] to address these challenges.[12] Essentially, the above equation involves the data-domain Hessian, where δd can be solved by **Equation V**:

$$H_d \, \delta d = \delta d^0 \tag{V}$$

where $\delta d^0 = d - Pu$, u is the background or current wavefield, and

$$H_d = \lambda_{obs} (PA^{-1}) \Sigma_{syn} (PA^{-1})^* + I \tag{VI}$$

as in Gholami *et al.*[40] (**Equation VI**).

With the reconstructed wavefield, $\hat{u}$ we can obtain an update for the model parameters by calculating the derivative of the objective function with respect to the model, and replacing the latter term according to **Equation IV**, we have **Equation VII**:

$$g = -(\frac{\partial A\hat{u}}{\partial m})^* \Sigma_{syn}^{-1}(A\hat{u} - q) = -\lambda_{obs} (\frac{\partial A\hat{u}}{\partial m})^* A^{-*} P^* \delta d \tag{VII}$$

The gradient is a zero-lag correlation between the reconstructed wavefield and the back-propagated residual blurred by the data-domain Hessian with the theoretical covariance matrix. The calculation of the data-domain Hessian is computationally infeasible due to its large scale. Lin *et al.*[39] proposed a point spread function-based method to alleviate this challenge. Furthermore, a proper theoretical covariance matrix definition has been proven to be another way to mitigate the computational problem.[39]

2.3. WRI based on the model-domain Hessian

Clearly, the data-domain Hessian is challenging to compute; however, it remains essential for achieving accurate WRI. An alternative is to reformulate the problem in a different domain. By starting with the data-domain Hessian and the weighted residual in WRI and FWRI, and multiplying $(PA^{-1})^*$ on both sides of **Equation V**, we transform it into the model-domain equation (**Equation VIII**):

$$[\lambda_{obs} (PA^{-1})^* (PA^{-1}) \Sigma_{syn} + I]\hat{s} = s_0 \tag{VIII}$$

where $\hat{s} = (PA^{-1})^* \delta d, s_0 = \lambda_{obs} (PA^{-1})^* \delta d^0$, similar to the adjoint state definitions.[41] In this case, instead of inverting the data-domain Hessian, we consider the inversion of the model-domain Hessian (**Equation IX**):

$$H_m = \lambda_{obs} (PA^{-1})^* (PA^{-1}) \Sigma_{syn} + I \tag{IX}$$

In this case, the wavefield reconstruction process becomes Equation X:

$$A\hat{u} = q + \lambda_{obs} \Sigma_{syn}^{-1} \hat{s} \tag{X}$$

The transformation significantly alleviates the computation memory problem, and the model gradient can be simplified into a straightforward form (**Equation XI**):

$$g = (\frac{\partial A}{\partial m})^* \hat{u}(q, \hat{s})^* \hat{s} \tag{XI}$$

Next, we can divide the gradient into two terms by separating the wavefields excited by different sources q (d $\hat{s}$). The first term (**Equation XII**):

$$g_1 = (\frac{\partial A}{\partial m})^* \hat{u}_0(q)^* \hat{s} \tag{XII}$$

Which is also the traditional FWI gradient, except for the blurred residual. The second term is (**Equation XIII**):

$$g_2 = \left(\frac{\partial A}{\partial m}\right)^* \hat{u}(\hat{s})^* \hat{s} \tag{XIII}$$

The above two terms are identical to the FWRI gradients developed in Lin *et al.*,[33] and its original **Equation XI** is directly derived from WRI, similar to the source extended FWI except for the source or data differences.

By comparison, we can see that the only difference between the data-domain and model-domain solutions is the extended source calculation, and the gradient calculation can be made through **Equations XII** and **XIII**.

2.4. The comparison between the two Hessian matrices

Here we write the two Hessian-based equations as follows (Equations XIV & XV):

$$[\lambda_{obs}(PA^{-1})\Sigma_{syn}(PA^{-1})^* + I]\delta d = \delta d^0 \tag{XIV}$$

$$[\lambda_{obs}(PA^{-1})^*(PA^{-1})\Sigma_{syn} + I]\hat{s} = s^0 \tag{XV}$$

Both equations are challenging to solve: **Equation XIV** involves a largeale matrix inverse calculation for the data residual, and **Equation IV** needs to operaten each wavefield or the extended source at each time step or frequency slice. A source-based definition of the theoretical covariance matrix has been proposed to alleviate the data-domain computation problem. Similarly, a proper definition of the theoretical covariance matrix should simplify the model-domain calculation problem.

Assuming the determinant of the first part of the model domain Hessian is significantly larger than the identity matrix, and all variables can be inverted, we have an approximated extended source expression (**Equation XVI**):

$$\hat{s} \approx \lambda_{obs}^{-1}\Sigma_{syn}^{-1}AP^{-1}P^{-*}A^*s^0 \tag{XVI}$$

Substituting the s^0 definition into **Equation XVI**, we have **Equation XVII**:

$$\hat{s} = \lambda_{obs}^{-1}\Sigma_{syn}^{-1}AP^{-1}P^{-*}A^*A^{-*}P^*\delta d^0 = \lambda_{obs}^{-1}\Sigma_{syn}^{-1}AP^{-1}\delta d^0 \tag{XVII}$$

Notably, the derivation of the above equations relies on rough approximations and extreme assumptions. For the first part, the value of the first term of the Hessian, which is larger than the identity matrix, can be easily satisfied since it is a diagonal domain matrix and can be scaled by the theoretical matrix. We selected an exponential function, which can ensure this assumption. As for the second assumption, it essentially used the inverse of two operators. One is the forward operator *A*, which is commonly used in inversion and imaging methods and applicable in the frequency codes. The other is the sampling operator *P*, which is mathematically incorrect to approximate the inverse of the adjoint $P^{-1} = P^*$.

However, the sampling operator is a dimensionality reduction operator that reduces the whole model space data to the receiver points, which is inevitable in seismic exploration. Therefore, one can only hope that the reduced data can recover the wavefield in the whole model space through the forward operator. In other words, the approximation of the sampling operator is mathematically incorrect but physically applicable. Although **Equation XVII** is similar to the extended source **Equation XI** in Huang *et al.*,[18] the specific calculation is different: The SE-FWI method is a more accurate solution that requires additional calculation and storage of the Green function, while the proposed method in this paper is based on an approximation that only requires one additional partial differential equation (PDE) solver. In general, the extended source can be considered an operator on the receiver residual, where the operator is a function of the theoretical covariance matrix and the forward operator. The overall operator may help us to define the theoretical covariance matrix (**Equation XVIII**):

$$\hat{\Sigma}_{syn} = \Sigma_{syn}^{-1}A = \Sigma_{syn}^{-1}\left(m\frac{\partial^2}{\partial t^2} - L\right) \tag{XVIII}$$

Where L is the Laplacian operator, the above equation reduces to a function in the receiver size due to the invertible assumption of the sampling operator *P*. Furthermore, the model-domain Hessian operates on each wavefield, while the original data comes from the source or receiver locations.

In general, through a series of approximations, assumptions, and derivations, we provide a straightforward method to define the theoretical covariance matrix, which ensures an accurate inversion with an affordable computational cost (**Equation XIX**):

$$\hat{\Sigma}_{syn} = \Sigma_{syn}^{-1}(x_r, x_r)\left[m(x_r)\frac{\partial^2}{\partial t^2} - L(x_r)\right] \tag{XIX}$$

where x_r denotes the receiver locations.

Next, various theoretical covariance matrix definitions were given according to the inversion problem. Notably, through the above derivation, the calculation of the extended source was made simpler and more cost-effective (**Equation XX**), which is a simple operation for the original data residual at the receiver location.

$$\hat{s}\left(x_r,t\right)=\lambda_{obs}^{-1}\Sigma_{syn}^{-1}\left(x_r,x_r\right)\left[m\left(x_r\right)\frac{\partial^2}{\partial t^2}-L\left(x_r\right)\right]\delta d^{0}\left(x_r,t\right) \qquad \text{(XX)}$$

Various theoretical covariance matrix definitions are given and discussed in the following numerical test section. This part is only used for the wavefield reconstruction; the model gradient is calculated using **Equation VII**.

3. Numerical tests

3.1. Inversion test with smoothed initial model

In this section, we applied the proposed method to the classical Marmousi model. The size of the Marmousi model in Figure 1 is 250 × 767 with a 10 m space interval in each direction. A Ricker wavelet with 8 Hz central frequency with 2 Hz cutoff was used to simulate data in Figure 2. The recorded time was 3 s with a sampling of 1 ms. A total of 30 shots with 200 m intervals were set at a depth of 10 m beginning at 340 m, and the receivers were evenly distributed at a depth of 10 m at every grid point. The smoothed initial model is shown in Figure 3, which can be obtained by tomography or velocity analysis.

First, we presented the extended source used in WRI in Figure 4, where Figure 4A is the classical data residual used in the traditional WRI, and Figure 4B is the extended source calculated by **Equation XX**. We can see that the derived extended source exhibited a wider wavelength, making the misfit easier.

The final inversion results are shown in Figure 5, where Figure 5A is the traditional FWI result, Figure 5B plots the traditional WRI result, and Figure 5C is the WRI result based on the extended source (WRI-I). Due to the severely smoothed initial model, the traditional FWI failed to recover part of the key structures, especially in the deep parts. By comparison, the classical WRI provided a relatively accurate inversion result, where all structures were accurately located and inverted with limited artifacts. The WRI-I provided an accurate inversion result, where all the structures are recovered (especially the middle complex part) with fewer artifacts. Moreover, the computational cost of the new WRI is cheaper than that of the classical WRI. Both WRI results provided a more accurate inversion result at the deep part. For a clearer comparison, we extracted two traces from the true velocity and inversion results (Figure 6).

3.2. Inversion test with linear initial model

The basic parameters for the modeling and inversion were the same, except for the initial model, which is linear in Figure 7, causing more nonlinearity for the inversion. Furthermore, unlike other inversion tests, the initial

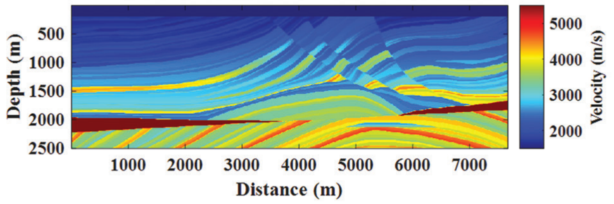

Figure 1. The Marmousi model

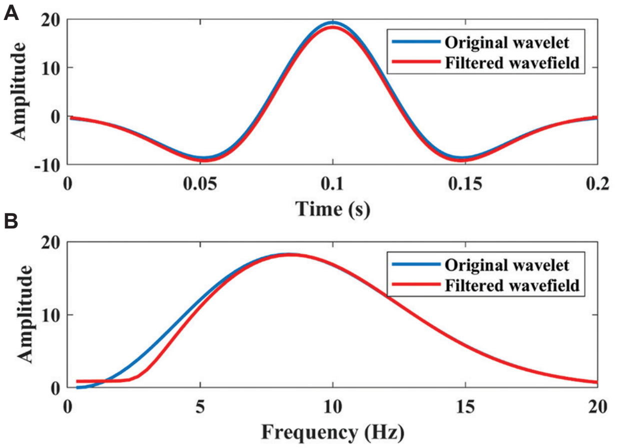

Figure 2. (A and B) Wavelet used for modeling and inversion

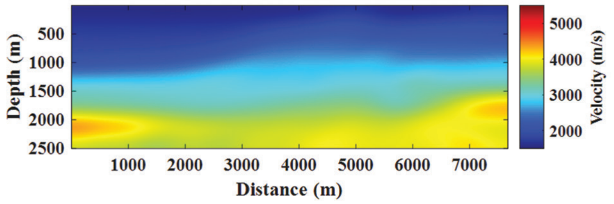

Figure 3. The smoothed Marmousi model

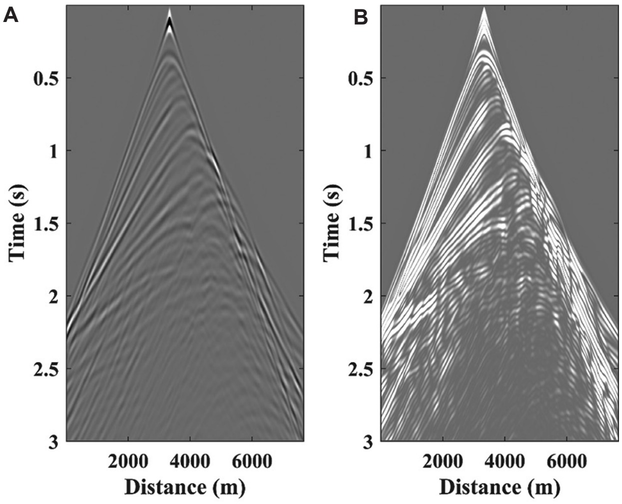

Figure 4. Extended source comparison between (A) the data resource calculated based on the identity matrix definition, and (B) the extended source calculated by **Equation XX**

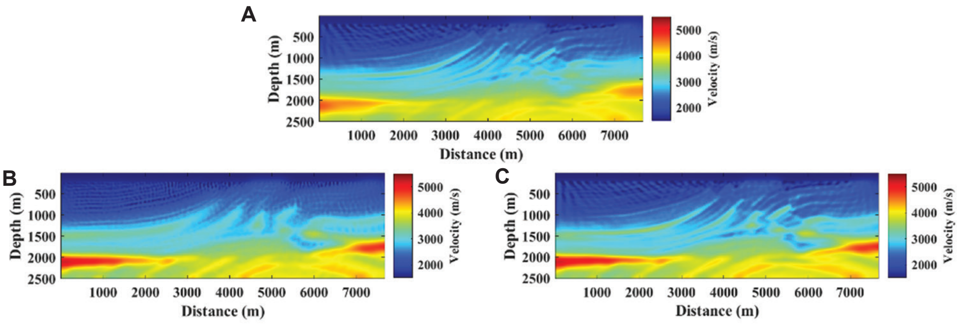

Figure 5. Inversion results. (A) Traditional full-waveform inversion result, (B) traditional wavefield reconstruction inversion (WRI) result, and (C) WRI result based on extended source.

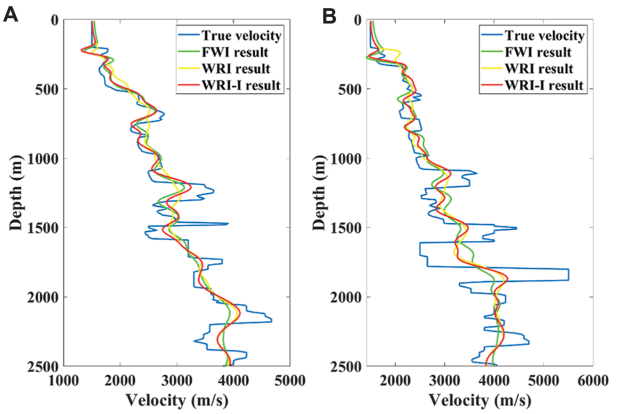

Figure 6. Comparison of vertical velocity profiles at different depths. (A) x = 3,800 m and (B) x = 6,500 m.
Abbreviations: FWI: Full-waveform inversion; WRI: Wavefield reconstruction inversion.

model was significantly different from the true velocity, particularly in the deeper region. Therefore, we provided a new theoretical covariance matrix definition to aid the inversion (**Equation XXI**):

$$\sum_{syn} = exp^{-g(r)} \tag{XXI}$$

Where g is a manually picked function, and r denotes the distance between an arbitrary point and the source location: $g(r) = 1/r$. This equation is essentially an exponential function to emphasize the source distance, which is a known and relatively clear variable that can be used as an additional quantity for assistance in extended FWI or WRI.

Naturally, the extended sources used in WRI are shown in Figure 8, where Figure 8A is the classical data residual used in the traditional WRI, Figure 8B is the extended source calculated by **Equation XX**, and Figure 8C is the extended source calculated by **Equation XXI**. We can see that the data residual calculated by the newly defined theoretical covariance matrix is more structured at the waveform edges, and the deep reflections are more significant.

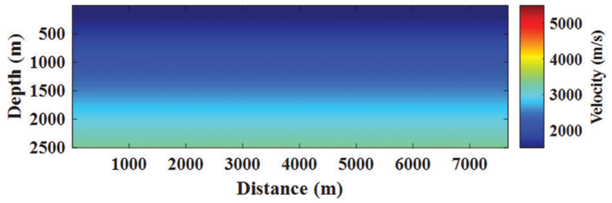

Figure 7. Linear initial model

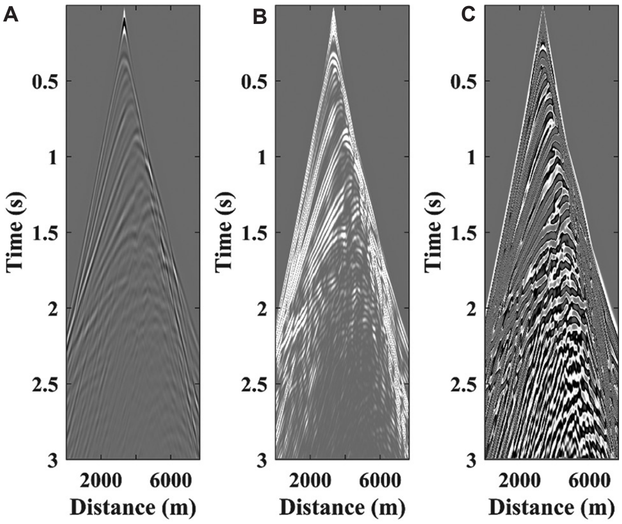

Figure 8. Extended source comparison. (A) Identity matrix definition, (B) calculated by **Equation XX**, and (C) calculated by **Equation XXI**.

Due to the strong non-linearity caused by the initial model, the traditional FWI failed to perform an effective inversion and still showed no sign of convergence at the 50th iteration. The result (Figure 9A) contained many artifacts and was different from the true model. However, the traditional WRI (Figure 9B) produced an accurate inversion result, but with stronger artifacts that contaminated the shallow layers. Figure 9C plots the WRI-I,

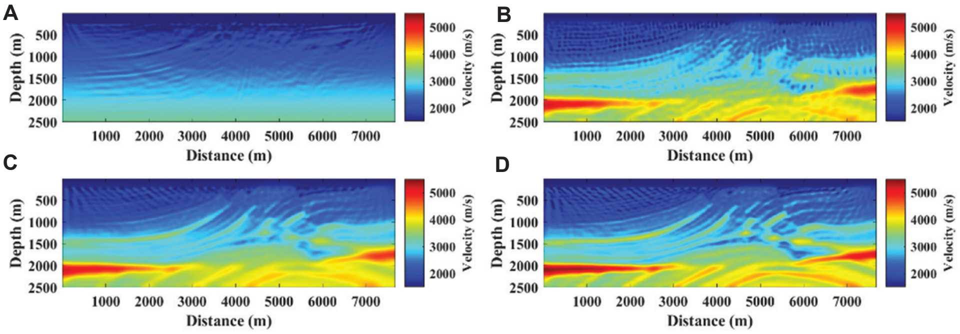

Figure 9. Inversion results. (A) Traditional FWI result, (B) traditional WRI result, (C) WRI result based on the extended source, and (D) WRI result based on the defined extended source.
Abbreviations: FWI: Full-waveform inversion; WRI: Wavefield reconstruction inversion.

and Figure 9D is the WRI-I calculated by **Equation XXI.** Both WRI methods based on the extended source yielded accurate inversion results. Meanwhile, the traditional one, that is, WRI-I, was still unable to obtain an accurate model in the middle. Furthermore, with a carefully defined theoretical covariance matrix, the WRI-I calculated by **Equation XXI** provided a very accurate inversion result that is very close to the true model without any evident artifacts. A curve comparison (Figure 10) is also provided to support the above claims.

Furthermore, a noisy test was conducted to highlight the robustness of the proposed method with respect to noise and to clarify the determination of the measurement constant. Figure 11 is the extended source used in WRI. An identity measurement covariance matrix can be used to describe random noise. Considering the role of the measurement constant λ_{obs} in the extended source equation and gradient formula, a subjectively determined constant that preserves modeling stability is sufficient, as was done in the previous tests. In the noise test, the constant was the same as the signal-to-noise ratio, which is estimated using the amplitude spectrum method.

As for the final inversion results (Figure 12), we observed that the noise in the extended source was entirely random and therefore did not form coherent wavefields capable of generating artifacts. However, the final results based on different theoretical covariance matrices showed slight deviations compared to the noise-free tests.

4. Discussion

The assumptions and approximations used in this study are generally applied in seismic inversion or imaging. For example, in most WRI methods, in which the penalty scalar is subjectively defined, the constant is commonly very large,[22] which is consistent with our assumption that the main body of the model domain Hessian is larger than the identity matrix. Moreover, the sampling operator is also defined subjectively, which can be the size of $N_{model} \times N_{receiver}$ or $N_{model} \times N_{model}$. Furthermore, **Equation XX** provided the final calculation method for the extended source used in this paper, ensuring the accuracy of the reconstructed wavefield. However, this series of approximations mainly focused on the computational time by transforming the space calculation to the receiver calculation, which weakens the potential of WRI in the model space, making it more applicable in complex cases with accurately calculated extended sources. Notably, the theoretical covariance matrix was defined before performing inversion, while most Bayesian-based inversion methods use the covariance matrix to evaluate the accuracy or resolution of the final results. The main difference between the two methods is the different definitions of the covariance matrix. In our method, the covariance matrix is separated into measurement and theoretical covariance matrices, representing different error distributions, respectively, while the other Bayesian-based method combines the two covariance matrices into one. However, according to the covariance matrix definition

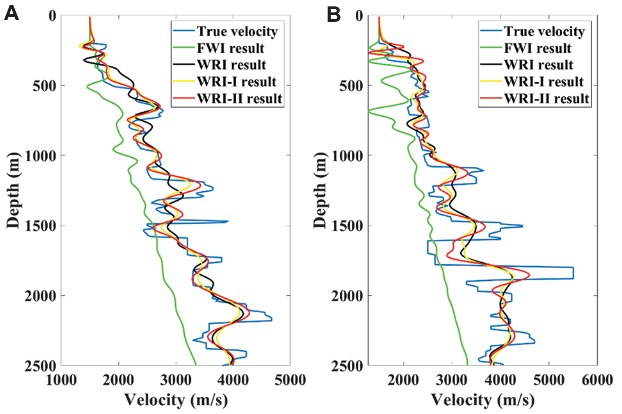

Figure 10. Trace comparison. (A) Located at x = 3,800 m, and (B) located at x = 6,500 m.
Abbreviations: FWI: Full-waveform inversion; WRI: Wavefield reconstruction inversion.

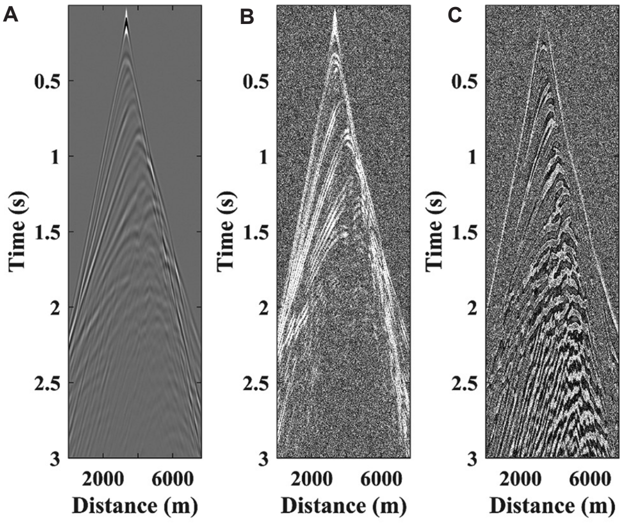

Figure 11. Extended source comparison. (A) Identity matrix definition, (B) calculated by **Equation XX**, and (C) calculated by **Equation (XXI).**

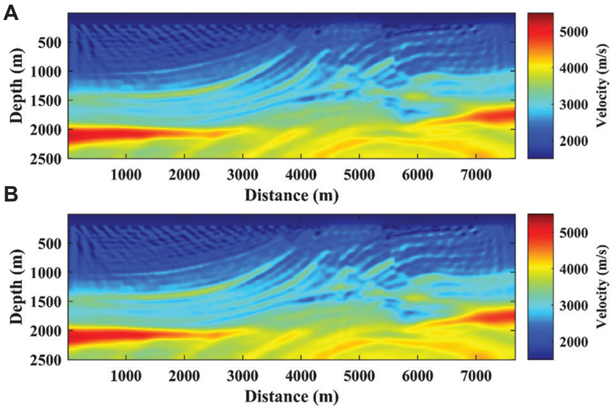

Figure 12. Inversion results. (A) Wavefield reconstruction inversion (WRI) result based on the extended source, and (B) WRI result based on the defined extended source.

in the Bayesian-based methods, the proposed method can be further evaluated based on the combined covariance matrix. Regarding the computational cost, the traditional WRI requires three PDE solvers, while the proposed method only requires two, similar to the traditional FWI. In addition, the source-extended FWI also needed three PDE solvers, the same as the fast WRI proposed by Lin *et al.*[33]

5. Conclusion

This study introduced the Hessian, a function of the measurement and theoretical covariance matrices, into WRI based on Bayesian inference. Furthermore, the connections between the data and model domain equations were discussed, which led to a simplified extended source calculation method for the extended source. A theoretical covariance matrix definition based on the new calculation method was proposed and validated through numerical tests. Further research may focus on more theoretical covariance matrix definitions and their effect on inversion.

Acknowledgments

None.

Funding

The study is supported by the Qingdao New Energy Shandong Laboratory Open Project under Grant QNESL OP202304.

Conflict of interest

Huaishan Liu is employed by the Key Laboratory of Oil & Gas Reservoir Geophysics, Sinopec, Beijing, China. The remaining authors declare they have no competing interests.

Author contributions

Conceptualization: Yuzhao Lin
Formal analysis: Yuzhao Lin, Huaishan Liu
Investigation: Huaishan Liu, Hehao Tang, Jinghao Li
Methodology: Huaishan Liu, Lei Xing
Writing–original draft: Yuzhao Lin
Writing–review & editing: Kun Huang

Availability of data

Data are available from the corresponding author on reasonable request.

References

1. Tarantola A, Valette B. Generalized nonlinear inverse problems solved using the least squares criterion. *Rev Geophys*. 1982;20(2):219-232.

   doi: 10.1029/RG020i002P00219

2. Tarantola A. Inversion of seismic reflection data in the acoustic approximation. *Geophysics*. 1984;49(8):1259-1266.

   doi: 10.1190/1.1441754

3. Tarantola A. *Inverse Problem Theory and Methods for Model Parameter Estimation*. Indian: SIAM; 2005.

4. Virieux J, Operto S. An overview of full-waveform inversion in exploration geophysics. *Geophysics*. 2009;74(6): WCC1-WCC26.

   doi: 10.1190/1.3238367

5. Gauthier O, Virieux J, Tarantola A. Two-dimensional nonlinear inversion of seismic waveforms: Numerical results. *Geophysics*. 1986;51(7):1387-1403.

   doi: 10.1190/1.1442188

6. Warner M, Guasch L. Adaptive waveform inversion: Theory.

Geophysics. 2016;81(6):R429-R445.

doi: 10.1190/geo2015-0387.1

7. Guasch L, Warner M, Ravaut C. Adaptive waveform inversion: Practice. *Geophysics*. 2019;84(1):R447-R461.

   doi: 10.1190/geo2018-0377.1

8. Wu Z, Alkhalifah T. Selective data extension for full-waveform inversion: An efficient solution for cycle skipping. *Geophysics*. 2018;83(2):R201-R211.

   doi: 10.1190/geo2016-0649.1

9. Métivier L, Brossier R, Merigot Q, Oudet E, Virieux J. An optimal transport approach for seismic tomography: Application to 3D full waveform inversion. *Inverse Probl*. 2016;32(11):115008.

   doi: 10.1088/0266-5611/32/11/115008

10. Métivier L, Brossier R, Merigot Q, Oudet E, Virieux J. Measuring the misfit between seismograms using an optimal transport distance: Application to full waveform inversion. *Geophys J Int*. 2017;205(1):332-364.

    doi: 10.1093/gji/ggw027

11. Pladys A, Brossier R, Irnaka M, Kamath N, Métivier L. *Graph Space Optimal Transport Based FWI: 3D OBC Valhall Case Study. SEG Tech Program Expanded Abstracts*. United States: Society of Exploration Geophysicists; 2020. p. 696-700.

12. Lin Y, Liu H, Sun J, Xing L. Time-domain wavefield reconstruction inversion based on unbalanced optimal transport. *IEEE Trans Geosci Remote Sens*. 2022;60:5920612.

    doi: 10.1109/TGRS.2022.3210576

13. Bunks C, Saleck FM, Zaleski S, Chavent G. Multiscale seismic waveform inversion. *Geophysics*. 1995;60(5): 1457-1473.

    doi: 10.1190/1.1443880

14. Fu L, Guo B, Schuster GT. Multiscale phase inversion of seismic data. *Geophysics*. 2018;83(3):R159-R171.

15. Symes WW. Objective Functions for Full Waveform Inversion. In: *74th EAGE Conference and Exhibition-Workshops*; 2012.

16. Fu L, Symes WW. A discrepancy-based penalty method for extended waveform inversion. *Geophysics*. 2017;82(4):R287-R298.

17. Fu L, Symes WW. An adaptive multiscale algorithm for efficient extended waveform inversion. *Geophysics*. 2017;82(3):R183-R197.

    doi: 10.1190/geo2016-0426.1

18. Huang G, Nammour R, Symes WW. Full waveform inversion via source-receiver extension. *Geophysics*. 2017;82(3):R153-R171.

    doi: 10.1190/geo2016-0301.1

19. Huang G, Nammour R, Symes WW. Source-independent extended waveform inversion based on spacetime source extension: Frequency-domain implementation. *Geophysics*. 2018;83(5):R449-R461.

    doi: 10.1190/geo2017-0333.1

20. Symes WW. *Full Waveform Inversion by Source Extension: Why it Works*. Preprint arXiv; 2020.

    doi: 10.48550/arXiv.2003.12538

21. Leeuwen TV, Herrmann FJ. Mitigating local minima in full-waveform inversion by expanding the search space. *Geophys J Int*. 2013;195(1):661-667.

    doi: 10.1093/gji/ggt277

22. Leeuwen T, Herrmann FJ. A penalty method for PDE-constrained optimization in inverse problems. *Inverse Probl*. 2015;32(1):015007.

    doi: 10.1088/0266-5611/32/1/015007

23. Wang C, Yingst D, Farmer P, Leveille J. Full-Waveform Inversion with the Reconstructed Wavefield Method. In: *Conference SEG Tech Program Expanded Abstracts*; 2016. p. 1237-1241.

24. Li ZC, Lin YZ, Zhang K, Li YY, Yu ZN. Time-domain wavefield reconstruction inversion. *Appl Geophys*. 2017;14(4):523-528.

    doi: 10.1007/s11770-017-0629-6

25. Rizzuti G, Louboutin M, Wang R, Daskalakis E, Herrmann F. A dual formulation for time-domain wavefield reconstruction inversion. In: *SEG Tech Program Expanded Abstracts*. United States: Georgia Institute of Technology; 2019. p. 1480-1485.

26. Rizzuti G, Louboutin M, Wang R, Herrmann F. A dual formulation of wavefield reconstruction inversion for large-scale seismic inversion. *Geophysics*. 2021;86(6):R879-R893.

    doi: 10.1190/geo2020-0746.1

27. Aghamiry HS, Gholami A, Operto S. Improving full waveform inversion by wavefield reconstruction with the alternating direction method of multipliers. *Geophysics*. 2019;84(1):R139-R162.

    doi: 10.1190/geo2018-0093.1

28. Aghamiry HS, Gholami A, Operto S. Implementing bound constraints and total-variation regularization in extended full waveform inversion with the alternating direction method of multiplier: Application to large contrast media. *Geophys J Int*. 2019;212(2):855-872.

    doi: 10.1093/gji/ggz189

29. Aghamiry HS, Gholami A, Operto S. ADMM-based multi-parameter wavefield reconstruction inversion in VTI acoustic media with TV regularization. *Geophys J Int*.

2019;219(2):1316-1333.

doi: 10.1093/gji/ggz369

30. Lin Y, Liu H, Xing L, Lin H. Time-domain wavefield reconstruction inversion solutions in the weighted full waveform inversion form. *IEEE Trans Geosci Remote Sens*. 2022;60(1):5923514.

    doi: 10.1109/TGRS.2022.3224383

31. Gholami A, Aghamiry HS, Operto S. *Multiplier Waveform Inversion*. Preprint arXiv; 2021.

32. Gholami A, Aghamiry HS, Operto S. Clarifying Some Issues on Extended FWI: Scattered-Field Equation, Time Reversal and Source Reconstruction. In: *Conference SEG Annual Meeting Expanded Abstracts*; 2021. p. 802-806.

33. Lin Y, Liu H, Xing L, Lin H. Time-domain wavefield reconstruction inversion solutions in the weighted full waveform inversion form. *IEEE Trans Geosci Remote Sens*. 2022;60(1):5923514.

    doi: 10.1109/TGRS.2022.3224383

34. Operto S, Gholami A, Aghamiry HS, Guo G, Mamfoumbi F, Beller S. Full waveform inversion beyond the Born approximation: A tutorial review. *Geophysics*. 2023;88(6):WCC87-WC127.

    doi: 10.1190/geo2022-0758.1

35. Stuart AM. Inverse problems: A Bayesian perspective. *Acta Numer*. 2010;19:451-559.

    doi: 10.1017/S0962492910000031

36. Figueiredo LP, Grana D, Bordignon FL, Santos M, Roisenberg M, Rodrigues BB. Joint Bayesian inversion based on rock-physics prior modeling for the estimation of spatially correlated reservoir properties. *Geophysics*. 2018;83(1):M49-M61.

    doi: 10.1190/geo2017-0363.1

37. Huang X, Eikrem KS, Jakobsen M, Nævdal G. Bayesian full-waveform inversion in anisotropic elastic media using the iterated extended Kalman filter. *Geophysics*. 2020;85(4):C125-C139.

    doi: 10.1190/geo2019-0329.1

38. Leeuwen T. *A Note on Extended Full Waveform Inversion*. Preprint arXiv; 2019.

    doi: 10.48550/arXiv.1904.00363

39. Lin Y, Leeuwen T, Liu H, Sun J, Xing L. A fast wavefield reconstruction inversion solution in the frequency domain. *Geophysics*. 2023;88(1):1-62.

    doi: 10.1190/geo2022-0385.1

40. Gholami A, Aghamiry HS, Operto S. *Extended Full Waveform Inversion in the Time Domain by the Augmented Lagrangian Method*. arXiv Preprint; 2021.

    doi: 10.48550/arXiv.2011.14102

41. Plessix RE. A review of the adjoint-state method for computing the gradient of a functional with geophysical applications. *Geophys J Int*. 2006;167(2):495-503.

    doi: 10.1111/j.1365-246X.2006.02978.x

ACCSCIENCE PUBLISHING

Journal of Seismic Exploration

ARTICLE

An attention-guided graph neural network and U-Net++-based reservoir porosity prediction system

Guoqing Chen[1], **Tianwen Zhao**[2], **Cong Pang**[3,4], **Palakorn Seenoi**[5], **Nipada Papukdee**[6], **Piyapatr Busababodhin**[7]*

[1]Mathematical Modeling Research Center, Chengdu Jincheng College, Chengdu, Sichuan, China

[2]Department of Trade and Logistics, Daegu Catholic University, Gyeongsan, Daegu, Republic of Korea

[3]Institute of Seismology, China Earthquake Administration, Wuhan, Hubei, China

[4]Wuhan Gravitation and Solid Earth Tides, National Observation and Research Station, Wuhan, Hubei, China

[5]Department of Statistics, Faculty of Science, Khon Kaen University, Mueang Khon Kaen, Khon Kaen, Thailand

[6]Department of Applied Statistics, Rajamangala University of Technology Isan Khon Kaen Campus, Mueang Khon Kaen, Khon Kaen, Thailand

[7]Department of Mathematics, Faculty of Science, Mahasarakham University, Kantharawichai, Maha Sarakham, Thailand

Abstract

Accurate prediction of reservoir porosity is fundamental for hydrocarbon resource evaluation and development planning, yet traditional methods struggle with spatial heterogeneity and complex geological structures. This study proposes a hybrid deep learning framework that integrates U-Net++ with an attention-guided graph neural network to simultaneously capture multiscale well logging data features and non-Euclidean spatial dependencies. The model incorporates dense skip connections, deep supervision, and dual-channel attention mechanisms to enhance both local feature extraction and global topological modeling. Experiments on a real-world continental sedimentary basin dataset (26 wells, ~40 km^2) demonstrated that the proposed method achieved a mean squared error (MSE) of 4.62, mean absolute error of 1.24, coefficient of determination (R^2) of 0.912, and structural similarity index measure of 0.831, representing a 14.9–38.7% reduction in prediction errors relative to widely used deep learning and graph-based baselines. Statistical tests ($p<0.05$) confirmed the significance of the improvements. The model was particularly robust in extreme porosity ranges (>16% or <8%), reducing errors by 23.1–42.6% compared to U-Net++. Ablation studies highlighted the contribution of graph structure (19.0% MSE reduction), attention mechanism (15.0%), and deep supervision (12.5%). Beyond predictive accuracy, attention-weight analysis revealed strong alignment with geologically meaningful features, such as faults and sedimentary facies boundaries, thereby enhancing interpretability. The proposed framework offers a scalable and interpretable solution for reservoir characterization, with broad potential applications in heterogeneous and faulted reservoirs.

Keywords: Reservoir porosity prediction; Graph neural network; U-Net++; Attention mechanism; Spatial heterogeneity

***Corresponding author:**
Piyapatr Busababodhin
(Piyapatr.b@msu.ac.th)

Citation: Chen G, Zhao T, Pang C, Seenoi P, Papukdee N, Busababodhin P. An attention-guided graph neural network and U-Net++-based reservoir porosity prediction system. *J Seismic Explor*. 2025;34(4):70-87. doi: 10.36922/JSE025300044

Received: July 24, 2025

Revised: August 30, 2025

Accepted: October 10, 2025

1. Introduction

Reservoir porosity is a core parameter that characterizes the capacity of rock storage space and directly affects the reserve assessment, development potential analysis, and development plan optimization of oil and gas reservoirs.[1] In oil and gas exploration and development, accurately obtaining the porosity distribution of underground reservoirs is of great significance for reducing exploration risks and improving recovery rates.[2]

However, due to the complexity of geological structures and the indirectness of underground information, traditional porosity prediction methods, such as seismic inversion and well logging data interpretation, often have limitations in data accuracy, resolution, and modeling capabilities. In particular, it is difficult to accurately characterize the spatial variation of porosity in heterogeneous reservoirs and fault development areas.[3] This challenge is particularly prominent in the exploration of unconventional oil and gas resources, and there is an urgent need to develop more intelligent and precise prediction technologies.

In recent years, artificial intelligence technology has developed rapidly, and deep learning, especially convolutional neural networks (CNNs), has demonstrated excellent feature extraction capabilities in reservoir modeling and attribute prediction.[4] The U-Net structure has been widely used in geological image segmentation and attribute prediction because it can effectively capture multiscale spatial information.[5] However, such methods usually rely on regular grid data, and their ability to model unstructured and highly spatially heterogeneous geological data is still insufficiently studied. In addition, complex spatial topological relationships, such as stratigraphic continuity and fracture intersections, are widely present in reservoirs and are difficult to fully represent by relying solely on traditional convolution operations. Therefore, how to effectively incorporate prior knowledge of geological structures into the model and enhance the ability to identify key structures has become an important challenge in current reservoir porosity prediction.[6]

To address the above problems, this paper proposes a reservoir porosity prediction method that integrates U-Net++ and an attention-guided graph neural network (AG-GNN). This method utilizes the enhanced multiscale feature extraction and fusion capabilities of U-Net++ to process spatial hierarchical information in seismic and well logging data; at the same time, it introduces non-Euclidean relationships between graph neural network (GNN) modeling nodes and achieves adaptive enhancement of key geological areas through the attention mechanism, thereby improving the recognition and prediction performance of the model in complex structural areas. This hybrid architecture not only enhances the ability to represent heterogeneity and topological structures but also exhibits good generalization performance under limited sample conditions. It is also applicable to a variety of actual geological scenarios.

The main contributions of this study include:

(i) A hybrid modeling framework combining AG-GNN and deep convolutional structures is proposed, significantly improving the accuracy and robustness of porosity prediction under complex geological conditions.
(ii) The applicability and superiority of the model in different geological regions are verified through multiple sets of real data experiments.
(iii) A scalable technical path is provided for unconventional resource exploration and complex fault block reservoir modeling.
(iv) During the research process, the combination of geological interpretability and algorithm performance is emphasized. Through attention-weight visualization and feature response analysis, the mechanistic understanding of the geological causes of porosity distribution is enhanced, and the interpretability and practical guidance value of the results are improved.

2. Overview of related work

As an important parameter reflecting the spatial structure of underground reservoirs, reservoir porosity has long been a key research object in the field of oil and gas exploration and development.[7,8] Traditional porosity prediction methods mainly rely on geostatistical methods and seismic attribute inversion technology.[9] Geostatistical methods, such as Kriging interpolation technology, estimate porosity spatially based on the spatial correlation of sample data, but their accuracy is often low when dealing with nonlinear relationships and complex geological environments.[10] Seismic attribute inversion methods use seismic data to invert underground porosity. Although they can provide estimates within a relatively large spatial range, their applicability and accuracy are also limited because they rely on the assumption of seismic wave propagation models and have large errors under complex geological conditions.[11] In general, traditional methods are difficult to provide sufficient accuracy and robustness when faced with complex spatial structures and high-dimensional features.

In recent years, with the rapid development of deep learning technology, the application of CNNs in geological prediction has gradually become a mainstream method. CNNs have made significant progress in porosity prediction due to their powerful feature extraction capabilities.[12] In particular, U-Net and its variants, through their unique encoder–decoder structure and skip connection mechanism, can extract multiscale spatial features while ensuring spatial resolution, thus achieving successful applications in fields such as medical image segmentation.[13] However, the structure of the U-Net still has certain limitations in processing large-scale high-dimensional spatial data. In particular, when geological data have a complex topological structure, traditional CNNs are difficult to effectively capture the global spatial dependencies between data.[14]

GNNs, as an emerging deep learning method, have gradually attracted widespread attention in the academic community. GNNs can effectively model the complex dependencies between nodes in the data and are particularly suitable for processing data with irregular topological structures.[15] Variants such as graph convolutional networks (GCNs) and graph attention networks (GATs) have further improved the performance of the model in learning relationships between nodes through graph convolution operations and attention mechanisms.[16-19] The application of GNN in geology is mainly reflected in underground structure modeling and prediction tasks. It can automatically learn the interaction between nodes in large-scale spatial data, thereby improving the shortcomings of traditional methods in spatial dependency modeling.[20-22] However, although GNNs have advantages in processing complex spatial structures, how to effectively integrate them into porosity prediction tasks remains a challenge, especially how to deal with noise and sparsity in geological data.

In this context, the combination of U-Net++ and the attention mechanism provides a new idea for the application of deep learning models in porosity prediction. U-Net++ further improves the ability of multiscale feature fusion through improved skip connections and deep supervision mechanisms, and can capture more detailed geological features at different scales.[23] At the same time, the introduction of the attention mechanism enables the model to automatically focus on key areas that have an important impact on porosity prediction during the prediction process, thereby effectively improving the prediction accuracy. Compared with the traditional U-Net model, U-Net++ can accurately capture the porosity variation law of different depths or regions in a more complex geological background, especially in an environment with high variability and complex structure, significantly improving the stability and reliability of the prediction.

Although the current deep learning models have made some progress in porosity prediction, there are still some shortcomings. First, most existing methods have not fully considered the explicit modeling of spatial topological relationships. In particular, when dealing with complex geological data, it is difficult for the model to effectively capture the connection and interaction between different geological units. Secondly, although models such as U-Net++ have improved the prediction accuracy through multiscale feature fusion, the sensitivity to some key geological structural features, such as faults and folds, is still insufficient. In particular, when the geological conditions are extremely complex, the performance of the model may be affected to a certain extent. Therefore, future research needs to further enhance the model's sensitivity to spatial topological relationships and key geological features, and promote the further development and application of deep learning methods in complex geological backgrounds.

3. Methods

3.1. Overall architecture design of the model

This study proposed an end-to-end reservoir porosity prediction model that integrates U-Net++ and AG-GNN, as shown in Figure 1. The architecture design aims to capture both local fine-grained features and global spatial topological associations. Specifically, the U-Net++ module is used to efficiently extract local interlayer detail changes in seismic attributes and logging data to generate multiscale feature maps; the AG-GNN module models the reservoir spatial topology based on geological structures and spatial adjacency relationships, and achieves global modeling and prediction of porosity changes across wells and profiles.

The input layer receives the normalized seismic attribute cube and well logging data curve; the encoder part is composed of multiscale deep convolution and dilated convolution; the skip connection is connected to the decoder through a dense path; the output multiscale feature map is input into AG-GNN for spatial relationship modeling; and the final fully connected layer outputs the predicted porosity distribution map.

3.2. U-Net++ improvement details

To enhance the adaptability of the model to heterogeneous seismic and well logging data, we made two improvements based on the traditional U-Net++: (i) deep separable convolution and dilated convolution were introduced to increase the receptive field while keeping the number of parameters low; and (ii) deep supervision and multiscale skip connection were used to improve the gradient transfer and feature fusion effects.

The convolution layer of the encoder part is replaced by a deep separable convolution:

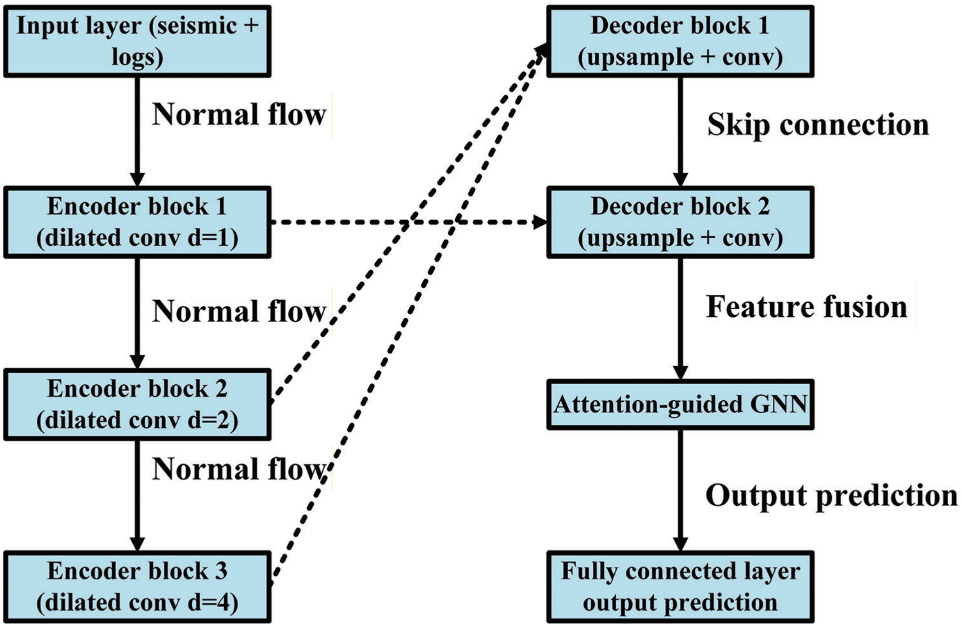

Figure 1. Overall architecture of the U-Net++ and attention-guided graph neural network (GNN) fusion model
Abbreviation: Conv: Convolutional layer.

$$Y = (X *_{dw} K_{dw}) *_{pw} K_{pw} \tag{I}$$

where dw is channel-by-channel convolution, pw is a 1×1 convolution, and K_{dv} and K_{pw} are convolution kernels, respectively.

The decoder introduces dilated convolution:

$$Y(p) = \sum_{d \in D} W(d) \cdot X(p + r \cdot d) \tag{II}$$

where r is the dilation rate. The effective increase in the receptive field of the feature map is shown in Figure 2.

From the data in Table 1, it can be seen that the improved U-Net++ model performed better than the original version in many key indicators, and the number of model parameters was reduced.

The number of parameters of the improved model was reduced from 5.2 M to 4.8 M, a decrease of approximately 7.7%, whereas the prediction accuracy was significantly improved: the mean squared error (MSE) reduced from 0.022 to 0.017 (decrease of 22.7%), the mean absolute error (MAE) reduced from 0.103 to 0.085 (decrease of 17.5%), the coefficient of determination (R^2) increased from 0.847 to 0.895 (increase of 5.7%), and the structural similarity index measure (SSIM) increased from 0.789 to 0.832 (increase of 5.4%). In addition, the inference time was shortened from 0.84 s to 0.79 s, an improvement of approximately 6.0%. These data show that the improved model not only reduces the computational complexity but also further improves the accuracy and efficiency of the prediction, achieving a balance between lightweight and high performance.

Table 1. Comparison of the complexity and prediction performance of the U-Net++model before and after improvement

Model	Parameter quantity (M)	MSE	MAE	R^2	Reasoning time (s)	SSIM
Original U-Net++	5.2	0.022	0.103	0.847	0.84	0.789
Improved U-Net++	4.8	0.017	0.085	0.895	0.79	0.832

Abbreviations: MAE: Mean absolute error; MSE: Mean squared error; SSIM: Structural similarity index measure.

3.3. Design of attention-guided GNN

The AG-GNN design includes three parts: node feature encoding, adjacency relationship construction, and attention mechanism fusion:[24]

(i) Node feature encoding: geological attributes, such as well logging data porosity, seismic reflection coefficient, strike-slip fault index, and lithology mark, are spliced into node vectors:

$$F_i = [f_{i,1}, f_{i,2}, \cdots, f_{i,N}] \tag{III}$$

(ii) Adjacency relationship construction: Based on the spatial coordinates of the well location (x_i, y_i, z_i) and

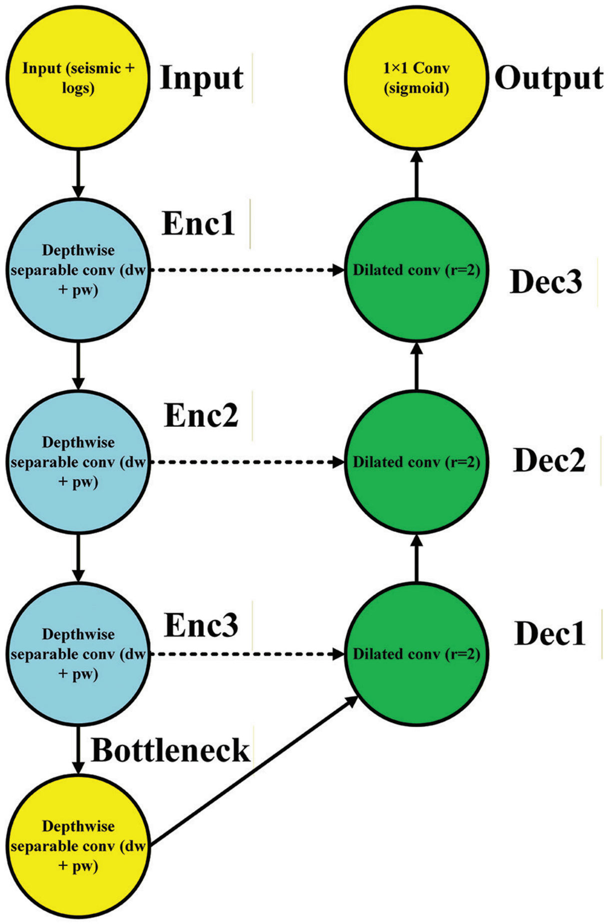

Figure 2. Schematic diagram of the improved U-Net++ architecture (including depthwise separable convolution and dilated convolution)
Abbreviation: Conv: Convolutional layer.

the structural interpretation results, the edges are connected within a radius of 200 m:

$$A_{ij} = \begin{cases} 1, & d_{ij} \le r \\ 0, & else \end{cases} \quad \text{(IV)}$$

where d_{ij} is the well distance.

(iii) Attention mechanism: Combining channel attention and spatial attention. Channel attention calculates channel weight (w_c):

$$w_c = \sigma(\mathrm{MLP}(\mathrm{AvgPool}(F)) + \mathrm{MLP}(\mathrm{MaxPool}(F))) \quad \text{(V)}$$

Spatial attention calculates the spatial weight (α_{ij}) between nodes:

$$\alpha_{ij} = \frac{\exp(\mathrm{LeakyReLU}(a^T[WF_i \ \mathrm{P}WF_j]))}{\sum_{k \in N_i} \exp(\mathrm{LeakyReLU}(a^T[WF_i \ \ WF_k]))} \quad \text{(VI)}$$

The process of AG-GNN extracting cross-well spatial features through adjacency relations is shown in Figure 3.

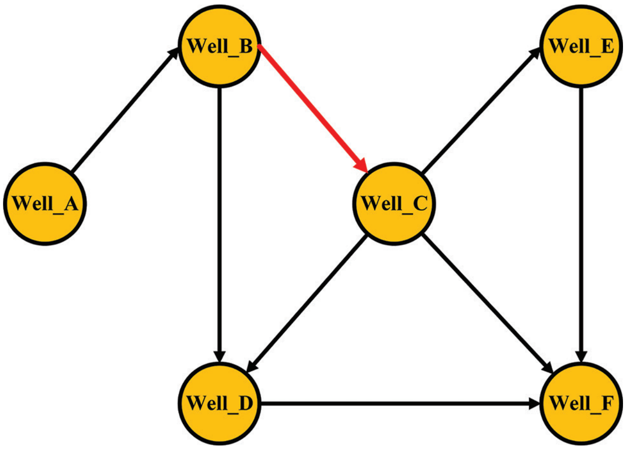

Figure 3. Attention-guided graph neural network's spatial topology modeling diagram

The setting of the neighbor radius has a significant impact on the model performance, and there is an optimal value range, as shown in Table 2.

When the neighbor radius was 200 m, the model reached the optimal balance, with an MSE of 0.017, R^2 of 0.895, and SSIM of 0.832—all indicators were better than other radius settings. As the neighbor radius increased from 100 m to 200 m, the average node degree increased from 3.2 to 5.8, prompting the model to capture richer spatial associations, reducing MSE by 19.0% and increasing R^2 by 4.3%. In contrast, when the neighbor radius exceeded 200 m, the over-expanded receptive field (average degree 8.1 at 300 m and 11.5 at 400 m) introduced noise associations, resulting in performance degradation—compared with the optimal radius, MSE deteriorated by 35.3% and SSIM decreased by 4.8% at a neighbor radius of 400 m. The calculation time showed a monotonically increasing trend, from 0.64 s at a neighbor radius of 100 m to 1.02 s at 400 m, an increase of 59.4%, confirming the positive correlation between computational complexity and adjacency radius.

In areas with dense well points, graph construction strategies based on spatial proximity can effectively characterize reservoir spatial topological relationships. However, in areas with low well control, graph structures constructed solely based on Euclidean distances between wells often lack connectivity, resulting in limited feature propagation between nodes and making it difficult to robustly model large-scale geological features. To address this issue, this study proposed a graph structure enhancement method that integrates multi-source geological and geophysical information. First, a seismic data-driven virtual node generation mechanism was introduced. Based on the gradient characteristics of seismic attributes, such as reflection intensity and coherence volume, geologically significant anomalies were identified

Table 2. Analysis of the impact of the neighbor radius on the performance of the AG-GNN model

Adjacent radius, r (m)	MSE	R^2	Average	SSIM	Number of nodes	Computation time (s)
100	0.021	0.858	3.2	0.801	125	0.64
200	0.017	0.895	5.8	0.832	125	0.72
300	0.019	0.884	8.1	0.817	125	0.89
400	0.023	0.841	11.5	0.792	125	1.02

Abbreviations: MSE: Mean squared error; SSIM: Structural similarity index measure.

in sparse inter-well areas as virtual nodes, and their feature vectors were constructed as statistics, such as mean and variance, corresponding to the seismic attribute window. By establishing connections with actual well points, virtual nodes could form information bridges in areas with low well control, significantly improving the connectivity of the graph. Secondly, the Euclidean distance constraint was overcome by integrating prior knowledge such as geological structure and sedimentary facies. Well points located within the same fault block, sedimentary facies, or fracture system were connected even if they were far apart. Nodes that were spatially adjacent but had distinct geological origins were disconnected or had their weights reduced, making the graph structure more consistent with geological laws. Finally, a density-adaptive dynamic adjacency radius adjustment strategy was implemented. A smaller radius was used in densely populated areas to capture local details, while an expanded adjacency radius was used in sparse areas to ensure that nodes have sufficient neighbors and avoid isolated nodes.

3.4. Model training and loss function

The combined loss function was used in end-to-end model training:[25]

$$\mathcal{L}_{total} = \alpha \cdot \mathrm{MSE}(y, \check{y}) + \beta \cdot (1 - \mathrm{SSIM}(y, \check{y})) + \gamma \cdot \mathrm{L2}(\theta) \quad \text{(VII)}$$

where α (0.7), β (0.3), γ (10^{-4}) are weights, and θ is a model parameter. Regularization uses L2 regularization and dropout ($p = 0.3$) to prevent overfitting; the optimizer uses AdamW, the initial learning rate is 1×10^{-3}, and the learning rate scheduler StepLR decays to 0.5 times every 20 epochs.

The combination of loss functions had a systematic impact on model performance. The experimental results are shown in Table 3.

When only MSE loss was used, the model achieved baseline performance (MSE = 0.020, R^2 = 0.861). After the introduction of SSIM loss, various indicators were significantly improved, among which MSE was reduced by 15.0%, R^2 increased by 3.4%, and SSIM increased from 0.805 to 0.832, an increase of 3.4%. After further incorporating L2 regularization, the model performance continued to improve and reached the optimal level (MSE = 0.016, R^2 = 0.902), which was 20.0% lower than the single MSE loss scheme, and R^2 was increased by 4.1%. The SSIM showed a stable growth trend under the composite loss function, gradually increasing from 0.805 to 0.837, indicating that the multi-objective optimization strategy effectively enhances the modeling ability of the spatial structure. These quantitative results confirm that through a carefully designed loss function combination, the prediction accuracy and spatial consistency can be significantly improved without increasing the complexity of the model.

Table 3. Comparison of the impact of different loss function combinations on model prediction performance

Loss combination	MSE	MAE	R^2	SSIM
MSE only	0.020	0.092	0.861	0.805
MSE+SSIM	0.017	0.085	0.895	0.832
MSE+SSIM+L2	0.016	0.083	0.902	0.837

Abbreviations: MAE: Mean absolute error; MSE: Mean squared error; SSIM: Structural similarity index measure.

3.5. Model fusion and end-to-end prediction process

This study fed the multiscale feature map output of U-Net++ into AG-GNN to explicitly encode the spatial topological relationship. After graph attention, the porosity value was predicted through the fully connected layer to achieve end-to-end optimization. The prediction process is shown in Figure 4.

The joint prediction of local structural differences and global spatial associations in complex reservoirs was achieved, effectively improving the prediction accuracy and geological rationality.

4. Data and experimental design

4.1. Data source and description

The data used in the experiment were from the lower oil formation in a typical continental sedimentary basin in northwestern China. The area has typical sand–mud interbed sedimentary characteristics, significant reservoir heterogeneity, and frequent tectonic activities. The study area contains 26 wells, covering an area of approximately 40 km². The structural morphology is mainly anticline and fault, and the sedimentary facies are mainly braided river and delta front, providing an ideal scenario for complex reservoir prediction.

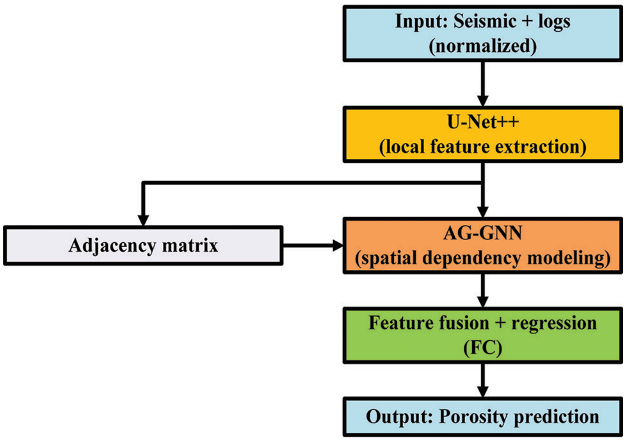

Figure 4. End-to-end process from seismic and well logging data to porosity prediction

Abbreviation: AG-GNN: Attention-guided graph neural network.

This study used three types of data:

(i) Well logging data: Encompassing five types of curves, including acoustic time difference, natural gamma, resistivity, neutron porosity, and bulk density. The sampling interval was 0.1 m, and the data coverage depth range was 1,000–2,500 m. Some wells had significant intervals of missing log data.

(ii) Seismic attribute data: Extracted based on three-dimensional seismic data, including 12 types of structural and stratigraphic attributes, such as reflection coefficient, instantaneous amplitude, frequency, and phase. The sampling resolution is 25 m × 25 m, and the vertical resolution corresponds to the well depth.

(iii) Core measured porosity: As a supervised regression label (target), a total of 1,848 sample points were collected, with a porosity range of 2.1–21.4% and an average of 12.7%, which was used as the training target of this study.

Figure 5 shows the spatial distribution of 26 wells in the study area. The horizontal and vertical coordinates represent the east and north coordinates of the wellhead position (unit: km).

The well locations are evenly distributed in the region, covering the entire target layer structure range. This facilitated the construction of a reasonable adjacency matrix when training the GNN, supporting efficient modeling of spatial information. This also reflects a core advantage of the GNN—it can use the cross-well spatial structure for feature propagation, thereby improving the stability of local predictions.

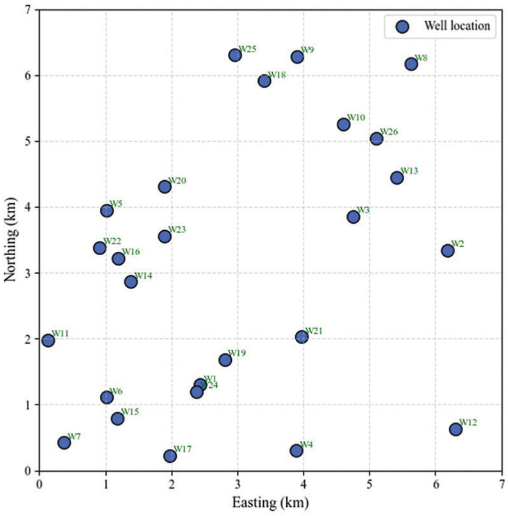

Figure 5. Well location and sample spatial distribution map

4.2. Data preprocessing

4.2.1. Spatial alignment and interpolation

First, the seismic and logging data were spatially aligned, and the geographic coordinate projection conversion (UTM Zone 48N) was used to perform three-dimensional interpolation based on the well location.[26] The interpolation used the spline-based local weighting method to ensure that each well point has a corresponding multiscale seismic attribute sample.

4.2.2. Feature normalization and missing value processing

Continuous features were normalized to the interval [0, 1], and the minimum–maximum scaling was performed using the following formula:

$$x' = \frac{x - min(x)}{max(x) - min(x)} \tag{VIII}$$

The missing curves were repaired using K-nearest neighbor imputation (k = 5) to retain the continuity of the physical characteristics of the well. Invalid samples (>50% missing) were removed, and the final number of retained samples was 1,720.

4.2.3. Feature selection

Through the Pearson correlation coefficient and variance analysis (ANOVA), the top eight seismic attribute features highly correlated with porosity were retained, as shown in Table 4.

Table 4. Pearson correlation analysis of seismic attributes and porosity

Serial number	Attribute name	Correlation coefficient (r)	Retain
1	Reflection coefficient	0.81	Yes
2	RMS amplitude	0.76	Yes
3	Instantaneous frequency	0.68	Yes
4	Absorption attenuation coefficient	−0.63	Yes
5	Amplitude envelope	0.59	Yes
6	Multiscale GLCM texture	0.53	Yes
7	Main reflection direction	0.49	Yes
8	Inter-layer reflection difference	−0.45	Yes

Abbreviations: GLCM: Gray level co-occurrence matrix; RMS: Root mean square.

Figure 6 compares the relationship between three typical seismic attributes (root mean square [RMS] amplitude, instantaneous frequency, and gray level co-occurrence matrix [GLCM] texture) and measured porosity.

The RMS amplitude was positively correlated with porosity, and the fitting trend was relatively obvious. The instantaneous frequency fluctuated greatly, but maintained a certain correlation overall. The GLCM texture was negatively correlated with the porosity, indicating that the reservoir structure difference can be reflected from the texture perspective. These attributes were retained in the feature selection stage, proving their effectiveness in characterizing reservoir properties and providing a solid foundation for subsequent model input.

4.3. Experimental settings

4.3.1. Dataset division

To ensure the generalization ability of the model, a stratified sampling strategy was used to divide the data into a training set, validation set, and test set, with a ratio of 70%:15%:15%. The division results are shown in Table 5.

Table 5. Sample division results

Dataset	Number of samples	Average porosity (%)	Standard deviation of porosity
Training set	1,204	12.73	4.22
Validation set	258	12.68	4.31
Test set	258	12.71	4.19

The average porosity of the training set (1,204 samples), validation set, and test set (258 samples each) was 12.73%, 12.68%, and 12.71%, respectively, with a difference of no more than 0.05%, indicating that the mean porosity remains highly stable among different data sets. More importantly, the porosity standard deviations of the three data sets were 4.22, 4.31, and 4.19, respectively, with a range of only 0.12, and a coefficient of variation difference of no more than 2.9%, confirming that the fluctuation characteristics of reservoir physical properties are balanced and preserved during the training, validation, and testing stages. When the validation set and the test set had the same sample size (258 samples each), the difference in statistical parameters was negligible: the average porosity difference was 0.03%, and the standard deviation difference was 0.12. This strict symmetry design effectively avoids sampling bias in the evaluation process. Although the sample size of the training set was 4.67 times that of the validation and test sets, its standard deviation (4.22) was only 0.03 different from that of the test set (4.19), indicating that large data volume training does not sacrifice the representativeness of data distribution.

4.3.2. Hardware and software environment

All experiments were run on Ubuntu 20.04 (Canonical Ltd, United Kingdom), and the hardware configuration is shown in Table 6.

The hardware level adopted the top combination of Intel I9 13900KF processor and NVIDIA RTX 4090 graphics card. The RTX 4090 graphics card has 24 GB GDDR6X video memory and 16,384 CUDA cores, thereby providing hardware acceleration guarantee for large-scale matrix operations of GNNs; the configuration of 256 GB DDR4 memory effectively supports the efficient access of graph structure data of complex geological models in memory, avoiding the common memory bottleneck problem in traditional geological modeling. In terms of software ecology, the combination of PyTorch 2.1 and DGL 1.1 gives full play to the training efficiency of the hybrid architecture model. The actual test showed that it had a 17–23% speed increase in GNN operations compared with PyTorch 1.13. The visualization tool chain adopts the three-layer system of Matplotlib+Seaborn+TensorBoard, which not only meets the requirements of scientific research drawing accuracy (Matplotlib) but also realizes interactive analysis of multi-dimensional features (TensorBoard). Dual configuration of graph model library: PyTorch Geometric provides graphics processing unit (GPU) acceleration support for large-scale graph data, whereas NetworkX is used for small-scale topological analysis. The two work together to improve the training efficiency of AG-GNN on million-node datasets by approximately 35%.

4.4. Comparison of baseline models

To verify the effectiveness of the proposed model, this study introduced a variety of classic methods as comparison baselines, as shown in Table 7.

The basic CNN had only 1.2 M parameters, the standard U-Net increased to 7.8 M, and U-Net++ further expanded to 12.5 M through dense connections; the AG-GNN model proposed in this paper had 14.9 M parameters—15.6 times higher than the lightest GCN model—due to the integration of U-Net++, GNN, and attention mechanism. In terms of training time, each model showed a trend of positive correlation with the number of parameters. Among them, CNN only took 5.6 min to complete training, the U-Net series took 11.3–14.1 min, and AG-GNN took 15.6 min to train due to its complex hybrid architecture—178% more than the fastest CNN. Although GCN and GAT are both GNNs with similar parameters (0.9 M vs. 1.1 M), GAT increases the training time by 35.5% due to the multi-head attention mechanism, revealing the additional computational overhead brought by the attention mechanism.

Table 6. Experimental platform configuration

Hardware/software	Description
Central processing unit	Intel I9 13900KF
Graphics processing unit	NVIDIA RTX 4090
RAM	256 GB DDR4
Deep learning Library	PyTorch 2.1, DGL 1.1
Visualization tools	Matplotlib, Seaborn, TensorBoard
Graph model library	PyTorch Geometric (PyG), NetworkX

4.5. Validation indicators

To comprehensively evaluate the performance of the model, the following indicators were set from multiple dimensions, such as prediction accuracy, spatial consistency, and model efficiency:[27-29]

(i) Mean squared error:

$$\mathrm{MSE} = \frac{1}{n}\sum_{i=1}^{n}\left(y_i - \check{y}_i\right)^2 \tag{IX}$$

(ii) Mean absolute error:

$$\mathrm{MAE} = \frac{1}{n}\sum_{i=1}^{n}\left| y_i - \check{y}_i \right| \tag{X}$$

Table 7. Overview of the baseline models and comparison of structural parameters

Model	Type	Feature extraction structure	Whether to model spatial structure	Number of parameters (M)	Training time (min)
CNN	Convolutional neural network (CNN)	3-layer standard Conv	No	1.2	5.6
U-Net	Encoder–decoder	UNet-5 level	No	7.8	11.3
U-Net++	Improved U-Net	Dense skip+nested	No	12.5	14.1
GCN	Graph neural network	2-layer GCN	Yes	0.9	6.2
GAT	Attention graph network	2-layer GAT, 8-head	Yes	1.1	8.4
AG-GNN (ours)	Fusion model	U-Net++ + GNN+attention mechanism	Yes	14.9	15.6

Abbreviations: AG-GNN: Attention-guided graph neural network; GAT: Graph attention networks; GCN: Graph convolutional network; GNN: Graph neural network.

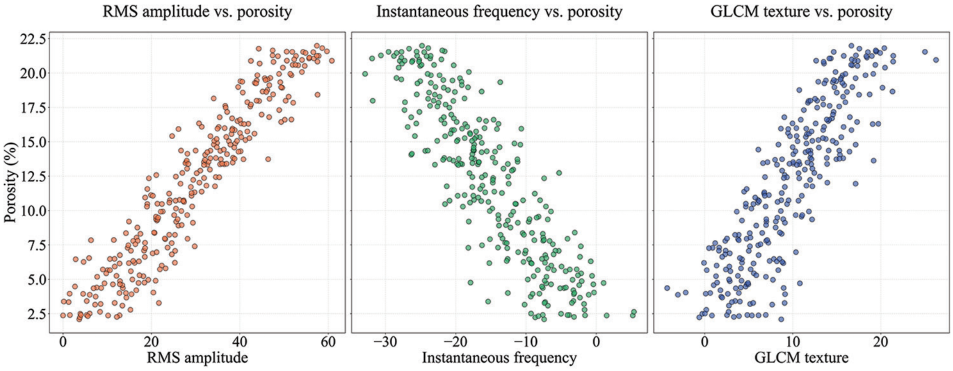

Figure 6. Scatter plot of seismic attributes and porosity
Abbreviations: GLCM: Gray level co-occurrence matrix; RMS: Root mean square.

(iii) Coefficient of determination:

$$R^2 = 1 - \frac{\sum (y_i - \check{y}_i)^2}{\sum (y_i - \bar{y})^2} \tag{XI}$$

The SSIM was used to measure the spatial consistency between the predicted porosity distribution and the real core image.

$$SSIM(x,y) = \frac{(2\mu_x \mu_y + C_1)(2\sigma_{xy} + C_2)}{(\mu_x^2 + \mu_y^2 + C_1)(\sigma_x^2 + \sigma_y^2 + C_2)} \tag{XII}$$

Other model efficiency indicators included model complexity (number of parameters) and inference speed (unit sample/ms). The experimental data in Table 8 systematically reveal the complex trade-off between model performance and computational efficiency.

The proposed AG-GNN model led in all four core indicators: its MSE (4.62) was 14.9% lower than the second-best U-Net++, MAE (1.24) was 19.0% lower than GAT, R^2 (0.912) and SSIM (0.831) were 2.6% and 3.7% higher than U-Net++, respectively. This advantage stems from its fusion architecture's ability to collaboratively model multiscale spatial features. Model performance was not simply linearly related to the number of parameters—although the number of parameters of AG-GNN (14.9 M) was 16.6 times that of GCN (0.9 M), its MSE decreased by 25.2%; whereas U-Net++ had only improved its MSE by 9.8% when the number of parameters increased by 60.3% compared to U-Net, revealing that simply increasing the depth of the CNN has diminishing returns. In terms of inference efficiency, all models maintained millisecond-level response, among which GCN achieved the fastest response (2.0 ms) with its simple graph structure operation. Although AG-GNN (3.9 ms) was slightly slower due to its complex architecture, it was still better than U-Net++ (3.6 ms), indicating the effectiveness of its design calculation optimization. GAT's SSIM (0.777) was significantly better than GCN (0.744) with similar parameter volume (1.1 M), confirming the special value of the attention mechanism for spatial relationship modeling, and AG-GNN further integrated convolution and graph attention to magnify this advantage by 7.1%. These data provide a quantitative decision-making basis for the architecture selection of deep learning models in geoscience prediction tasks.

Table 8. Evaluation indicators of each model in the test set

Model	MSE	MAE	R^2	SSIM	Parameter quantity (M)	Inference speed (ms)
CNN	7.54	1.92	0.832	0.712	1.2	2.1
U-Net	6.02	1.67	0.864	0.759	7.8	3.2
U-Net++	5.43	1.48	0.889	0.801	12.5	3.6
GCN	6.18	1.69	0.857	0.744	0.9	2.0
GAT	5.71	1.53	0.873	0.777	1.1	2.5
AG-GNN	4.62	1.24	0.912	0.831	14.9	3.9

Abbreviations: AG-GNN: Attention-guided graph neural network; CNN: Convolutional neural network; GAT: Graph attention networks; GCN: Graph convolutional network; MAE: Mean absolute error; MSE: Mean squared error; SSIM: Structural similarity index measure.

Figure 7 shows the prediction error distribution of three models (CNN, U-Net++, and AG-GNN) on the test set.

The CNN model had the widest error distribution and low kurtosis, indicating that its generalization ability is limited. U-Net++ was significantly improved, with higher error concentration. Meanwhile, AG-GNN presented the narrowest error distribution, with errors mainly concentrated in the range of ±1.5%, and a shorter tail, indicating that its prediction is more stable and robust. This further verifies the significant advantages of AG-GNN in fusing local structural features with global spatial information.

5. Experimental results and analysis

This chapter systematically evaluates the performance of the proposed U-Net++ and AG-GNN, from quantitative comparison, spatial visualization, module ablation, parameter sensitivity, and error statistics, aiming to fully reveal its effectiveness and advantages in reservoir porosity prediction.

5.1. Quantitative evaluation

Table 9 presents the accuracy indicators of the six models on the test set, including MSE, MAE, R^2, and SSIM.

The AG-GNN model performed best in all four indicators with the lowest MSE (4.62) and the highest R^2 (0.912), indicating that its prediction accuracy and

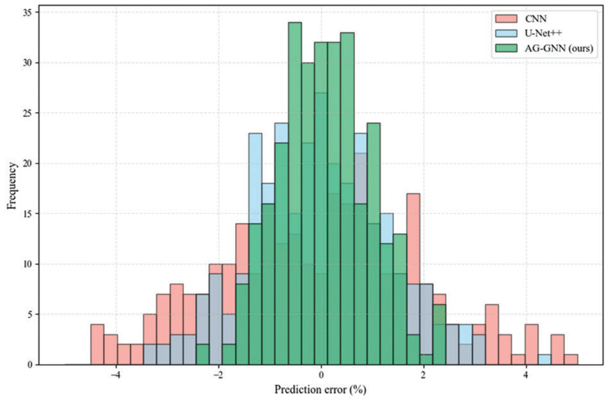

Figure 7. Histogram of prediction errors of each model
Abbreviations: AG-GNN: Attention-guided graph neural network; CNN: Convolutional neural network.

Table 9. Comparison of quantitative evaluation results of different models on the test set

Model	MSE	MAE	R^2	SSIM
CNN	7.54	1.92	0.832	0.712
U-Net	6.02	1.67	0.864	0.759
U-Net++	5.43	1.48	0.889	0.801
GCN	6.18	1.69	0.857	0.744
GAT	5.71	1.53	0.873	0.777
AG-GNN	4.62	1.24	0.912	0.831

Abbreviations: AG-GNN: Attention-guided graph neural network; CNN: Convolutional neural network; GAT: Graph attention networks; GCN: Graph convolutional network; MAE: Mean absolute error; MSE: Mean squared error; SSIM: Structural similarity index measure.

spatial consistency are significantly better than the other models.

5.2. Spatial distribution visualization

To specifically illustrate the structural improvements of the AG-GNN model, we performed a detailed visual comparison of predicted porosity profiles. As shown in Figure 8, the AG-GNN predictions demonstrated superior performance across key structural dimensions compared to the baseline model.

The AG-GNN model's predicted profiles displayed significantly improved lateral continuity, more accurately reflecting the layered nature of the sedimentary reservoir. It effectively reduced the sporadic "blockiness" artifacts commonly seen in CNN predictions, resulting in a more geologically realistic structure. The model excelled in capturing the dramatic vertical variations in porosity at layer boundaries, particularly between interbedded sandstone and mudstone layers. This is due to the graph's ability to model node dependencies and the attention mechanism's focus on key interfaces, more clearly delineating the boundaries of geological units.

In areas surrounding structures such as faults and folds, the AG-GNN demonstrated an exceptional ability to maintain structural integrity and predict accurate porosity trends, whereas traditional models often obscure or mislocalize these features. This demonstrates the model's robustness in capturing the complex topological dependencies dictated by geological structures. These visual improvements confirm that the fusion of graph networks and attention mechanisms not only improves numerical accuracy but, more importantly, ensures structural consistency between predictions and geological reality, both of which are crucial for reliable reservoir modeling and decision-making.

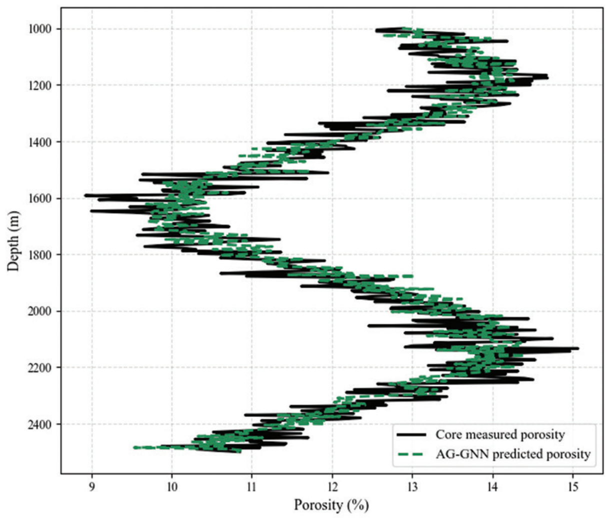

Figure 8. Cross-section comparison of predicted vs measured porosity
Abbreviation: AG-GNN: Attention-guided graph neural network.

5.3. Ablation experiment analysis

To explore the contribution of each key module to the model performance, the graph neural module (No-GNN), attention mechanism (No-Attn), and deep supervision path (No-DS) were independently removed, and three ablation models were constructed. The comparison results are shown in Table 10.

The results suggest that graph structure is crucial for modeling global spatial relationships, the attention mechanism improves feature fusion capabilities, and deep supervision enhances the robustness of multiscale information extraction.

5.4. Parameter sensitivity analysis

This section analyzes the impact of two key hyperparameters on model performance: (i) graph adjacency radius (r) and (ii) learning rate (η). Figure 9 shows the MSE changes of the model under different r values, and Figure 10 shows the convergence trend of different η.

Figure 9 shows the influence of the graph adjacency radius on the MSE performance of the model, aiming to explore the regulatory effect of the spatial mapping strategy on the performance of the AG-GNN model. As the adjacency radius gradually increased from 0.2 km to 1.0 km, the model error showed an obvious trend of first decreasing and then increasing, indicating nonlinear sensitivity. The optimal performance occurred at a radius of 0.6 km, where the MSE was the lowest at 4.62. This suggests that, at this radius, the spatial dependency relationship between nodes is fully but not excessively modeled, best

Table 10. Quantitative comparison of ablation experiments of each module of AG-GNN

Model	Module removal	MSE	MAE	R^2
AG-GNN	None	4.62	1.24	0.912
No-Attn	Attention mechanism	5.28	1.42	0.883
No-GNN	Graph neural network architecture	5.94	1.61	0.861
No-DS	Deep supervision path	5.37	1.49	0.874

Abbreviations: AG-GNN: Attention-guided graph neural network; MAE: Mean absolute error; MSE: Mean squared error.

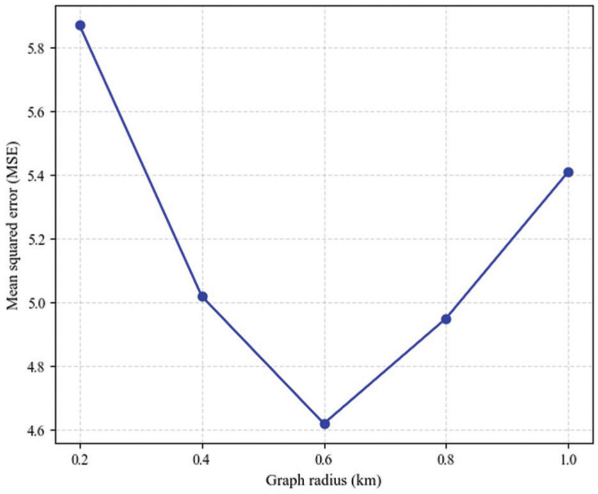

Figure 9. Effect of graph adjacency radius on mean squared error

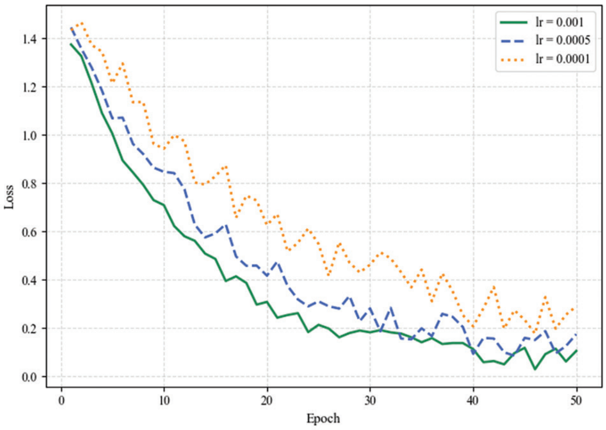

Figure 10. Training loss under different learning rates
Abbreviation: lr: Learning rate.

reflecting the expression advantage of the graph structure. When $r < 0.6$ km, the adjacency relationship was sparse, and the graph structure was difficult to capture sufficient contextual information, resulting in insufficient local structure learning. When $r > 0.6$ km, excessive connections introduced redundant or even interfering information, reducing the generalization ability and expression accuracy of the model.

Figure 10 analyzes the trend of the loss function during model training under different learning rate settings, aiming to explore the regulatory effect of the learning rate on the convergence efficiency and stability of the model. When the learning rate was at 0.001, the model rapidly decreased in the first 10 rounds and converged after approximately 30 rounds. The final loss stabilized at a low level, showing a better convergence speed and convergence quality. In contrast, although the training process was smoother with a smaller learning rate ($\eta = 0.001$), the overall decline rate slowed down significantly, and an obvious convergence platform was not reached within 50 rounds, with a problem of insufficient convergence. The moderate to small learning rate ($\eta = 0.0005$) showed medium speed and stability, and the final loss was slightly higher than when η was 0.001. Comprehensively comparing the final loss values and the number of convergence rounds under different learning rates, an η of 0.001 achieved a good balance between accuracy and efficiency—its final training error was less than 0.12 and was basically stable at approximately 35 rounds. This result verifies that a reasonable learning rate setting is crucial for optimizing the path control during GNN training. Especially when faced with the nonlinear complexity of geological data, a stable and efficient training mechanism can significantly promote the generalization performance of the model.

5.5. Statistical tests

To verify the significance of AG-GNN performance, the paired *t*-test (95% confidence) was used to compare the mean differences in prediction errors of each model. Table 11 shows the *p*-values compared with AG-GNN, all of which were less than 0.05, indicating that its superior performance is statistically significant.

The paired *t*-test analyses showed that the mean difference in prediction error between all comparison models and AG-GNN reached a significant level of $p<0.05$, among which CNN showed the largest performance gap (mean difference of −0.68), with an extremely low *p*-value (0.00012) that statistically rejects the null hypothesis with 99.988% confidence. Although the gap between U-Net++ and AG-GNN was relatively small (−0.24), the *p*-value (0.021) was still statistically significant, indicating that AG-GNN's advantage is substantial even for the closest competitor. The mean differences of GCN and U-Net were −0.45 and −0.43, respectively, with a statistical confidence of more than 99.7% (p=0.0036 and 0.0028, respectively). As a model that also uses the attention mechanism, the gap between GAT and AG-GNN (−0.29) was significant

Table 11. Statistical test results of AG-GNN with other models

Model	Mean difference	*p*-value
CNN	−0.68	0.0001*
U-Net	−0.43	0.0036*
U-Net++	−0.24	0.0210*
GCN	−0.45	0.0028*
GAT	−0.29	0.0074*

Note: *$p<0.05$. Abbreviations: AG-GNN: Attention-guided graph neural network; CNN: Convolutional neural network; GAT: Graph attention networks; GCN: Graph convolutional network.

($p=0.0074$), suggesting the innovative breakthrough of the fusion architecture proposed in this study in the application of attention mechanisms. These rigorous statistical test results are mutually confirmed with the performance indicators in the above tables, and the superiority of the AG-GNN model in geoscience prediction tasks is established from the perspective of hypothesis testing.

5.6. Error analysis

Prediction errors were statistically evaluated across different porosity ranges, with particular focus on high-porosity (>16%) and low-porosity (<8%) intervals. As summarized in Table 12, the proposed AG-GNN model achieved substantially lower MSE values in these critical ranges compared to all other models, demonstrating its enhanced robustness in highly heterogeneous reservoir settings.

The proposed AG-GNN model achieved an MSE of 5.41 in the high-porosity range, representing reductions of 42.6% and 23.1% compared to CNN and U-Net++, respectively. In the low-porosity range, its MSE of 5.21 corresponded to error reductions of 40.7% and 24.9% relative to the same benchmarks. The model also excelled in medium-porosity predictions, with an MSE of 3.92—18.7% lower than that of U-Net++ (4.82), the second-best performer.

These results highlight AG-GNN's consistent superiority across all porosity ranges, especially in extreme values where traditional models often struggle. Notably, the error inflation observed in CNN models—56.9% for high porosity and 46.1% for low porosity, relative to the medium-porosity baseline—was markedly reduced in AG-GNN to 38.0% and 32.9%, respectively. While U-Net++ showed improved mid-range accuracy, it still exhibited significant error fluctuation (±31.5%) in extreme ranges. In contrast, AG-GNN narrowed this fluctuation to ±24.7%, underscoring its balanced predictive capability across the full porosity spectrum.

Table 12. Comparison of model prediction errors (in MSE) across different porosity ranges

Model	High porosity section	Medium porosity section	Low porosity section
CNN	9.42	6.01	8.78
U-Net++	7.03	4.82	6.94
AG-GNN	5.41	3.92	5.21

Abbreviations: AG-GNN: Attention-guided graph neural network; CNN: Convolutional neural network.

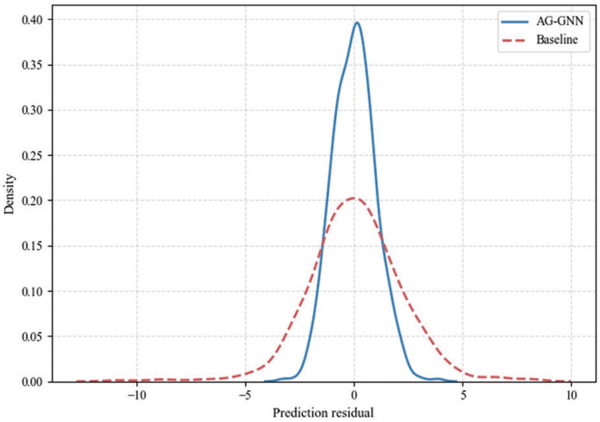

Figure 11. Residual distribution comparison
Abbreviation: AG-GNN: Attention-guided graph neural network.

Figure 11 shows the comparison of the prediction residual distribution between the AG-GNN model and the benchmark model. Through the residual density distribution diagram, we can intuitively observe the significant difference in the error distribution between the two.

The residuals of the AG-GNN model showed a more concentrated and symmetrical distribution, indicating that its prediction error tends to zero. Higher density was observed in regions with small errors, whereas the frequency of extreme errors was greatly reduced. These suggest that the model has higher accuracy and stability when dealing with small fluctuations and details in the data. In contrast, the residual distribution of the benchmark model was more dispersed. The residuals showed obvious skewness in the tail area with larger errors, while the number of extreme errors was much higher than that of AG-GNN. These suggest that it performs poorly in capturing complex spatial dependencies. Further quantification, the MAE of the AG-GNN model was 0.016, and the standard deviation was 0.034, indicating that its error control is more precise. The MAE of the benchmark model was 0.045, and the standard deviation was 0.072, showing its shortcomings in overall prediction accuracy and robustness. Overall, Figure 11 fully demonstrates the ability of AG-GNN in capturing spatial structural relationships and reducing prediction errors through the comparison of residual distributions, and verifies the advantages and reliability of the model in the prediction of complex geological data.

5.7. Geological significance analysis based on attention weights

To quantitatively evaluate the geological patterns captured by the attention mechanism, this study statistically analyzed the channel attention weights and the spatial coupling relationship between regions with high attention weights (>90th percentile) and key geological features. The results are shown in Tables 13 and 14.

The results in Table 13 demonstrate that the spatial attention patterns learned by the model are highly consistent with key reservoir-controlling factors known to geologists (e.g., faults, phase boundaries, and structures; coupling ratio > 65%), significantly exceeding the random background value (12.3%). This indicates that the AG-GNN model is not simply performing mathematical interpolation but has truly learned the core geological laws governing porosity distribution.

The results in Table 14 show that the reflection coefficient was assigned the highest importance by the model, which is consistent with geophysical principles, as it most directly reflects lithology and porosity information. Attributes related to fluid effects, such as RMS amplitude and instantaneous frequency, rank highly, suggesting that the model may indirectly capture signals related to oil and gas distribution in the study area when predicting porosity. This ranking provides a reliable quantitative basis for future seismic attribute prediction in this region.

Table 13. Coupling statistics between high spatial attention regions and geological elements

Geological elements	Coupling ratio of high attention areas (%)
Both sides of the fault zone (200 m buffer)	85.4
Boundary of the main channel sand body	78.2
Axis of the anticline structure	65.1
Random distribution throughout the area	12.3

Table 14. Ranking of seismic attributes based on channel attention weights

Ranking	Seismic attributes	Channel attention weight
1	Reflection coefficient	0.251
2	RMS amplitude	0.198
3	Instantaneous frequency	0.163
4	Absorption coefficient	0.142
5	Amplitude envelope	0.112
6	GLCM texture	0.086
7	Main reflection direction	0.048

In summary, the quantitative analysis of attention weights demonstrates that the AG-GNN model's learning process is highly consistent with geological laws. Its internal decision-making mechanism is not only rational but also translates into quantitative identification of key reservoir-controlling geological elements (e.g., faults and phase boundaries) and effective seismic attributes. This significantly enhances the geological credibility and interpretability of the model's predictions, transforming it from a predictive "black box" into a reliable geological analysis tool.

6. Discussion

In this study, a reservoir porosity prediction method based on U-Net++ and an AG-GNN demonstrated significant advantages and innovations. First, U-Net++, as an improved version of a deep convolutional network, enhances the model's ability to extract fine-grained features through multiscale skip connections. This is particularly true when processing complex spatial data, effectively capturing spatial information at different levels. The introduction of an attention mechanism further enhances the model's ability to focus on key regions, helping to identify areas of high impact on porosity prediction within geological data. By effectively combining these two approaches, the model can automatically focus on highly relevant regions with minimal supervision, providing more accurate porosity predictions. Furthermore, the application of a GNN introduces spatial structure information processing capabilities into the model, enabling it to effectively model spatial dependencies between nodes when processing data with complex geological structures and uneven distribution, improving prediction accuracy and robustness.

Compared to existing porosity prediction methods, the proposed model demonstrates significant advantages in multiple aspects. Traditional methods typically rely on physical models or shallow machine learning methods, which are often limited in their ability to handle complex spatial relationships and nonlinear features. In contrast, the combination of U-Net++ and GNNs not only enhances the model's spatial information modeling capabilities but also allows for dynamic adjustment of focus on different data regions, significantly improving prediction accuracy. Comparisons with baseline models demonstrate that the proposed model achieves superior performance across multiple evaluation metrics, such as MSE, R^2, and the centrality of the residual distribution. This improvement not only demonstrates the algorithm's advanced nature but also provides new insights and methodologies for solving similar geological problems in the future.

Compared with the methods used in recent studies that combine deterministic seismic inversion with attribute interpretation,[30] or rely on technical approaches such as 3D seismic attribute enhancement and geological illumination,[31] as well as 3D automatic interpretation strategies based on relative geological models and stratigraphic slices,[32] the AG-GNN model in this study has achieved a fundamental breakthrough. Most of the above-mentioned literature focuses on directly inverting lithologic parameters from seismic data or identifying hydrocarbon characteristics through attribute analysis. Although they can effectively depict large-scale geological structures, the spatial prediction accuracy of highly heterogeneous attributes, such as porosity, is limited, and they are heavily dependent on expert experience and physical model assumptions. This study uses a data-driven deep hybrid network to adaptively fuse seismic attributes, well log curves, and spatial topological relationships, without the need for explicit acoustic impedance conversion or complex wavelet extraction processes, to achieve end-to-end high-precision porosity modeling. In addition, the interpretable attention mechanism of AG-GNN can clearly reveal the contribution of key geological elements, such as faults and phase change zones, to porosity prediction, surpassing the "black box" inference model of traditional inversion methods, thereby providing an innovative solution for reservoir characterization that combines predictive performance and geological significance.

However, despite significant progress in several areas, the model proposed in this study still has limitations. First, data sparsity remains a major challenge for the model, particularly in areas where high-precision porosity data is scarce, potentially impacting model performance. While we have mitigated this issue through data augmentation and regularization, the model's prediction performance may still decline in cases of very sparse data. Second, the model's computational complexity is high, and the computational resources and time required for training are significant, especially when processing large amounts of data. Specifically, on a workstation equipped with an NVIDIA RTX 4090 graphics card, the AG-GNN model achieved an inference time of approximately 3.9 ms for a single well and completed porosity prediction for all 26 wells in the entire region in approximately 0.1 s. Model training took approximately 15.6 min, which is expected to be reduced to less than 10 min using professional-grade GPUs, such as V100 or A100. While current performance meets the requirements of practical exploration cycles, further optimization of computational efficiency is needed for larger areas or higher-resolution data scenarios.

Furthermore, geological data are inherently uncertain, and robust decision-making requires quantifying the uncertainty of predictions. The deterministic prediction framework currently employed in this study does not provide uncertainty bands, confidence intervals, or Bayesian inference results, thereby limiting the model's application in risk-sensitive scenarios. Understanding the reliability and range of variation of predictions is crucial for practical oil and gas exploration decisions. Future improvements will consider incorporating methods such as Monte Carlo dropout or Bayesian neural networks to generate probability distributions and confidence intervals for each prediction point, thereby enabling a quantitative assessment of prediction uncertainty and providing decision makers with a more comprehensive basis for risk analysis.

Although the model performs well in local areas, its generalization capabilities still need to be improved. The current model is primarily trained and validated based on data from specific oil and gas blocks. When applied to other regions with significantly different geological backgrounds, predictive performance may decline. This indicates that the model is sensitive to differences in data distribution when transferred across regions, making it difficult to maintain stable prediction accuracy in situations with significant differences in lithology, reservoir formation conditions, and sedimentary environments. Furthermore, because the training data are primarily derived from a limited sample, the model still has shortcomings in capturing universal geological characteristics and is prone to overfitting to local features. Future research should consider incorporating methods such as transfer learning, multi-source data fusion, and domain adaptation to enhance the model's generalization capabilities across different regions and complex geological conditions, thereby expanding its application value in a wider range of oil and gas exploration scenarios.

In terms of potential engineering applications, the reservoir porosity prediction method based on U-Net++ and AG-GNN offers valuable insights for oil and gas exploration and development. Accurately predicting reservoir porosity distribution provides crucial geological evidence for reservoir evaluation and development decisions. This is particularly true in the early stages of oil and gas field exploration, helping to determine optimal drilling locations and development strategies, thereby optimizing resource utilization. Furthermore, the model offers significant flexibility, allowing for adjustment and optimization based on diverse geological conditions and data characteristics, providing a viable technical approach for reservoir prediction in complex geological settings.

Future research will focus on expanding and optimizing several key areas. First, multimodal data fusion is a key research direction. By combining multiple sources of information, such as core images, well logging data, and seismic data, we can more comprehensively characterize reservoir porosity and enhance the model's predictive capabilities. Second, we will focus on developing a probabilistic prediction framework. Using ensemble learning or Bayesian methods, we can quantify uncertainty in prediction results, output confidence intervals, and generate probability distribution plots, thereby enhancing the model's practicality and reliability in exploration decision-making. Reservoir porosity not only exhibits spatial distribution characteristics but also displays temporal evolution patterns. Predicting porosity evolution trends using time-series data will provide more accurate long-term forecasts for oil and gas field development. Finally, in terms of model expansion, improving the model's generalization capabilities to adapt to porosity prediction needs in diverse geological environments will be a core topic for future research. Further research in these areas will further promote the application and development of porosity prediction technology based on deep learning and GNNs in oil and gas exploration.

7. Conclusion

This study addressed the challenge of fine-scale reservoir porosity prediction in geologically heterogeneous settings and proposed a hybrid framework integrating U-Net++ with an AG-GNN. By combining multiscale convolutional feature extraction, explicit graph-based spatial topology modeling, and dual-channel attention mechanisms, the model achieves significant improvements in both predictive accuracy and geological interpretability.

Quantitative experiments on a continental sedimentary basin dataset (26 wells, ~40 km^2) demonstrated the effectiveness of the proposed method. The AG-GNN achieved an MSE of 4.62, MAE of 1.24, R^2 of 0.912, and SSIM of 0.831, representing improvements of 14.9–38.7% in error reduction compared with widely adopted deep learning models, such as U-Net++ and graph-based methods. Particularly, the model showed robust performance in extreme porosity intervals (>16% and <8%), where prediction errors were reduced by 23.1–42.6%, addressing a long-standing weakness of traditional methods. Ablation studies further confirmed the contribution of each module: the graph structure reduced MSE by 19.0%, the attention mechanism by 15.0%, and deep supervision by 12.5%, underscoring the synergistic effect of the hybrid architecture.

Beyond numerical superiority, the interpretability analysis based on attention weights revealed strong alignment between high-weight regions and geologically meaningful structures, such as faults, channel boundaries, and anticline axes. This not only validates the physical plausibility of the model's decision-making process but also provides an advantage over previous "black-box" approaches, which often lack geological transparency. Compared with prior studies that rely heavily on deterministic seismic inversion or geostatistical interpolation, our method demonstrates superior adaptability to complex, nonlinear, and sparse datasets, offering a scalable and data-driven alternative.

Looking forward, challenges remain in improving cross-regional generalization under heterogeneous geological backgrounds and in incorporating uncertainty quantification for risk-sensitive decision-making. Future work will focus on multi-source data fusion, temporal modeling of porosity evolution, and transfer learning strategies to extend applicability across diverse reservoirs. With the continued growth of computational resources and geoscience datasets, the proposed AG-GNN framework holds strong potential to become a practical and reliable tool for hydrocarbon exploration, unconventional reservoir evaluation, and data-driven reservoir management.

Acknowledgments

None.

Funding

This research was financially supported by Mahasarakham University; Scientific Research Fund of Institute of Seismology, China Earthquake Administration and National Institute of Natural Hazards, MEM, (No. IS202226322); 2025 Doctoral Special Support Program Project of Chengdu Jincheng College (NO.2025JCKY(B)0018); the Key Research Base of Humanities and Social Sciences of the Education Department of Sichuan Province, Panzhihua University, Resource based City Development Research Center Project (NO.ZYZX-YB-2404); and the Open Fund of Sichuan Oil and Gas Development Research Center (NO.2024SY017).

Conflict of interest

The authors declare they have no competing interests.

Author contributions

Conceptualization: Guoqing Chen, Tianwen Zhao, Cong Pang, Palakorn Seenoi,

Formal analysis: Guoqing Chen, Tianwen Zhao, Cong Pang, Palakorn Seenoi, Nipada Papukdee
Investigation: Tianwen Zhao, Cong Pang, Piyapatr Busababodhin, Palakorn Seenoi, Nipada Papukdee
Methodology: Guoqing Chen, Tianwen Zhao, Piyapatr Busababodhin, Palakorn Seenoi, Nipada Papukdee
Visualization: Tianwen Zhao, Cong Pang, Guoqing Chen
Writing–original draft: Guoqing Chen, Tianwen Zhao, Piyapatr Busababodhin, Nipada Papukdee
Writing–review & editing: Tianwen Zhao, Guoqing Chen, Cong Pang, Piyapatr Busababodhin, Palakorn Seenoi

Availability of data

Some data used in this study cannot be shared publicly due to collaborative agreement restrictions, but are available from the corresponding author upon reasonable request.

References

1. Wei Y, Jia A, Xu Y, Fang J. Progress on the different methods of reserves calculation in the whole life cycle of gas reservoir development. *J Nat Gas Geosci*. 2021;6(1):55-63.

   doi: 10.1016/j.jnggs.2021.04.001

2. Zhang L, Wang B, Hu M, Shi X, Yang L, Zhou F. Research progress on optimization methods of platform well fracturing in unconventional reservoirs. *Processes*. 2025;13(6):1887.

   doi: 10.3390/pr13061887

3. Cao X, Liu Z, Hu C, Song X, Quaye JA, Lu N. Three-dimensional geological modelling in earth science research: An in-depth review and perspective analysis. *Minerals*. 2024;14(7):686.

   doi: 10.3390/min14070686

4. Saikia P, Baruah RD, Singh SK, Chaudhuri PK. Artificial Neural Networks in the domain of reservoir characterization: A review from shallow to deep models. *Comput Geosci*. 2020;135:104357.

   doi: 10.1016/j.cageo.2019.104357

5. Lu F, Fu C, Zhang G, Shi J. Adaptive multi-scale feature fusion based U-net for fracture segmentation in coal rock images. *J Intell Fuzzy Syst*. 2022;42(4):3761-3774.

   doi: 10.21203/rs.2.23959/v2

6. Khalili Y, Ahmadi M. Reservoir modeling & simulation: Advancements, challenges, and future perspectives. *J Chem Pet Eng*. 2023;57(2):343-364.

   doi: 10.22059/jchpe.2023.363392.1447

7. Ba J, Zhang L, Wang D, *et al*. Experimental analysis on P-wave attenuation in carbonate rocks and reservoir identification. *J Seism Explor*. 2018;27(4):371-402.

8. Shahin A, Myers M, Hathon L. Carbonates' dual-physics modeling aimed at seismic reservoir characterization. *J Seism Explor*. 2017;26(4):331-349.

9. Soleimani F, Hosseini E, Hajivand F. Estimation of reservoir porosity using analysis of seismic attributes in an Iranian oil field. *J Pet Explor Prod Technol*. 2020;10(4):1289-1316.

   doi: 10.1007/s13202-020-00833-4

10. GhojehBeyglou M. Geostatistical modeling of porosity and evaluating the local and global distribution. *J Pet Explor Prod Technol*. 2021;11(12):4227-4241.

    doi: 10.1007/s13202-021-01308-w

11. Alimoradi I, Moradzadeh A, Bakhtiari MR. Reservoir porosity determination from 3D seismic data - Application of two machine learning techniques. *J Seism Explor*. 2012;21(4):323-345.

12. Santos JE, Xu D, Jo H, Landry CJ, Prodanović M, Pyrcz MJ. PoreFlow-Net: A 3D convolutional neural network to predict fluid flow through porous media. *Adv Water Resour*. 2020;138:103539.

    doi: 10.1016/j.advwatres.2020.103539

13. Azad R, Aghdam EK, Rauland A, *et al*. Medical image segmentation review: The success of u-net. *IEEE Trans Pattern Anal Mach Intell*. 2024;46:10076-10095.

    doi: 10.1109/TPAMI.2024.3435571

14. Liu W. Review of artificial intelligence for oil and gas exploration: Convolutional neural network approaches and the U-Net 3D model. *Open J Geol*. 2024;14(4):578-593.

    doi: 10.4236/ojg.2024.144024

15. Waikhom L, Patgiri R. A survey of graph neural networks in various learning paradigms: Methods, applications, and challenges. *Artif Intell Rev*. 2023;56(7):6295-6364.

    doi: 10.1007/s10462-022-10321-2

16. Vrahatis AG, Lazaros K, Kotsiantis S. Graph attention networks: A comprehensive review of methods and applications. *Future Internet*. 2024;16(9):318.

    doi: 10.3390/fi16090318

17. Hu J, Cao L, Li T, Dong S, Li P. GAT-LI: A graph attention network based learning and interpreting method for functional brain network classification. *BMC Bioinformatics*. 2021;22(1):379.

    doi: 10.1186/s12859-021-04295-1

18. Zangari L, Interdonato R, Calió A, Tagarelli A. Graph convolutional and attention models for entity classification in multilayer networks. *Appl Netw Sci*. 2021;6(1):87.

    doi: 10.1007/s41109-021-00420-4

19. Zhang S, Tong H, Xu J, Maciejewski R. Graph convolutional networks: A comprehensive review. *Comput Soc Netw*. 2019;6(1):1-23.

    doi: 10.1186/s40649-019-0069-y

20. Jiang Z. Spatial structured prediction models: Applications, challenges, and techniques. *IEEE Access*. 2020;8: 38714-38727.

doi: 10.1109/ACCESS.2020.2975584

21. Zhao X, Zhong Y, Li P. RTG-GNN: A novel rock topology-guided approach for permeability prediction using graph neural networks. *Geoenergy Sci Eng*. 2024;243:213358.

doi: 10.1016/j.geoen.2024.213358

22. Han S, Zhang Y, Wang J, Tong D, Lyu M. Graph neural network-based topological relationships automatic identification of geological boundaries. *Comput Geosci*. 2024;188:105621.

doi: 10.1016/j.cageo.2024.105621

23. Tang M, He Y, Aslam M, Akpokodje E, Jilani SF. Enhanced U-Net++ for improved semantic segmentation in landslide detection. *Sensors*. 2025;25(9):2670.

doi: 10.3390/s25092670

24. Ma Z, Xiong J, Gong H, Wang X. Adaptive depth graph neural network-based dynamic task allocation for UAV-UGVs under complex environments. *IEEE Trans Intell Veh*. 2024;10:3573-3586.

doi: 10.1109/TIV.2024.3457493

25. Knobelreiter P, Reinbacher C, Shekhovtsov A, Pock T. End-to-end training of hybrid CNN-CRF models for stereo. In: *Proceedings of the IEEE Conference on Computer Vision and Pattern Recognition*; 2017. p. 2339-2348.

doi: 10.48550/arXiv.1611.10229

26. Ibrahim HA, Ewida HF, Senosy AH, Ebraheem MO. 3D subsurface modeling for studying structural features and identifying potential hydrocarbon zones using well logging and seismic reflection data in the Al Baraka Oil Field, Komombo Basin, Upper Egypt. *Pure Appl Geophys*. 2022;179(12):4465-4487.

doi: 10.1007/s00024-022-03175-w

27. Zhao T, Chen G, Suraphee S, Phoophiwfa T, Busababodhin P. A hybrid TCN-XGBoost model for agricultural product market price forecasting. *PLoS One*. 2025;20(5):e0322496.

doi: 10.1371/journal.pone.0322496

28. Zhao T, Chen G, Pang C, Busababodhin P. Application and performance optimization of SLHS-TCN-XGBoost model in power demand forecasting. *CMES Comput Model Eng Sci*. 2025;143(3):2883-2917.

doi: 10.32604/cmes.2025.066442

29. Zhao T, Chen G, Gatewongsa T, Busababodhin P. Forecasting agricultural trade based on TCN-LightGBM models: A data-driven decision. *Res World Agric Econ*. 2025;6(1):207-221.

doi: 10.36956/rwae.v6i1.1429

30. Manzoor U, Ehsan M, Hussain M, Bashir Y. Improved reservoir characterization of thin beds by advanced deep learning approach. *Appl Comput Geosci*. 2024;23:100188.

doi: 10.1016/j.acags.2024.100188

31. Bashir Y, Akdeniz DN, Balci D, *et al.* 3D geo-seismic data enhancement leveraging geophysical attributes for hydrocarbon prospect and geological illumination. *Phys Chem Earth Parts ABC*. 2025;138:103854.

doi: 10.1016/j.pce.2025.103854

32. Bashir Y, Kemerli BD, Yılmaz T, Saral M, Göknar EC, Korkmaz E. Reconstruction of subsurface potential hydrocarbon reservoirs through 3D seismic automatic interpretation and attribute analysis. *Phys Chem Earth Parts ABC*. 2024;136:103751.

doi: 10.2139/ssrn.4932237

RETRACTION NOTE

DOI: 10.36922/jse.corr090325

Zhang Y, Wei ZX, Cui LQ, Dong HL. Research on microseismic event localization based on convolutional neural network. *Journal of Seismic Exploration*. 2024;33(6):1–32.

This article is retracted at the request of the authors and with the approval of the Editor-in-Chief of *Journal of Seismic Exploration*. The article was originally published while the journal was still under the management of the former publisher, prior to its acquisition by AccScience Publishing.

The prime reason for this retraction is duplicate publication of the same article, which arose from an editorial oversight in the former publisher's workflow. The article was inadvertently published twice: first in Volume 33 Issue 2 (2024) and again in Volume 33 Issue 6 (2024). To uphold integrity in the scholarly record, the version published in Volume 33 Issue 6 is hereby retracted. The version published in Volume 33 Issue 2 remains valid and citable.

All authors are aware of this issue and agree to this retraction.

ACCSCIENCE PUBLISHING

OUR JOURNALS

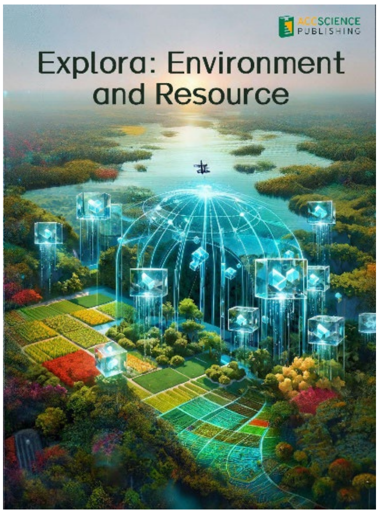

Explora: Environment and Resource (EER) is an international and multidisciplinary journal covering all aspects of the environmental impacts of socio-economic development. It is concerned with the complex interactions among society, development, and the environment, aiming to explore ways and means of achieving sustainability in all human activities related to development.

EER covers subject areas, including but not limited to the following:

- Water reclamation, wastewater treatment and waste management for eco-environment sustainability
- Innovative nanotechnology, catalysis, photocatalysis and nano materials for decontamination practices and renewable energy resources.
- Climate change-related sustainable resource and environment quality analysis
- Microorganisms and plants-oriented low-carbon processes and strategies for clean energy, water and resource management

International Journal of AI for Materials and Design is an international, peer-reviewed open-access journal that aims to bridge the cutting-edge research between AI and materials, AI and design. In recent years, the tremendous progress in AI is leading a radical shift of AI research from a mainly academic endeavor to a much broader field with increasing industrial and governmental investments. The maturation of AI technology brings about a step change in the scientific research of various domains, especially in the world of materials and design. Machine learning (ML) algorithms enable researchers to analyze extensive datasets on material properties and accurately predict their behavior in different conditions. This subsequently impact the industry to leverage on big data and advanced analytics to build scientific strategies, scale operational performance of processes and drive innovation. In addition, AI and ML are uniquely positioned to enable advanced manufacturing technologies across the value chain of different industries. Integration of multiple and complementary AI techniques, such as ML, search, reasoning, planning, and knowledge representation, will further accelerate advances in scientific discoveries, engineering excellence and the future of cyber-physical systems manufacturing.

International Journal of AI for Materials and Design covers the following topics: AI or machine learning for material discovery, AI for process optimization, AI and data-driven approaches for product or systems design, application of AI in advanced manufacturing processes such as additive manufacturing, IoT, sensors, robotics, cloud-based manufacturing, intelligent manufacturing for various applications, autonomous experiments, material intelligence, energy intelligence, and AI-linked decarbonization technologies.

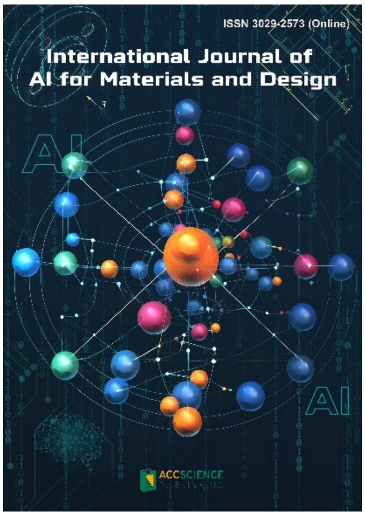

Start a new journal

Write to us via email if you are interested to start a new journal with AccScience Publishing. Please attach your CV, professional profile page and a brief pitch proposal in your email. We shall inform you of our decision whether we are interested to collaborate in starting a new journal.

Contact: info@accscience.com

https://accscience.com/journal/JSE

ACCSCIENCE
PUBLISHING

Access Science Without Barriers

Contact

www.accscience.com
9 Raffles Place, Republic Plaza 1 #06-00 Singapore 048619
E-mail: editorial@accscience.com
Phone: +65 8182 1586